University of Calabria - Department of Physics

Science and Technology of Mesophases and Molecular Materials
STM3 - XXI Cycle - FIS/07

Nanostructured Soft Matter: Mirror-less Laser

Mario Ariosto Matranga

Supervisor:
Prof. Riccardo Barberi

Ph.D. Student:
Mario Ariosto Matranga

Coordinator:
Prof. Carlo Versace

2007-2008

Commission:

Prof. Antonio D'Alessandro
Dipartimento di Ingegneria Elettronica, Università "La Sapienza" di Roma

Prof. Oriano Francescangeli
Dipartimento di Fisica e Ingegneria dei Materiali e del Territorio, Università Politecnica delle Marche

Prof. Gerardo Palazzo
Dipartimento di Chimica, Università di Bari

Prof. Antonio Raudino
Dipartimento di Chimica, Università di Catania

Prof. Alexander Mashin Lobachevsky
State University of Nizhni Novgorod (UNN)

Acknowledgments

There are a lot of people that played an important role during these years in my life and my scientific growth, these pages want to be a tribute to them. I have spent many hours in the lab working side by side with people that more than colleagues I like to consider them friends, all of them gave me a real help in carrying out this work.

It is fair at this point to thank my supervisor Prof. Riccardo Barberi for giving me the opportunity to attend this doctoral course and to e part of his staff.

In these days in the preface of an old thesis I found a sentence that sound like " this thesis would not be in this form if it was not for..." Well I have to really say now, looking at my work, that it would never be in this form without the help of Maria De Santo that follows all my work step by step. If the amount of mistakes present in this work is only a few of what it was initially it is mainly for her patience.

It was a real pleasure working with Alfredo Pane that taught me how to move my first steps in the clean room and with his experience solved a lot of my technical problems. I'm very thankful to Gia Petriashvili for sharing with me all his knowledge and for being a good fellow researcher.

The body of this thesis is based on the results of a few collaborations, Prof. Luis Oriol and Prof. Milagros Piñol of the University of Zaragoza, among the kindest persons I've ever met in my life, that provide me a lot of materials and their knowledge during these years. Prof. Guram Chilaya and Andro Chanishvili with whom some of the works of this thesis were carried out.

Obviously, all the other people of the licryl group are also in my mind from Prof. Gabriella Cipparrone and Prof. Lev Blinov for the long and helpful discussions, to Alfredo Mazzulla and Federica Ciuchi for the great collaboration and all the other people the use to live in the laboratories of the licryl, for all the hours we spent together (Massimo, Gianni, Bruno, Giuseppe, Habib, Ridha) and at the end all the new entries in the lab.

Finally how to forget the technical support of Giovanni and Salvatore and the other people of the workshop as Francesco and Mr. Bruno De Nardo.

In this last year, I had the great opportunity to spend a period at the University

of Cambridge in the BSS group , I'm thankful for giving me this opportunity to Prof. Eugene Terentjev. I would like also to say thanks to Francesca Serra and all the other guys I met in Cambridge they all were very kind with me and I am sure that our friendship will continue and that our roads will meet again.

Vorrei ancora ricordare e ringazziare un folt gruppo di persone che non fanno parte della vita dei laboratori ma con cui ho trescorso dei splendidi momenti da quanto è cominciata questa avventura, comminciando dai miei genitori e spingendomi fino ai miei compagni di viaggio di cui ormai in "appartamento" ne è rimasta solo una manciata di reduci tra cui Leonardo, Antonio mio fratello Mimmo, e ancora Anna e Pamela e quanche altro che non mene vorrà se non trova il suo nome tra queste righe. Penso che un doveroso ringraziamento vada a Silvio Calvelli che con grande pazienza ha curato l'impaginazione e la grafica di questo lavoro.

Infine vorrei mandare un bacio a Sonia che in quest'ultimo periodo è entrata a fare parte della mia vita, e che ogni giorno fa si che le mie giornate abbiano più senso e siano più piacevoli.

Now I would like to apologize to all that persons that reading these pages did not find their name, all you guys have a place in my mind

Thank you all

Ariosto

Contents

Introduction

Liquid crystals, constituting an actual phase of matter, were discovered only in 1888. They remained a scientific curiosity until the late 1960s, when liquid crystal displays (LCDs) were invented. Today, liquid crystals are the technology of choice for the multi-billion dollar flat panel display industry. The development of LCDs has fueled much of the liquid crystal research in the past 40 years. The subsequent maturing of the LCD technology, however, resulted in increased exploration in new directions in the liquid crystal research. This in turn gave rise to beautiful results and unexpected advances in a wide variety of areas, to the extent of suggesting a renaissance in the field. Photonics and lasing in liquid crystal materials represents one such advance.

Nowadays lasers are considered as an essential tool in our society, they have found a wider use in many fields of science and technology as well as on a daily basis. From digital players to the telecommunications industry to the medicine, where they found use for high precision surgery, lasers are spread around the all common technologies. This is why this particular field of physics is being nowadays privileged and it is attracting a great interest from both practical and fundamental points of view. Moreover the ongoing developments in nanotechnology have led to the quest for nanolasers. Photonic band gap materials with the potential of allowing comparable control over light are a subject of great interest today.

Liquid crystals can spontaneously form periodic dielectric structures and, in particular, cholesteric liquid crystals have the potential to behave as self-assembled photonic band gap materials. Due to the supermolecular helical structure, cholesteric liquid crystals show many peculiar properties, in particular the capability to reflect light selectively according to the Bragg law.

Since they possess these properties of selective reflection and refractive index modulation, cholesteric liquid crystals can be considered as photonic crystals and can be good candidates in forming optical resonators for distributed feedback lasers, with a noticeable interest in science and applications.

This thesis studies the laser effect from cholesteric liquid crystals as well as from cholesteric elastomers, exploiting the fluorescence properties of some molecules that can be used as gain media. The high sensitivity of the cholesteric helix to the external factors is one of the main advantages in using these materials. In fact this results in the possibility to tune the position of the photonic band gap by different mechanisms, allowing to achieve tuning of the laser emitted wavelength. The major limit of the these laser systems is their low applicability. Even if they are based on well known technologies and are easy to handle, the low stability of the emitted lasing is their main drawback. This thesis also describes the work devoted to overcome the problem of stability presenting several experimental results that allow to improve the laser performances.

The thesis is divided mainly in two parts: the first part is devoted to all basic concepts behind these systems, presenting the theory and the experimental approaches to obtaining the laser effect, while the second part describes the original experimental results obtained during the three years of this work.

Chapter 1 is an introduction to liquid crystals with their principal characteristics, pointing our attention on cholesteric materials with their peculiar optical and photonic properties. Then it is given a brief introduction of liquid crystal polymers and elastomers including the description of their behavior under stretching. Finally we mentioned the photonic crystals and their link with cholesterics.

Chapter 2 gives an unified picture for wave propagation in a periodic structure. In this chapter it is highlighted the presence of a forbidden wavelength range for wave propagating in layered media as well as in cholesteric liquid crystals. The concept of density of states is then introduced at the end.

After the introduction of the concept of stop band in periodic media, in **Chapter 3** it is presented an overview of the theory of optical absorption and emission in atoms and in molecules, which is the basis concept for understanding the classical laser mechanisms. Then it is described how, combining the presence of a stop band with the fluorescence properties of some molecules, the laser effect in dye doped cholesteric liquid crystals can arise.

Chapter 4 starts the second part of the thesis. In this chapter we collected

the experimental results obtained using cholesteric liquid crystals, describing all the improvements achieved in terms of stability and tunability of the cholesteric lasers. This chapter is closed showing how all the experimental results were included in the development of several prototypes.

Chapter 5 then gives a description of a final original result obtained for the first time using cholesteric liquid crystal elastomers. It describes the synthesis of materials and all the efforts to obtain a homogeneous elastomer film that can act as tunable selective mirror and finally its inclusion in a laser system, where the lasing tuning is obtained by uniaxial mechanical stretching.

At the end, in **Chapter 6**, we will present further possible developments as a new kind of device that allows the detection of the UV radiation in relation with the human skin behavior under sun light.

Part I

Introductive Theory

Chapter 1

Liquid Crystals: Fundamental aspects

1.1 History

Liquid crystal materials have been observed for over a century but were not recognized as such until 1880s.

In 1888 Friedrich Reinitzer an Austrian botanist, interested in the biological functions of cholesterol in plants, was looking at the melting behavior of an organic substance related to cholesterol (the structure of cholesterol was still unknown). Nowadays we know that the observed substance was cholesteril benzoate, the first liquid crystal. He observed a strange phenomenon and was struck by the fact that the substance melted to a cloudy liquid at 145.5 C and became a clear liquid at 178.5 C.

Puzzled by his discovery, Reinitzer turned for help to the German physicist Otto Lehmann, who was an expert in crystal optics. Lehmann became convinced that the cloudy liquid had a unique kind of order. in contrast, the transparent liquid at higher temperature had the characteristic disordered state of all common liquids. Eventually he realized that the cloudy liquid was a new state of matter and coined the name "liquid crystal", illustrating that it was something between a liquid and a solid sharing important properties of both.

The new idea was challenged by the scientific community and some scientists

claimed that the newly discovered state was probably just a mixture of solid and liquid components. But between 1910 and 1930 conclusive experiments and early theories supported the liquid crystal concept, at the same time new types of liquid crystalline states of order were discovered.

In these years (1922) the French scientist Georges Friedel suggested the classification scheme which is used today with different phases of liquid crystals.

Today, thanks to Reinitzer, Lehmann and their followers, we know that literarily thousand of substances have a diversity of other states. These strange forms of matter which piqued up the curiosity of scientists at the end of the last century has grown into an enormous industry with a great variety of applications and is still growing.

1.2 What are liquid crystals

Materials in nature can be divided into different phases also called state of matter, depending on the mobility of the individual atoms or molecules. The obvious states are the solid, the liquid and the gaseous state. Although the three categories seem very defined, the borders between the different states are not always clear. Apart from the three familiar states there exist a large number of other intermediate phases. Liquid crystals are an important intermediate phase which exhibits features from both solid and fluid states, they have the ordering properties of solids but they flow like liquids. Liquid crystals for examples can be composed of moderate size organic molecules which tend to be elongated like a cigar. The figure bellow shows the molecular structure of a typical rod-like liquid crystal molecule. It consists of two or more rings systems connected by a central linkage group.

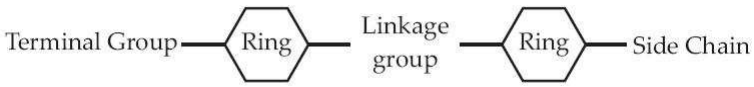

Figure 1.1: *Liquid crystals building blocks*

The presence of the rings provides the short range molecular forces needed to form the mesomorfic phase, but also affect the electrical and elastic properties.

The chemical stability of liquid crystals, their resistence to e.g. moisture or ultraviolet radiation, depends strongly on the central linkage group (compounds with single bond in the center are among the most stable ones). At one side of the rings there is a long side chain which strongly influences the elastic constants and the transition temperatures of the liquid crystal phase. At the other end, a terminal group is connected, which determines the dielectric constant and its anisotropy.

1.3 Liquid crystal phases

There are many different types of liquid crystal phases, which can be distinguished based on their properties. Liquid crystal materials not always be in an LC phase (just as water is not always in the liquid phase: it may also be found in the solid or in gas state)(fig.).

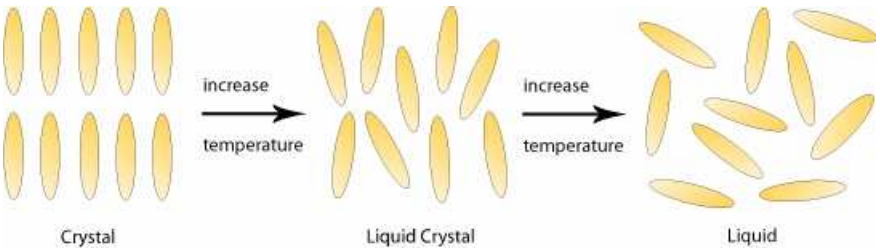

Liquid crystals can be divided into thermotropic and lyotropic LCs. Thermotropic LCs exhibit a phase transition into the LC phase as temperature is changed, whereas lyotropic LCs exhibit phase transition as a function of the concentration of mesogens in a solvent (typically water).

Following the nomenclature proposed by Friedel, thermotropic liquid crystals are classified broadly into three types: Nematic, Cholesteric and Smectic.

1.3.1 Nematic phase

The nematic liquid crystal has a high degree of long range orientational order of the molecules, but no long range of translational order.

Thus it differs from the isotropic liquid in that the molecules are spontaneously oriented with their long axis approximately parallel to a preferred direction that can be described by a unit vector, the so called nematic director $\hat{n}$.

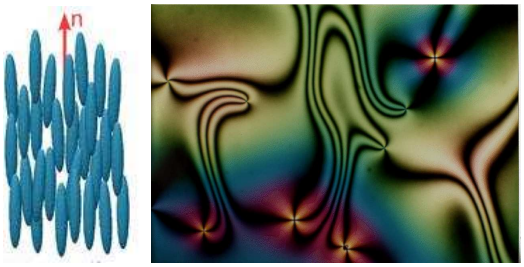

Figure 1.2: *Orientation of molecules in the nematic liquid crystalline phase - typical texture of the nematic with common defects.*

The preferred direction usually varies from point to point in the medium, but a homogeneously aligned specimen is optically uniaxial, positive and strongly birefringent. The mesophase owes its fluidity to the ease with which the molecules slides past one another while still retaining their parallelism.

1.3.2 Cholesteric phase

The cholesteric phase is also a nematic type of liquid crystal except that it is composed of optically active molecules. As a consequence the structure has a screw axis superimposed normal to the preferred molecular direction.

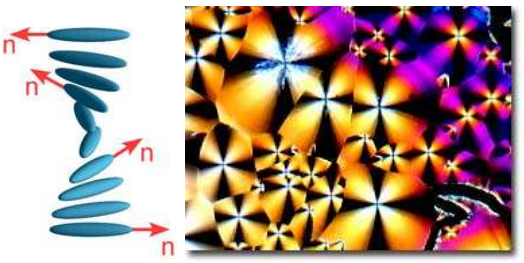

Figure 1.3: *Orientation of molecules in the cholesteric liquid crystalline phase.*

Optically inactive molecules or racemic mixtures results in a helix of infinite pitch which corresponds to the true nematic. Thermodynamically the cholesteric is very similar to the nematic as the energy of twist form only a minute part ($\sim 10^{-5}$)of the total energy associated with the parallel alignment of the molecules.

A very important feature of the cholesteric pahse is the pitch, p, which is defined as the distance it takes for the director to rotate one full turn in the helix as illustrated in the following drawing (fig.1.4).

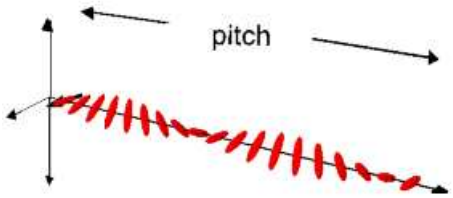

Figure 1.4: *helical pitch of the cholesteric structure.*

The spiral arrangement of the molecules in this mesophase is responsible for its unique optical properties, viz, selective reflection of circularly polarized light and a rotatory power about a thousand times greater than that of an ordinary optically active substance, as we will see later in this chapter.

1.3.3 Smectic phase

Smectic liquid crystals have stratified structures but a variety of molecular arrangements are possible within each layer with their centers irregularly spaced in a "liquid-like" fashion. The thickness of the layer is of the order of the length of the free molecule. The inter-layer attractions are weak as compared with the lateral forces between molecules and in consequence the layers are able to slide over one another relatively easily. Thus this mesophase has fluid properties, though as a rule it is very much more viscous than the nematic mesophase. There is a very large number of smectic phases, all characterized by different types of degrees of positional and orientational order.

In the smectic A phase the molecules are oriented along the layer normal, and there is no particular positional order within the layer.

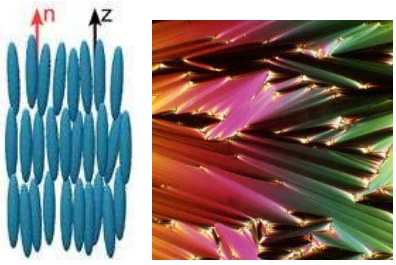

Figure 1.5: *Orientation of molecules in the Smectic A liquid crystalline phase.*

1.4 The order parameter

In liquid crystals, a local preferred orientation can be always found, its direction can be usually indicated by a unit vector called *director*, $\hat{n}$ as mentioned previously. It represents the average molecular direction in a volume small enough to make meaningful talking about a molecular direction and large enough to contain a great number of molecules which make meaningful an averaging procedure.

The grade of order in most of the liquid crystal phases can vary depending on different factors the most important of them is the temperature. It is necessary, at this point, to describe the state of orientational order of molecules in a quantitative way.

Rigid rods are the simplest type of objects that allow liquid crystal behavior, in particular nematic behavior. The rod is assumed to have complete cylindrical symmetry about its major axis and to be non polar ($\hat{n} = -\hat{n}$). The state of alignment of the rods can be described by a distribution function.

Generally a one-particle distribution function $P = (\mathbf{r}, \Omega)$, presenting the probability to find a molecule with orientation Ω at position $\mathbf{r}$, can be introduced for the purpose to find the proper order parameter which describe the LC phases order.

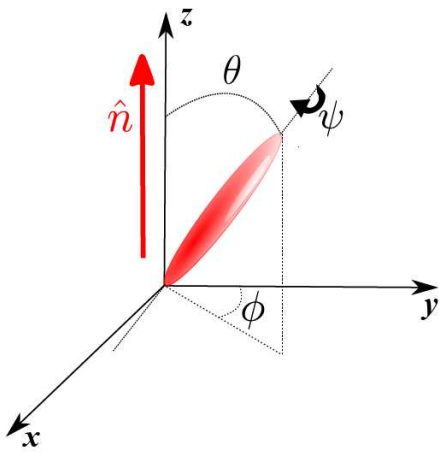

Figure 1.6: *Euler angles and alignment direction of an LC molecule.*

Here Ω is the solid angle which includes the three Euler angles ψ (rotation along the longitudinal molecular axis), ϕ (precession of the longitudinal molecular

axis along a cone surface around axis z) and θ (deviation of the longitudinal molecular axis from the director).

From fundamentals of the group theory the transitional and orientational degrees of freedom can be treated separately,

$$P(\mathbf{r}, \Omega) = P(\mathbf{r}) \times P(\Omega)$$

then the distribution function can be written as *group* product of both them. In particular for the isotropic liquid as well as for the nematic phase, where no positional order is present, the distribution function can be written as, $P(\mathbf{r}, \Omega) = \rho P(\Omega)$ where $\rho = const$ is the density.

Consider now the *orientational distribution function* $f(\Omega)$ and $f(\Omega)d\Omega$ which gives the fraction of molecules with Euler angles ϕ and $d\phi$, θ and $d\theta$, ψ and $d\psi$. In the uniaxial phase as the nematic phase, due to the cylindrical symmetry, there isn't any order for the angles ϕ and ψ, thus the only element with an order degree is the angle θ. Then the orientational distribution function can be written as $f(\theta)$ and , again for symmetrical reasons $f(\theta) = f(\pi - \theta)$.

As any axial symmetric function, $f(\theta)$ can be expanded in a series of Legendre polynomials $P_i \cos\theta$,

$$f(\theta) = (1/2)[1 + a_1 P_1(\cos\theta) + a_2 P_2(\cos\theta) + a_3 P_3(\cos\theta) + a_4 P_4(\cos\theta) + ...] \quad (1.1)$$

according to the following formula:

$$P(x) = \frac{1}{2^n n} \cdot \frac{d^n[(x^2-1)^n]}{dx^n} \quad (1.2)$$

In order to find the coefficients a_L of the series 1.1 it is necessary to multiply both sides by $P_L(\cos\theta)$ and integrate over θ, using the orthogonality, and finally it is possible to write the orientational distribution function as

$$f(\theta) = (1/2)[1 + 3 < P_1(\cos\theta) > P_1(\cos\theta) + 5 < P_2(\cos\theta) > P_2(\cos\theta) + 7 < P_3(\cos\theta) > P_3(\cos\theta) + 9 < P_4(\cos\theta) > P_4(\cos\theta) + ...]. \quad (1.3)$$

In the liquid crystal case, the polynomials depend on the angle θ, so $x = \cos\theta$, where $\cos\theta$ is the projection of θ on the axis z.

The distribution function contains all the information about the state of order in the material, but it would be convenient to represent this state of order not as a function but as a number, an *order parameter* which took the value 0 for complete disorder, and 1 for the perfect order. For uniaxial molecules with inversion centers (head to tale symmetry of a cylinder), as in most LCs where both directions of the director $\hat{n}$ ($+\hat{n}$ and $-\hat{n}$) are equivalent, avoiding the description of a polar phase, only the even terms are taken into account. Then the amplitude of each term of the series can be considered as an order parameter, and it is possible to write briefly

$$f(\theta) = f(\cos\theta) = \sum_0^\infty \frac{1}{2}(4l+1)S_{2l}P_{2l}(\cos\theta) \tag{1.4}$$

and the coefficients

$$S_{2l} =< P_{2l}(\cos\theta) >= \int_\pi^0 P_{2l}(\cos\theta)f(\theta)d(\cos\theta) \tag{1.5}$$

are the number we are looking for:

$$\begin{aligned} &S_0 \equiv 1 \\ &S_1 =< P_1(\cos\theta) >\equiv< \cos\theta > \\ &S_2 =< P_2(\cos\theta) >\equiv 1/2 < 3\cos^2\theta - 1 > \\ &\dots \end{aligned}$$

Afterwards the order parameter that better describe the liquid crystal structure must be chosen between these coefficients, the first S_0 is meaning less because is angle independent, the second S_1 is an odd function incompatible with $\hat{n} = -\hat{n}$, then the next is the coefficient

$$S_2 = 1/2 < 3\cos^2\theta - 1 >$$

which describe the quadrupolar order. It looks suitable in describing the order of liquid crystal phases.

1.5 The distortion free energy

Let us impose on a nematic a certain state of distortion described by a variable director $\hat{n}(\mathbf{r})$. We make the following assumptions about this distorted system,

the variations of $\hat{n}$ are slow on the molecular scale

$$a\nabla\hat{n} \ll 1$$

If F_d is the free energy due to the distortion of $\hat{n}$, F_d will vanish if $\nabla\hat{n} = 0$ and it may be expanded in power of $\nabla\hat{n}$.

We can write an expression for the distortion free energy F_d for a conventional (uniaxial non-polar) nematic in the form

$$F_d = \frac{1}{2}K_1(\nabla \cdot \hat{n})^2 + \frac{1}{2}K_2(\hat{n} \cdot \nabla \times \hat{n})^2 + \frac{1}{2}K_3(\hat{n} \times \nabla \times \hat{n})^2 \qquad (1.6)$$

The constants K_1, K_2 and K_3 in the eqn. 1.6 are respectively associated with the three basic types of deformation displayed in the following figure

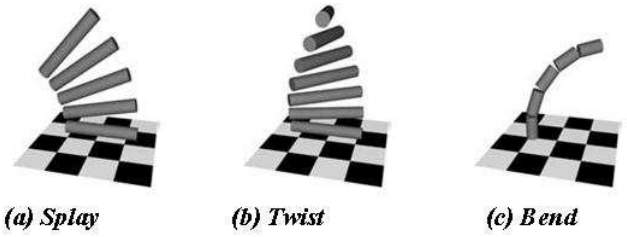

Figure 1.7: *Splay, Twist and Bend distortion of the liquid crystal director.*

$$\begin{aligned} K_1 &: \text{conformations with } \nabla \cdot \hat{n} \neq 0 && \text{(splay)} \\ K_2 &: \text{conformations with } \hat{n} \cdot \nabla \times \hat{n} \neq 0 && \text{(twist)} \\ K_3 &: \text{conformations with } \hat{n} \times \nabla \times \hat{n} \neq 0 && \text{(bend)} \end{aligned}$$

However in many cases the full form of the eqn. 1.6 is still too complex to be of practical use and a further approximation is often useful; this amounts to assuming all the three elastic constants equal

$$K_1 = K_2 = K_3 = K$$

The free energy then takes the form

$$F_d = \frac{1}{2}K\{(\nabla \cdot \hat{n})^2 + (\nabla \times \hat{n})^2\} \qquad (1.7)$$

1.6 Nematic-Isotropic Phase transition

To give a description of the phase transition from the nematic liquid crystal to the isotropic liquid, one must take into account that the nematics are thermotropic liquid crystals and that the scalar order parameter depends on temperature.

Experimentally an abrupt drop of the order parameter at transition temperature has been observed, which is manifestation of first order transition.

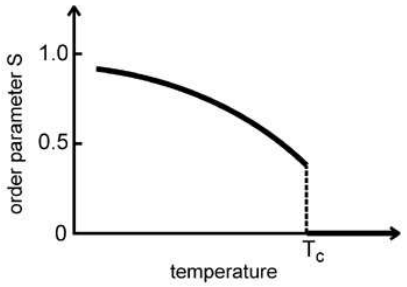

Figure 1.8: *Scalar order parameter vs temperature.*

The graph shows the typical behavior of the scalar order parameter S in function of the temperature, and also the discontinuity at the T_c point. T_c is the nematic isotropic phase transition also called *clearing point*.

1.7 Anisotropy in liquid crystals

The uniaxial symmetry around the director in the liquid crystal phase leads to an anisotropy in many physical properties. For example the refractive index, the dielectric permittivity, the magnetic susceptibility, viscosity and conductivity have different value parallel to the director and perpendicular to it.

1.7.1 Optical anisotropy

The anisotropy of liquid crystals causes light polarized along the director $\hat{n}$ to propagate at a different velocity than light polarized perpendicular to it. As was done previously we can use a second rank tensor to describe the optical properties of the liquid crystal. Each second rank tensor in three dimension can be represented by an ellipsoid. Choosing the coordinate system in such a way that the the ellipsoid would be oriented with its principal axes along the coordinate axes, the tensor will be diagonalize. In general, the refractive index is related

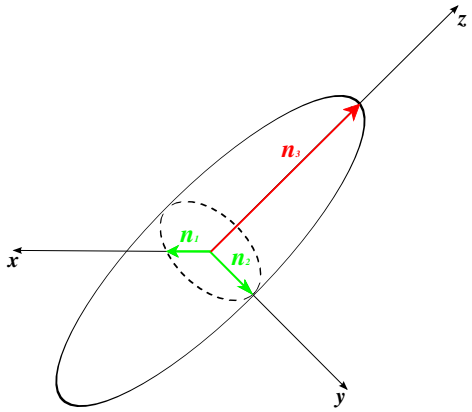

Figure 1.9: *Ellipsoid of indices and optical indicatrix.*

to the response of matter to an electric field. Then it depends on dielectric permittivity ε, according $n^2 = \varepsilon$ at optical frequencies. Then the ellipsoid of indices can be written as

$$\frac{x^2}{n_1^2} + \frac{y^2}{n_2^2} + \frac{z^2}{n_3^2} = 1$$

In a uniaxial liquid crystal only two of the three refractive indices are different, $n_1 = n_2 \equiv n_o$ that is the ordinary refractive index and $n_3 = n_e$ that is the extraordinary refractive index.

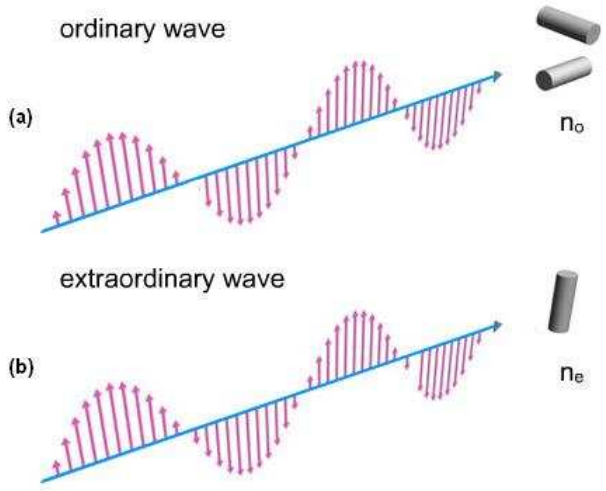

Figure 1.10: *Light propagation in liquid crystals along the normal to the optical axis: (a) ordinary beam; (b) extraordinary beam; n_e is the extraordinary refractive index and n_o is the ordinary refractive index*

The first one, n_o, is measured for the light wave where the electric vector vibrates perpendicular to the optical axis (ordinary wave). The index n_e is measured for the light where the electric vector vibrates along the optical axis (extraordinary wave), fig 1.10. Then the birefringence is given by:

$$\Delta n = n_e - n_o$$

Usually, $n_e > n_o$ and, therefore, Δn is positive and varies in the range from values close to zero to about 0.4. The indices n_o and n_e are measured for the light propagating along or normal to the optical axis. In the case when the direction of the light propagation is tilted with respect to the optical axis (fig.1.11), the

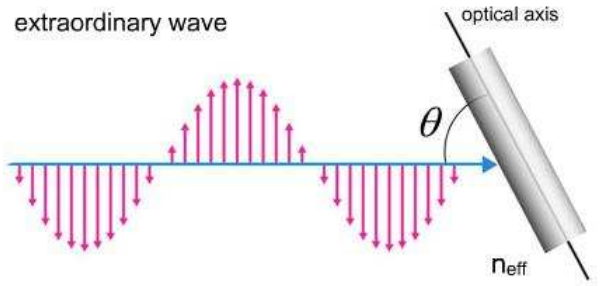

Figure 1.11: *Light propagation through a liquid crystal with a generic angle.*

refractive index for the ordinary wave is equal to n_o but the refractive index for the extraordinary wave is equal to some effective value given by:

$$n_{eff} = \frac{n_e n_o}{\sqrt{n_e^2 \cos^2\theta + n_o^2 \cos^2\theta}}$$

where θ is an angle between the optical axis and the light propagation direction. Then the birefringence is $\Delta n = n_{eff} - n_o$.

1.8 Optical properties of Cholesteric Liquid Crystals

Cholesteric liquid crystals show very distinctly that molecular structure and external fields have a profound effect on cooperative behavior and phase structure. As was already presented in sec.1.3.2 CLCs posses a supermolecular periodic helical structure due to the chirality of molecules. The spatial periodicity (helical

pitch) of cholesterics can be of the same order of magnitude as the wavelength of the visible light. If so, a visible Bragg reflection occurs. On the other hand, the helix pitch is very sensitive to the influence of external conditions. A combination of these properties leads to the unique optical properties of cholesterics which are of both scientific and practical interest.

The cholesteric phase appears in organic compounds which consist of elongated (nematogenic) molecules without mirror symmetry (chiral molecules). Typical representatives of these compounds are the derivatives of cholesterol. Thus, chiral nematic liquid crystals are generally called cholesteric liquid crystal, although the name chiral nematic is more correct. The cholesteric structure occurs not only in the pure chiral compounds, but also in mixtures of achiral nematics with optical active (chiral) mesogenic or non-mesogenic dopants (induced cholesteric systems).

1.8.1 The planar texture

In the ideal state the cholesteric present a helical arrangement (sec. 1.3.2) in which the director **n(r)** varies in space according to the law:

$$\begin{aligned} n_x &= \cos\theta \\ n_y &= \sin\theta \\ n_z &= 0 \end{aligned} \tag{1.8}$$

$$\theta = q_0 z + \text{constant} \tag{1.9}$$

where we have taken the helical axis along z. A cholesteric single crystal, described by equations (1.8) and (1.9) can often be obtained in thin slabs provided that the boundary conditions on both sides of the slab are tangential.

The nominal pitch of the helical structure is equal to $2\pi/q_0$; however since the state (**n**) and (-**n**) are indistinguishable, the periodicity interval along z is $L = P/2 = \pi/q_0$.

It is necessary also to remember the question of sign: If the (xyz) frame used in eqn. 1.8 is a right-handed frame, and if the wave-vector q_0 is positive, we have a right-handed helix. If q_0 is negative, we have a left-handed helix.

Bragg reflections

A light beam of angular frequency ω, is sent parallel to the helical axis (z). In a zero-order approximation, we may think of the cholesteric as a nearly isotropic medium, with a certain average index of refraction $\bar{n}$. The optical wavelength in the medium is then

$$\lambda = \frac{2\pi c}{\bar{n}\omega}. \tag{1.10}$$

We may also define the beam by the wave-vector $\mathbf{k}_0$, along z, and the magnitude $\omega\bar{n}/c$.

In the next approximation, we note that the medium is not exactly isotropic; the optical properties are modulated with a spatial period q_0. This may in principle give rise to Bragg reflections, provided

$$2L = m\lambda \qquad (m = \text{integer}). \tag{1.11}$$

Experimentally, one does observe *one* Bragg reflection ($m = 1$). The higher order reflection are forbidden for normal incidence, due to a specific form of the dielectric permittivity tensor of the cholesteric. The polarization features of the waves are also remarkable.

1. The reflected light is circularly polarized: at any instant t the electric field pattern in the reflected wave is a helix, identical in shape to the cholesteric helix (see fig.1.12).

2. If we analyze the incident wave into two components of opposite circular polarizations, we find that only one component is strongly reflected - i.e. the component for which the instantaneous electric pattern is again identical in shape to the cholesteric helix. The other component is transmitted without any significant reflection through the slab. These features are also displayed in figure 1.12.

All these properties can be explained in terms of scattering amplitude α, according to the following equation:

$$\boldsymbol{\alpha = f \cdot \varepsilon(q) \cdot i} \tag{1.12}$$

where $\mathbf{f}$ and $\mathbf{i}$ represent the polarizations of the reflected waves (of wave-vector $\mathbf{k}_1$) and of the incident wave (wave-vector $\mathbf{k}_0$). $\mathbf{q}=\mathbf{k}_0 - \mathbf{k}_1$ is the scattering wave-vector, and $\varepsilon(\mathbf{q})$ is the Fourier transform of the dielectric tensor. In the present case, the three vectors $\mathbf{k}_0$, $\mathbf{k}_1$ and $\mathbf{q}$ will be parallel to (z). As explained in sec.

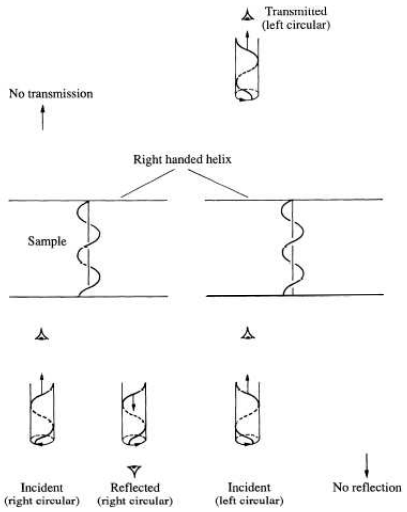

Figure 1.12: *Bragg reflection and transmission by a slab in the planar texture the cylinder with S represents "snapshots" of the electric field* $\boldsymbol{E}$ *associated with one wave. The vertical arrows give the direction of propagation. The circle C shows the rotation of* $\boldsymbol{E}$ *as seen by an observer at one fixed point in space. The reflected wave emitted by the sample is an image of the cholesteric helix, translated downwards Examinations of the corresponding project path C shows that it is right circular.*

1.3.2, at any point $\mathbf{r}$ a cholesteric behaves locally like a uniaxial material: the dielectric tensor may thus be written

$$\epsilon_{\alpha\beta}(\mathbf{q}) = \epsilon_{\perp}\delta_{\alpha\beta} + (\epsilon \parallel -\epsilon_{\perp})n_{\alpha}(\mathbf{r})n_{\beta}(\mathbf{r}). \tag{1.13}$$

Using equation 1.8 for $\mathbf{n(r)}$ we can compute $\varepsilon(\mathbf{r})$ and then $\varepsilon(\mathbf{q})$. For $q \neq 0$ a constant term like $\epsilon_{\perp}$ does not contribute. To illustrate the calculation let us discuss the (xx) component of dielectric tensor

$$\begin{gathered}\epsilon_{xx}(\mathbf{q}) = \epsilon_{\alpha}\int d\mathbf{r}\cos^2(q_0 z)e^{\imath qz} \\ (\epsilon_{\alpha} = \epsilon_{\parallel} - \epsilon_{\perp}).\end{gathered} \tag{1.14}$$

Writing

$$\cos^2(q_0 z) = \frac{1}{2} + \frac{1}{4}(e^{2\imath q_0 z} + e^{-2\imath q_0 z}) \tag{1.15}$$

and eliminating again the constant term, we see that the integral 1.14 vanishes except when $q = \pm 2q_0$. Let us take $q_0 > 0$ (right handed helix). Then the case

$q = -2q_0$ corresponds to k_1 larger than k_0, and is forbidden, since the frequency of the scattered wave must coincide with ω.

The case of interest is $q = 2q_0$ corresponding to $k_0 = -k_1 = q_0$. Then

$$\epsilon_{xx}(2q_{0)} = \frac{1}{4}\epsilon_\alpha V$$

where V is the sample volume.

Similar manipulation give the other components of $\varepsilon(2q_0)$: the only non-vanishing component correspond to polarizations in the x,y-plane, and the resultant 2×2 matrix is

$$\begin{aligned} \hat{\epsilon}(2q_0) &= \frac{1}{4}\epsilon_\alpha V \hat{M} \\ \hat{M} &= \begin{bmatrix} 1 & \imath \\ \imath & -1 \end{bmatrix} \end{aligned} \tag{1.16}$$

Omitting the constant factor, the polarization of the reflected wave **f** is related to the incident polarization **i** by

$$\begin{bmatrix} f_x \\ f_y \end{bmatrix} = \hat{M} \begin{bmatrix} i_x \\ i_y \end{bmatrix} \tag{1.17}$$

or, explicitly,

$$\begin{aligned} f_x &= i_x + \imath i_y \\ f_y &= \imath i_x - i_{y.} \end{aligned} \tag{1.18}$$

We see that $f_y = +\imath f_x$: the reflected light is circularly polarized. In one case we do not get a reflected wave: namely $i_y = \imath i_x$; this defines the transmitted wave of fig 1.12

We may also explain why the higher-order Bragg reflection are forbidden, in terms of the matrix amplitude $\hat{M}$.

Let us look for instance at the reflection $m = 2$, which would correspond to $q = 4q_0$. This can be obtained by scattering from the initial state k_0 to a virtual photon state $k_0 - 2q_0$, followed by a second scattering from $k_0 - 2q_0$ to $k_0 - 4q_0$. The matrix amplitude for this process is proportional to M^2. But, from eqn (1.16), it is easily verified that $\hat{M}^2 = 0$. The proof can be extended to higher-order processes involving more than one virtual photon, and larger values of m; all higher Bragg reflections are forbidden for normal incidence.

Let us now discuss briefly the case of oblique incidences. Here, we observe

reflections with the geometrical condition

$$2L\cos r = m\lambda \tag{1.19}$$

where r is the angle of the refracted beam in the slab (related to the angle of incidence i by $\sin i = \bar{n}\sin r$). The main differences from the case of normal incidence are that:

1. All orders ($m = 1, 2, 3, ...$) are observed.

2. The polarizations are elliptical.

The optical properties observed on a planar cholesteric structure (Bragg reflection and optical rotation) are very spectacular: when P corresponds to an optical wavelength in the visible range, the sample show some very bright colours in reflection. Also the optical rotations are huge.

1.9 Liquid crystal polymers (LCP)

Liquid crystal polymers are a class of materials that combine the properties of polymers with those of liquid crystals. These "hybrids" show the same mesophases characteristic of ordinary liquid crystals, yet retain many of the useful and versatile properties of polymers.

In order for normally flexible polymers to display liquid crystal characteristics, rod-like elements must be incorporated into their chain. The placement of the mesogens palys a large role in determining the type on LCP that is formed. *Main-chain liquid crystal polymers* are formed when the mesogens are themselves part of the main chain polymer.

These stiff components along the chain allow the polymer to orient in a manner similar to ordinary liquid crystals, and thus display liquid crystal characteristics. The mesogens are usually separated or "decoupled" by a flexible bridge called spacer fig. (1.13). Decoupling of the mesogens provides for independent movement of the molecules which facilitates the proper alignment.

Conversely, *side-chain liquid crystal polymers* are formed when the mesogens are connected as side chains to the polymer by a *spacer*. These kind of liquid crystal polymers have three major structural components: *the backbone, the spacer and the mesogen*. The versatility of side-chains arises because these structure can be varied in a number of ways.

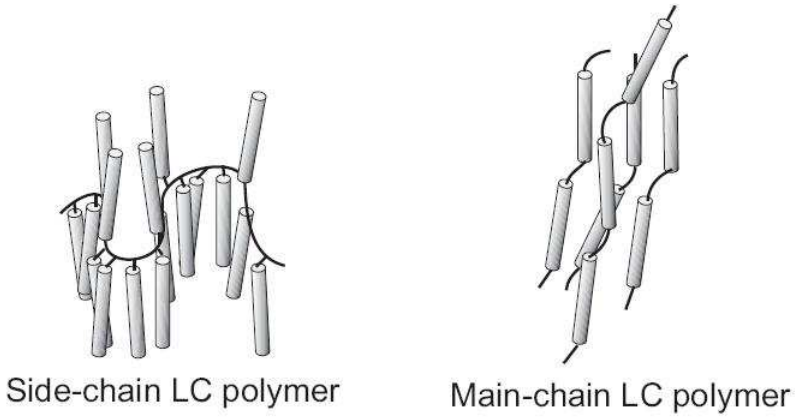

Figure 1.13: *Schematic view of Liquid Crystal Polymers (LCP).*

The backbone of a side-chain liquid crystal polymer is the element that the side chains are attached to. The structure of the backbone can be very important in determining if the polymer shows liquid crystal behavior. Polymer with rigid backbone typically have high glass transition temperature and thus liquid crystal behavior is difficult to observe, on the contrary a more flexible backbone can lower this temperature allowing the liquid crystal behavior more easily.

The mesogen is perhaps the most important part of a side chain liquid crystal polymer. It is the alignment of these groups that causes the liquid crystal behavior. Usually, the mesogen is made up of a rigid core (as was previously described sec. 1.2). Like their main chain counterparts, mesogens attached as side groups on the backbone are able to orient because **the spacer** allows for independent movement. The structure of the spacer is an important determining factor in the side chain liquid crystal polymers. Accordingly, the spacer length has a profound effect on the temperature and type of phase transitions. Usually the glass transition temperature decreases with increasing the spacer length. Short spacers lead to nematic phases, while longer spacers lead to smectic phases.

1.10 Liquid crystal elastomers (LCE)

Liquid crystal elastomers bring together, as nowhere else, three important ideas: *orientational order* in amorphous soft materials, *responsive molecular shape* and *quenched topological constraints*. Classical liquid crystals, as we have already seen in this chapter, are typically fluids of relatively stiff molecules with long range

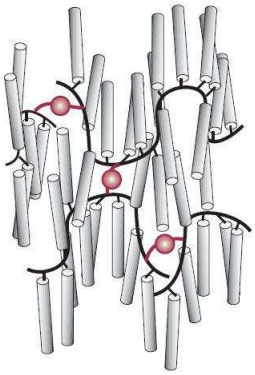

Figure 1.14: *Schematic view of Liquid Crystal Elastomers (LCE).*

orientational order.

Long polymer chains, with incorporated rigid anisotropic units can also order nematically and thus form liquid crystalline polymers. Linking the polymer chains together into a gel network fixes their topology, and the melt become an elastic solid, *a rubber*. Then Nematic and consequently Cholesteric, as well as Smectic elastomers are networks of polymer chains that have intrinsic liquid crystalline ordering in addition to their conventional high polymer properties.

In rubber, monomers remain highly mobile and thus liquid-like. Thermal fluctuations move the chains as rapidly as in the melt, but only as far as their topological crosslinking constraints allow. These loose of constraints make the polymeric liquid into a weak, highly extensible material. Nevertheless, rubber is a solid in that an energy input is required to change its macroscopic shape, in contrast to a liquid which would flow in response. Equivalently, a rubber recovers its original state when external influences are removed.

1.10.1 Cholesteric liquid crystal elastomers

There are different types of liquid crystal polymers and elastomers usually prepared from reactive mesogenic units. Their aligned structure is fixed by thermal or UV initiated reaction to yield a mechanically strong film.

Adding polymer properties into a liquid crystal phase makes LC polymers and elastomers an anisotropic solid with unusual properties [7]. The system can show a complicated response to a mechanical strain since a conformational change of the polymer chain affects the liquid crystal phase directly. They can be used for con-

verting mechanical energy into electrical or optical response and vice versa. Many studies have been conducted for the purpose of artificial muscles, light scattering electro-optical switches, display materials, electro- or photo-controllable micro- or nano-machinery, electrically switchable color-tunable reflectors, full-color reflective displays, and fine-tunable low-threshold mirror-less lasing [8]. In the case of

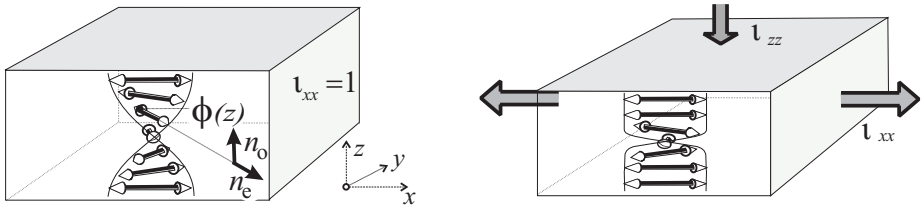

Figure 1.15: *A schematic view of CLC elastomers under uniaxial strain. The strain is imposed along x. Contraction of y direction is not shown in order to simplify the diagram.*

cholesteric liquid crystal elastomers, mechanical deformation directly affects the selective reflection, the unique optical property of cholesteric liquid crystal phase. The opto-mechanical response of the CLC elastomers has been theoretically studied by Warner and Terentjev [7, 9], followed by experimental studies [10]. When the CLC elastomer is stretched along x direction, perpendicularly to the helical axis z it is subjected to a contraction (figure 1.15), the director angle ϕ in the xy plane is given by the equation:

$$\tan 2\phi = \frac{2\iota_{xx}\iota_{yy}(r-1)\sin 2\widetilde{q}z}{(r-1)(\iota_{xx}^2+\iota_{yy}^2)\cos 2\widetilde{q}z + (r+1)(\iota_{xx}^2-\iota_{yy}^2)} \tag{1.20}$$

where ι_{xx}, ι_{yy} are strains of the system in x and y direction, respectively, r is the chain anisotropy given by:

$$r = \frac{l_{\parallel}}{l_{\perp}} \tag{1.21}$$

where $l_{\parallel}$ and $l_{\perp}$ means effective step length of a random walk representing the polymer chain parallel and perpendicular to the director. The value of r is estimated as 1.2 approximately in the materials that will be studied in this work [10]. $\widetilde{q}z$ is a phase of the compressed helix where the inverse pitch $\widetilde{q}$ becomes q_0/ι_{zz}. This $\widetilde{q}z$ also represents a z position along the helical axis where the position is defined relatively to the cholesteric pitch.

Considering incompressibility of the material, $\iota_{xx}\iota_{yy}\iota_{zz} = 1$ has to be main-

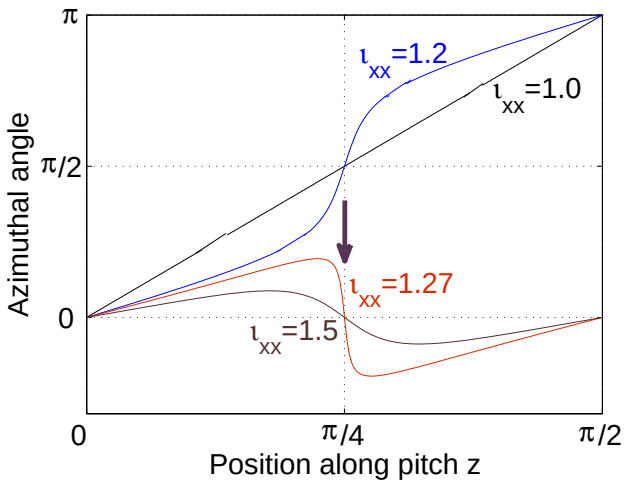

Figure 1.16: *The director angle ϕ against the position along pitch z. The helical structure at $\iota_{xx} = 1$ shows a linear increase of ϕ against the position $\widetilde{q}z$. The curvature changes when ι_{xx} is increased, and then the system experiences a sudden transition (shown by an arrow) where the original helical structure becomes a non-chiral periodic structure.*

tained. In an isotropic elastomer, $\iota_{zz} = \iota_{yy} = \iota_{xx}^{-1/2}$. In an anisotropic cholesteric elastomer, however, the original theory predicts $\iota_{zz} = \iota_{zz}^{-1/4}$, and $\iota_{yy} = \iota_{xx}^{-3/4}$ [10]. Therefore, the equation 1.20 is simplified as:

$$\tan 2\phi = \frac{2\iota_{xx}^{1/4}(r-1)\sin 2\widetilde{q}z}{(r-1)(\iota_{xx}^{2} + \iota_{xx}^{-3/2})\cos 2\widetilde{q}z + (r+1)(\iota_{xx}^{2} - \iota_{xx}^{-3/2})} \tag{1.22}$$

where ι_{xx} is the externally imposed extension[ref11].

It is important to note that the wavenumber of periodic modulation is given by $\widetilde{q} = q_0/\iota_{zz}$, so the position of the selective reflection bands can be continuously blue-shifted by mechanical deformation.

Figure 1.16 shows how ι_{xx} modifies the director angle ϕ. Without strain, the system shows a simple helix such that ϕ increases linearly from 0 to π along the helix phase $\widetilde{q}z$. However, the curvature changes when ι_{xx} is imposed since the director $\hat{n}$ tends to follow the uniaxial elongation of the sample. The system experiences a sudden transition (as shown by the arrow in figure 1.16) when the strain exceeds a threshold value. In this transition, the middle point ($\widetilde{q}z = \pi/2$) suddenly changes its angle from $\pi/2$ to 0, from a position perpendicular to the strain direction (y) to a position parallel to the direction x. At this point the system loses its original helicity, forming a periodic structure having no phase

chirality.

1.11 Photonic Crystals

The ability to manipulate and control light is one of the foremost goals of modern optics. However, it is also something that nature perfect a long time ago, when the manipulation of light began to influence the survival of many animals. Natural optical systems offer inspiration for new ideas in optical design and could provide shortcuts for developing advanced photonic systems. Some examples of the natural photonic structures are shown in figures 1.17 and 1.18.

Figure 1.17: *Examples of photonic structures in biological systems.*

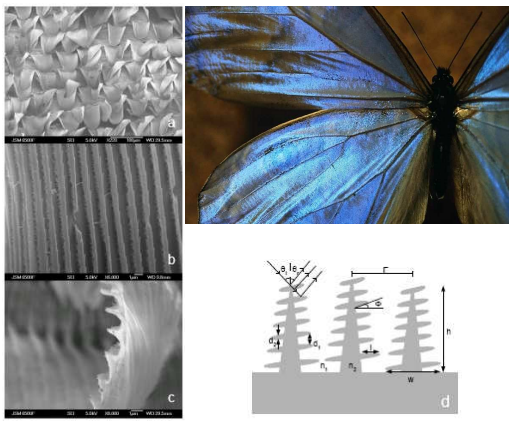

Figure 1.18: *SEM images of Morpho butterfly a) Scale Structure b) Ridges Present on Scales c) Close-up Showing Tree-Like Cross-Section at Ends of Scales d) Diagram of Tree-Like Cross-Section showing Relevant Parameters.*

Some of the most interesting optical systems in nature are hard to miss. They are often brightly colored, metallic looking or strongly iridescent, and stand out from ordinary objects that are colored by pigmentation alone. In the 17th century R.Hooke and I.Newton were among the first to explain the underlying physics of

these systems. They correctly predicted that the iridescent colors of the peafowl feathers and silverfish scales resulted from their physical structure rather than pigmentation. Photonic band gap structures can also be made from a lattice of

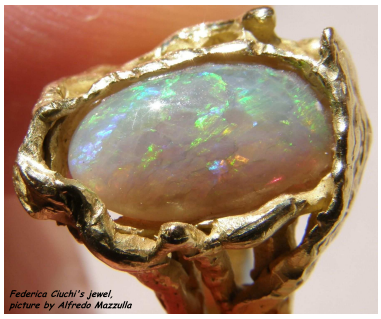

Figure 1.19: *Natural photonic structures in opals.*

high refractive index material embedded within a medium with a lower refractive index. A naturally occurring example of such a material is the opal (fig. 1.19)

Photonic crystals are periodically structured electromagnetic media, generally possessing *photonic band gaps*: ranges of frequency in which light can not propagate through the structure. This periodicity is proportional to the wavelength of light in the band gap, as we will see in the next chapter, is the electromagnetic analogue of the crystalline atomic lattice, where the latter acts on the electrons wavefunction to produce the familiar band gaps, like in semiconductors.

Photonic crystals can be classified into three main groups, that is, one-dimensional (1D), two-dimensional (2D) and three-dimensional (3D) systems, according to the dimensionality of the structure that forms the crystal fig.1.20

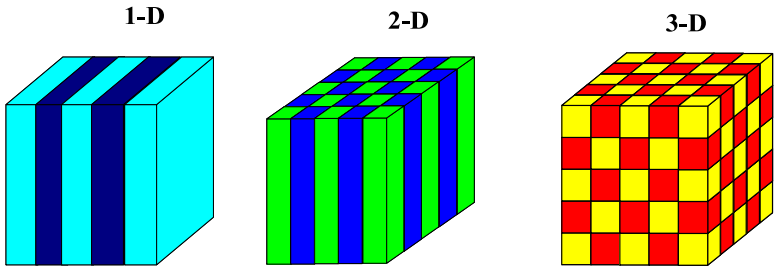

Figure 1.20: *Schematic depiction of photonic crystals periodic in one, two and three dimensions.*

The simplest possible photonic crystal, shown in fig 1.20 consists of alternating layers of material with different dielectric constants. This arrangement is

not a very new idea, the optical properties of such a multilayer film have been widely studied. This photonic crystal can act as a perfect mirror for light with a frequency within a sharply defined gap.

Cholesteric liquid crystals as well as cholesteric elastomers, since their supermolecular helical structure possesses particular properties, as modulation of the refractive index and selective reflection of light. These peculiar properties allow to consider both these materials as natural one dimensional photonic crystals.

Chapter 2

Wave propagation in periodic structures

2.1 Introduction

Electromagnetic wave propagation in periodic media was first studied by Lord Rayleigh in 1887, in connection with the peculiar reflective properties of a crystalline mineral with periodic "twinning" planes. These correspond to a one-dimensional photonic crystals, and he identified that they have a narrow band gap prohibiting light propagation through the planes. This band gap is angle-dependent, due to the differing periodicities experienced by light propagating at non-normal incidences, producing a reflected color that varies sharply with angle. A similar effect is responsible for many other iridescent colors in nature, such as butterfly wings opals and so on, as we have seen in the previous chapter.

Although mutlilayer film received intensive study over the following century, it was not until 100 years later, when Yablonovitch and John in 1987 joined the tools of classical electromagnetism and solid-state physics, that the concepts of omnidirectinal photonic band gaps in two and three dimensions was introduced. This generalization, which inspired the name *"photonic crystal"*, led to many subsequent developments in their fabrication, theory, and application, from integrated optics to negative refraction to optical fibers.

In this chapter we shall discuss a unified picture for wave propagation in periodic structures. We will highlight the presence of a forbidden wavelengths range for waves propagating in layered media and in particular in cholesteric liquid crystals. We will then end the chapter introducing the concept of density

of states.

2.2 Bloch waves

There are some common properties of wave propagation in periodic structures, before discussing these properties, it is important to notice that there is a tuning condition between periodic potentials and wavelength of the propagating waves. In general, it is only for those waves which have wavelength near the period of these structures that substantial effects in wave behavior will be expected. So in the discussion of wave propagation in periodic structures, the tuning condition must be considered.

The range of wavelength of the electromagnetic radiation may vary from γ-rays to visible light to radio waves, so that the lattice spacing of periodic structures for electromagnetic wave should be chosen correspondingly. The waves propagating in periodic structures are not perfectly free. They are constrained to form Bloch waves.

Take an electron in a crystalline solid, the Schrödinger equation is

$$\left[-\frac{\hbar^2}{2m}\nabla^2 + V(\boldsymbol{r})\right]\psi(\boldsymbol{r}) = E\psi(\boldsymbol{r}). \tag{2.1}$$

.

The electron will experience the periodic potential described by (**??**), so its wavefunction $\psi(\mathbf{r})$ and energy E determined by (2.1) will reflect the characteristics of the periodic potential.

The solution of (2.1) should be characterized by a wavefactor $\boldsymbol{k}$, and it will be always possible to take the form

$$\psi_{\boldsymbol{k}}(\boldsymbol{r}) = u_{\boldsymbol{k}}(\boldsymbol{r})f_{\boldsymbol{k}}(\boldsymbol{r}), \tag{2.2}$$

where the function $u_{\boldsymbol{k}}(\boldsymbol{r})$ is assumed to have the same translational symmetry as the lattice, that is,

$$u_{\boldsymbol{k}}(\boldsymbol{r}+\boldsymbol{l}) = u_{\boldsymbol{k}}(\boldsymbol{r}). \tag{2.3}$$

It is necessary now to determine the function $f_{\boldsymbol{k}}(\boldsymbol{r})$. Due to the periodic potential, one requires that the quantity $|\psi_{\boldsymbol{k}}(\boldsymbol{r})|^2$, which gives the electron probability,

must be periodic. This imposes the following condition on $f_{\boldsymbol{k}}(\boldsymbol{r})$:

$$|f_{\boldsymbol{k}}(\boldsymbol{r}+\boldsymbol{l})|^2 = |f_{\boldsymbol{k}}(\boldsymbol{r})|^2. \tag{2.4}$$

The choice which satisfies this requirement for all $\boldsymbol{l}$ is the exponential form $exp(\imath \boldsymbol{k}\cdot\boldsymbol{r})$. Then it is possible to write the solution of (2.1) with periodic potential (**??**) in the form

$$\psi_{\boldsymbol{k}}(\boldsymbol{r}) = u_{\boldsymbol{k}}(\boldsymbol{r})e^{\imath \boldsymbol{k}\cdot\boldsymbol{l}}. \tag{2.5}$$

This is the Bloch function from which it is possible to establish the Bloch theorem

$$\psi_{\boldsymbol{k}}(\boldsymbol{r}+\boldsymbol{l}) = \psi_{\boldsymbol{k}}(\boldsymbol{r})e^{\imath \boldsymbol{k}\cdot\boldsymbol{l}}. \tag{2.6}$$

The Physical meaning of the Bloch theorem is that the wavefunction at positions $\boldsymbol{r}+\boldsymbol{l}$ and $\mathbf{r}$ are almost the same, except for a phase factor $exp(\imath \boldsymbol{k}\cdot\boldsymbol{l})$.

The Bloch theorem discussed above may be generalized to other cases of wave equations with periodic potentials. If there is perfect periodicity in a direct lattice, Fourier transformation gives rise to a reciprocal lattice. Now each of these states is characterized by a wavevector to which an eigenenergy or eigenfrequency is related. We shall see later that a profound consequence of periodicity is is that there are some ranges of energy or frequency, known as band-gaps, within which wave propagation is forbidden. Then the dispersion relation can be divided into separated bands. A useful concept is the Brillouin zone (BZ), i.e. the Wigner-Seitz (WS) cell of the reciprocal lattice. A Brillouin zone may be regarded as unit cell in $\mathbf{k}$ space including all the modes for propagating waves.

2.3 Study of classical waves

The propagation of classical waves, including electromagnetic waves, in media is an old scientific problem. The Bragg equation

$$2d\sin\theta_0 = n\lambda \tag{2.7}$$

which combines the wavelength λ and the lattice parameter d, is the cornerstone of the theory of diffraction in crystals.

To study the frequency-wavevector relation for electromagnetic waves in periodic structures, we at first transform the (**??**) into a stationary equation for the

electric displacement vector $\boldsymbol{D}$ as

$$-\nabla^2 \boldsymbol{D} - \nabla \times \nabla \times [\chi(\boldsymbol{r})\boldsymbol{D}] = \frac{\omega^2}{c^2}\boldsymbol{D}, \tag{2.8}$$

where

$$\chi(\boldsymbol{r}) = 1 - \frac{1}{\epsilon(\boldsymbol{r})} \tag{2.9}$$

the electric susceptibility, is also a periodic function of position.

According to the general characteristics of wave propagation in periodic structures, it is expected that electromagnetic waves can show bands and gaps as electrons do; these are known as photonic bandgaps. This is simply a window of frequencies, with finite width, in which electromagnetic wave propagation through a periodic structure cannot occur.

The crucial step in establishing propagation gaps lies in achieving a sufficiently large dielectric contrast for different media. These were first demonstrated with microwaves for three dimensional dielectric structure which are called photonic crystals by Yablonovitch in 1989 and have been pursued in the late 1990s to light waves, which are crucial for application to photonics. The photonic crystals with photonic band gaps are therefore the natural analog for semiconductors with electronic energy gaps for solid state electronics.

In the 1980s and 1990s, there was renewed interest in the study of the propagation of classical waves in both periodic and aperiodic structures. It should be noted that the study of electronic wave started from band structure (Bloch, 1928) and then led to localization (Anderson 1958, Edwards 1958); however, the study of classical waves shows a reverse process, i.e., from localization (John 1984, Anderson 1985) to band structure (Yablonovitch 1987; John 1987). Yablonovitch and John studied the propagation of electromagnetic waves in a fcc structure by different methods. The former considered "inhibited spontaneous emission in solid-state physics and electronics"; while the latter investigated the band-tail states, mobility edges and Anderson localization by introducing a known degree of disorder.

We should point out here that although electrons and photons both have characteristics of waves, there are some basic differences which influence their band structure. As a matter of fact, the underline dispersion relation for electrons is parabolic, while for photons it is linear; the angular momentum of electrons is 1/2, so scalar wave treatment is always sufficient, while photons have spin 1, and

vector-wave character plays a major role. In addition, the band theory of electrons is only an approximation due to the fact that there are always interactions among electrons, while photonic band theory is exact since interactions between photons are negligible. Thus the structure-property relationship for photonic crystals is essential independent of length scale.

2.4 Electrons in crystals

There are large numbers of electrons moving in a solid. If the interaction between electrons can be ignored, we arrive at the independent electron model, in which only the periodic ionic potential is felt by electrons.

2.4.1 Free electron gas model

If the potential is weak enough, we might take V($\mathbf{r}$)=0, then (2.1) has the plane wave solution

$$\psi_{\boldsymbol{k}}(\mathbf{r}) = \Omega^{-\frac{1}{2}} e^{\imath \boldsymbol{k}\cdot\boldsymbol{r}} \tag{2.10}$$

where Ω is the volume of the crystal. The dispersion relation now takes the simplest form

$$E(\boldsymbol{k}) = \frac{\hbar^2 k^2}{2m} \tag{2.11}$$

For a system with N electrons characterized by wavevectors $\boldsymbol{k}$, we can introduce the concept of the Fermi surface, which is the surface in $\boldsymbol{k}$ space within the which all the states are occupied. We can define the Fermi energy at the Fermi surface

$$E_F = E(\boldsymbol{k}_F) \tag{2.12}$$

where k_F is the Fermi wave vector. It is strictly valid only at $T = 0$ K but the effect of finite temperature on the Fermi surface is very small. It remain sharp even at room temperature. It is easy to find the Fermi wavevector and Fermi energy in free electron approximation by writing

$$N = \sum_{\boldsymbol{k}} = \frac{2\Omega}{(2\pi)^3} \int d\boldsymbol{k}, \tag{2.13}$$

where the factor two comes from the spin degeneracy. Noting that $\int d\boldsymbol{k} = 4\pi k_F^3/3$,

we get

$$k_F = \left(3\pi^2 \frac{N}{\Omega}\right)^{1/3} \tag{2.14}$$

and

$$E_F = \frac{\hbar}{2m}\left(3\pi^2 \frac{N}{\Omega}\right)^{2/3} \tag{2.15}$$

Equation (2.11) tells us that the electron energy depends on the wavevector $\mathbf{k}$. In fact, as periodicity exists, any state can be characterized by its reduced wavevector. Taking the empty lattice approach, fig(2.1) shows the energy as the function of the wavevector for the one dimensional free electron gas.

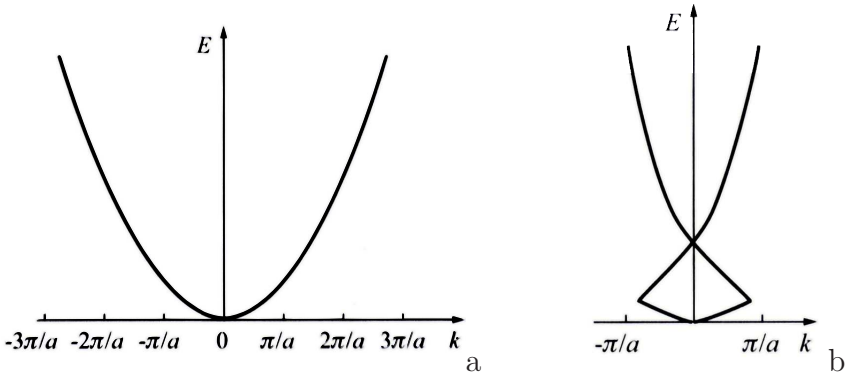

Figure 2.1: *Dispersion curve of one-dimensional free electron gas for (a) the extended zone scheme and the reduced zone (b).*

2.4.2 Nearly-free electron model

Strictly speaking, the crystal potential $V(\mathbf{r})$ cannot be ignored. However, it may be assumed that is relatively weak and can be treated as a perturbation, so it is possible to replace the free electron gas model by the nearly-free electron model. The starting point, for this model are the wavefunctions $\psi^{(0)}_{n\mathbf{k}}$ and the eigenenergies $E^{(0)}_n(\mathbf{k})$ for the free electron model. By using the perturbation theory, the dispersion relation and wavefunction can be obtained:

$$E_n(\mathbf{k}) = E^{(0)}_n(\mathbf{k}) + \langle\psi^{(0)}_{n\mathbf{k}}|V|\psi^{(0)}_{n\mathbf{k}}\rangle + \sum_{n'\mathbf{k}'}{}' \frac{|\langle\psi^{(0)}_{n'\mathbf{k}'}|V|\psi^{(0)}_{n\mathbf{k}}\rangle|^2}{E^{(0)}_n(\mathbf{k}) - E^{(0)}_{n'}(\mathbf{k}')}, \tag{2.16}$$

and

$$\psi_{n\mathbf{k}} = \psi^{(0)}_{n\mathbf{k}} + \sum_{n'\mathbf{k}'}{}' \frac{\langle \psi^{(0)}_{n'\mathbf{k}'} | V | \psi^{(0)}_{n\mathbf{k}} \rangle}{E^{(0)}_n(\mathbf{k}) - E^{(0)}_{n'}(\mathbf{k}')} \psi^{(0)}_{n'\mathbf{k}'}. \tag{2.17}$$

For simplicity and still without loss of generality, we take the one-dimensional case as an example. In (2.16), the second term on the right hand side is a constant, and merely corresponds to a shift of the zero energy. When we consider the lowest energy band $n = 1$ and we only consider $n' = 2$, we obtain the following:

$$E_1(\mathbf{k}) \simeq E^{(0)}_1(k) + \frac{|V_{-2\pi/a}|^2}{E^{(0)}_1(k) - E^{(0)}_2(k)}, \tag{2.18}$$

with

$$V_{-2\pi/a} = \frac{1}{L} \int V(x) e^{\imath 2\pi x/a} dx.$$

There is only a slight modification for the eigenenergy of (2.18) from the parabolic dispersion curve of fig.2.1, if k is not at the Brillouin zone boundary. However, when $k \simeq \pi/a$, $E^{(0)}_1 = \hbar^2 k^2/2m$, $E^{(0)}_2 = \hbar^2(k - 2\pi/a)^2/2m$, then the $E^{(0)}_1 \simeq E^{(0)}_2$ and degenerate perturbation theory is needed. The result of applying this is:

$$E_{\pm}(k) = \frac{1}{2} \left\{ E^{(0)}_1(k) + E^{(0)}_2(k) \pm \left[(E^{(0)}_1(k) - E^{(0)}_2(k))^2 + 4|V_{-2\pi/a}|^2 \right]^{1/2} \right\} \tag{2.19}$$

and there is an energy gap

$$E_g = E_+ - E_- \tag{2.20}$$

at the boundary of the first Brillouin zone. The same procedure can be used to get the whole energy spectrum for the one-dimensional nearly-free electron model as shown in fig 2.2 where (a) is for the extended zone scheme and (b) for the reduced zone scheme. Thus a periodic potential brings in energy bands and gaps.

The energy gap is related to the Bragg diffraction of electron waves. We can see this by observing that the first order modified wavefunction of the first band for $-\pi/a < k < \pi/a$ is

$$\psi_{1k} = \psi^{(0)}_{1k} + \frac{V_{-2\pi/a}}{E^{(0)}_1(k) - E^{(0)}_2(k)} \psi^{(0)_{2k}}, \tag{2.21}$$

where the summation only involves the wavefunction of the second band. Here $\psi^{(0)}_{1k} = L^{-1/2} exp(\imath k x)$ represents the wave traveling in the positive direction,

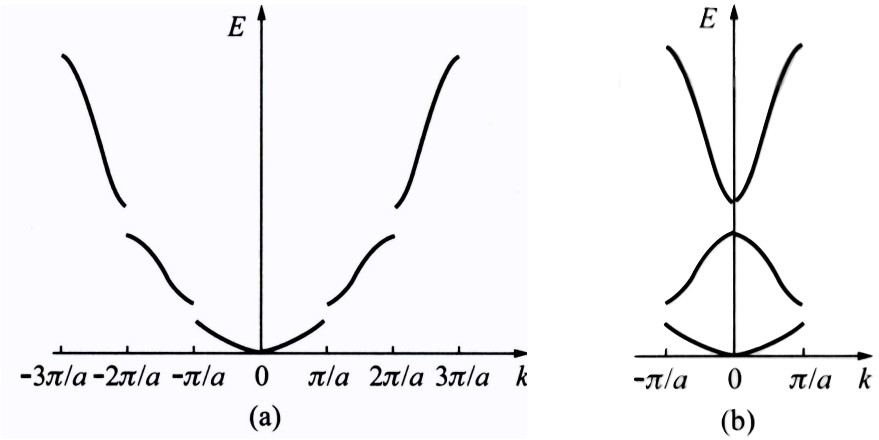

Figure 2.2: *Bands and gaps in one-dimensional nearly-free electron model for (a)the extended zone scheme, and (b) the reduced zone*

whereas $\psi_{1k}^{(0)} = L^{-1/2} exp[\imath(k - 2\pi/a)x]$ a left traveling wave. Near the zone edge, degenerate perturbation theory is still needed. The wavefunctions $\psi_{1k}^{(0)}$ and $\psi_{1k}^{(0)}$ are treated on an equal footing, then the wavefunctions at the brillouin zone boundaries are

$$\psi_{\pm}(x) = \frac{1}{\sqrt{2L}} \left[\psi_{1,\pi/a}^{(0)}(x) \pm \psi_{2,\pi/a}^{(0)}(x) \right] = \frac{1}{\sqrt{2L}} \left(e^{\imath\pi x/a} \pm e^{-\imath\pi x/a} \right). \tag{2.22}$$

These two state functions $\psi_+ (2/L)^{1/2} \cos(\pi x/a)$ and $\psi_- = (2/L)^{1/2} \sin(\pi x/a)$ represents standing waves.

Then at the edges of the Brillouin zone ($k = \pm\pi/a$) we have a standing wave ($v_g = 0$, group velocity).

The squared modulus of ψ_+ and ψ_- are electron probability distribution as shown in fig 2.3.

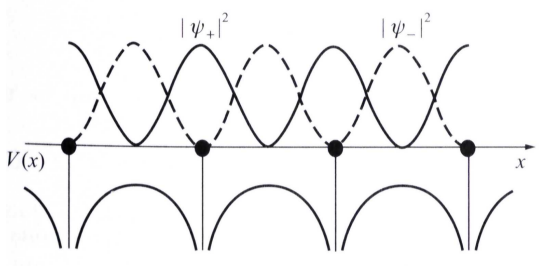

Figure 2.3: *Bragg reflection of electron in a periodic structure*

From the viewpoint of scattering, at the zone edge $k = \pi/a$, the scattering is strong and the reflected wave has the same amplitude as the incident wave. This leads to Bragg diffraction at $\lambda = 2\pi/k = 2a$. This strong scattering is caused by the periodic potential. Bragg scattering at the zone boundary opens up energy gaps, that is, the interaction of electron waves with the atomic lattice results in destructive interference at certain wavelengths.

It is clear that fig 2.1 was changed into fig 2.2, when the crystalline potential was added. The continuous energy-wavevector dispersion relation characteristic of free space is therefore modified; this energy spectrum is referred to as the electronic band structure of the system.

2.5 Electromagnetic waves in periodic structures

We now consider an electromagnetic wave propagating in a medium characterized by a spatially dependent dielectric constant $\epsilon(\mathbf{r})$. For simplicity, $\epsilon(\mathbf{r})$ is assumed to be scalar function of position. Here we are only concerned with non magnetic media, so μ is a constant, simply $\mu = 1$. We shall also assume that there is a periodic variation in the dielectric constant satisfying equation **??**.

2.5.1 Photonic bandgaps in layered periodic media

It is fundamental at this point to investigate layered periodic media, because, as we have seen in the previous chapter, photonic crystals fall in this category.

We consider a situation where there are two kinds of slabs with thicknesses d_1 and d_2 arranged alternatively with dielectric constant ϵ_1 and ϵ_2, respectively as shown in fig. 2.4(a). We assume that the stacking direction is z, and x-y plane is infinite and homogeneous. Electromagnetic wave propagation in this system can be treated as a one-dimensional problem, because it is trivial for waves along the x and y directions.

Let $\boldsymbol{E} = \boldsymbol{e}\mathcal{E}$, where $\boldsymbol{e}$ is the unit vector, then wave equation 2.8 can be reduced to

$$\frac{d^2}{dz^2}\mathcal{E}(z) + \frac{\omega^2}{c^2}\epsilon(z)\mathcal{E}(z) = 0. \tag{2.23}$$

The unit cell is composed of slab 1 and slab 2, so that the lattice spacing is $d = d_1 + d_2$. Then the periodicity of the dielctric constant can be written as

$$\epsilon(z + d) = \epsilon(z), \tag{2.24}$$

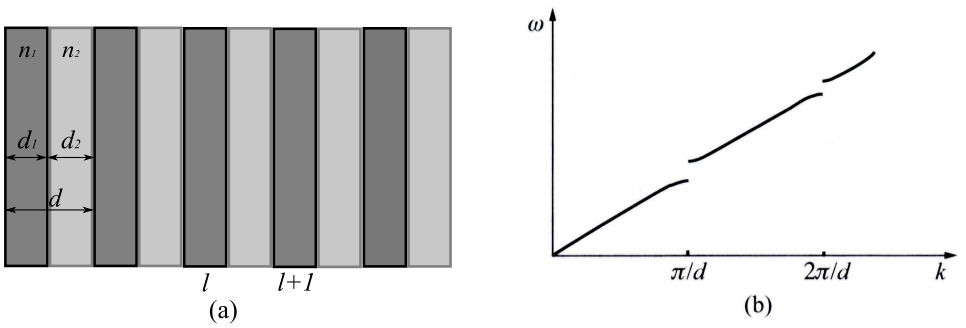

Figure 2.4: *(a)Layered periodic medium composed with two kind of slabs with thicknesses d_1 and d_2; (b)dispersion relation for a one-dimensional periodic dielectric structure.*

which will lead the solution of (2.23) to have the Bloch form

$$\mathcal{E}(z+d) = \mathcal{E}(z)e^{\imath kd}. \tag{2.25}$$

Further, we write the solutions in slab 1 and slab 2 of the lth unit cell and the slab 1 of the $(l+1)$th unit cell as follows:

$$\begin{aligned}
\mathcal{E}_l^{(1)}(z) &= A_l e^{\imath q_1 z} + B_l e^{-\imath q_1 z}, \\
\mathcal{E}_l^{(2)}(z) &= C_l e^{\imath q_2 z} + D_l e^{-\imath q_2 z}, \\
\mathcal{E}_{l+1}^{(1)}(z) &= A_{l+1} e^{\imath q_1 z} + B_{l+1} e^{-\imath q_1 z},
\end{aligned} \tag{2.26}$$

where we define $q_1 = \sqrt{\epsilon_1}\omega/c = n_1\omega/c$, $q_2 = \sqrt{\epsilon_2}\omega/c = n_2\omega/c$, with n_1 and n_2 the indices of refraction. A_l, B_l, C_l and D_l are the oscillation amplitudes of the electric field.

For convenience, we take the interface at the left hand side of each slab as its local coordinate origin $z = 0$, then using the continuity conditions of ε and $d\varepsilon/dz$ at boundaries, we can find that

$$\begin{pmatrix} A_{l+1} \\ B_{l+1} \end{pmatrix} = \boldsymbol{T} \begin{pmatrix} A_l \\ B_l \end{pmatrix}, \tag{2.27}$$

where $\boldsymbol{T}$ is a 2×2 transfer matrix with elements

$$\begin{aligned} T_{11} &= e^{\imath q_1 d_1}\left[\cos(q_2 d_2) + \frac{\imath}{2}\left(\frac{n_1}{n_2} + \frac{n_2}{n_1}\right)\sin(q_2 d_2)\right], \\ T_{12} &= e^{\imath q_1 d_1}\frac{\imath}{2}\left(\frac{n_1}{n_2} - \frac{n_2}{n_1}\right)\sin(q_2 d_2), \\ T_{21} &= T_{12}^*, \\ T_{22} &= T_{11}^*. \end{aligned} \tag{2.28}$$

Thus (2.25) is transformed into

$$\begin{pmatrix} A_{l+1} \\ B_{l+1} \end{pmatrix} = e^{\imath k d}\begin{pmatrix} A_l \\ B_l \end{pmatrix}. \tag{2.29}$$

Substituting this in (2.27), we have

$$(\boldsymbol{T} - e^{\imath k d} I)\begin{pmatrix} A_l \\ B_l \end{pmatrix} = 0, \tag{2.30}$$

where I is the unit matrix. If we consider the reverse process to get A_{l-1}, B_{l-1} from A_l, B_l, we can obtain

$$(\boldsymbol{T})^{-1} - e^{-\imath k d} I = \begin{pmatrix} A_l \\ B_l \end{pmatrix}. \tag{2.31}$$

Combining these two expressions, we obtain

$$\cos kd = \frac{1}{2}(\boldsymbol{T} + \boldsymbol{T}^{-1}) = \frac{1}{2} Tr\, \boldsymbol{T}. \tag{2.32}$$

Finally, we have the transcendental equation

$$\cos k(d_1+d_2) = \cos\frac{n_1\omega d_1}{c}\cos\frac{n_2\omega d_2}{c} - \frac{1}{2}\left(\frac{n_1}{n_2} + \frac{n_2}{n_1}\right)\sin\frac{n_1\omega d_1}{c}\sin\frac{n_2\omega d_2}{c}, \tag{2.33}$$

from which the dispersion relation for electromagnetic wave propagation in the one dimensional periodic dielectric structure is determined. The numerical result is shown in fig 2.4(b). It is clear that there are pass-bands and stop-bands for certain frequencies ω. The stop bands appear at the boundaries of the Brillouin zones. So there is a forbidden range of wavelengths that can not propagate within the layered medium.

2.5.2 Waves propagation along the cholesteric helical axis

Let us now give a look to the propagation of electromagnetic waves in the cholestric structure, and more precisely along the cholesteric helical axis. The presence of a stop band is to be found also in this case.

The starting point is an assumption on the form of the local dielectric tensor $\varepsilon(\mathbf{r})$ at any point $\mathbf{r}$ in the cholesteric fluid: neglecting the weak intrinsic rotation that persists in the isotropic phase, we may write that the electric displacement $\mathbf{D(r)}$ is a linear functional of the electric field $\mathbf{E(r)}$, taken at the same point $\mathbf{r}$,

$$\begin{aligned} &\mathbf{D} = \varepsilon\mathbf{E} = \epsilon_\perp \mathbf{E} + \epsilon_a \mathbf{n}(\mathbf{n}\cdot\mathbf{E}), \\ &\epsilon_a = \epsilon_\perp - \epsilon_\parallel . \end{aligned} \tag{2.34}$$

For a wave propagation along the helical axis z, $\mathbf{D}$ and $\mathbf{E}$ are restricted to the x,y-plane and eqn.(2.34), involving two parameters ($\epsilon_\parallel$ and $\epsilon_\perp$), is the most general form. Let now consider specifically the propagation, along z, of an electromagnetic wave of frequency ω. The non-zero components are

$$\begin{aligned} E_x(z,t) &= Re\{E_x(z)e^{-\imath\omega t}\}, \\ E_y(z,t) &= Re\{E_y(z)e^{-\imath\omega t}\} \end{aligned} \tag{2.35}$$

(Re = real part of), if we use Maxwell equations we obtain

$$-\frac{d^2}{dz^2}\begin{pmatrix} E_x \\ E_y \end{pmatrix} = \left(\frac{\omega}{c}\right)^2 \hat{\epsilon}(z) \begin{pmatrix} E_z \\ E_y \end{pmatrix}. \tag{2.36}$$

The explicit form of the matrix $\hat{\epsilon}$ is

$$\hat{\epsilon} = \frac{\epsilon_\parallel + \epsilon_\perp}{2}\begin{bmatrix} 1 & 0 \\ 0 & 1 \end{bmatrix} + \frac{\epsilon_a}{2}\begin{bmatrix} \cos 2q_0 z & \sin 2q_0 z \\ \sin 2q_0 z & -\cos 2q_0 z \end{bmatrix}. \tag{2.37}$$

Equation (2.36) does not have exactly the structure of an eigenvalue problem. However, there are some simple features. The operators on both sides are unchanged by translations of length L along (z). This implies a Bloch-Floquet theorem; a complete set of solutions can be found, such that, for each of them

$$\begin{pmatrix} E_x \\ E_y \end{pmatrix}_{z+L} = const \times \begin{pmatrix} E_x \\ E_y \end{pmatrix}_z . \tag{2.38}$$

Here we shall find it convenient to write the constant in the form $-e^{\imath lL}$ (the minus

sign is chosen because the helical pitch is $P = 2L$). The wavevector l defines the mode under consideration; note that l may be real (propagating wave) or complex (evanescent wave).

Dispersion relation

To derive the solution explicitly it is convenient to analyse all fields in terms of circular (rather than linear) waves. This amounts to choosing as new variables the quantities

$$E = E_x \pm \imath E_y. \tag{2.39}$$

Equation (2.36) then becomes

$$\begin{aligned} -\frac{d^2E^+}{dz^2} &= k_0^2 E^+ + k_1^2 \exp(2\imath q_0 z) E^-, \\ -\frac{d^2E^+}{dz^2} &= k_1^2 \exp(-2\imath q_0 z) E^+ + k_0^2 E^- \end{aligned} \tag{2.40}$$

where we have put

$$\begin{aligned} k_0^2 &= \left(\frac{\omega}{c}\right)^2 \frac{\epsilon_\parallel + \epsilon_\perp}{2} \\ k_1^2 &= \left(\frac{\omega}{c}\right)^2 \frac{\epsilon_a}{2}. \end{aligned} \tag{2.41}$$

From equation(2.40) we can immediately find the form of the modes

$$\begin{aligned} E^+ &= a \exp\{\imath(l + q_0)z\}, \\ E^- &= b \exp\{\imath(l - q_0)z\} \end{aligned} \tag{2.42}$$

where a and b are two constants, linked by the relations

$$\begin{aligned} \{(l + q_0)^2 - k_0^2\}a - k_1^2 b &= 0, \\ -k_1^2 a + \{(l - q_0)^2 - k_0^2\}b &= 0. \end{aligned} \tag{2.43}$$

The two equations (2.43) have a non-trivial solution only if the corresponding determinant vanishes

$$(-k_0^2 + l^2 + q_0^2)^2 - 4q_0^2 l^2 - k_1^4 = 0. \tag{2.44}$$

For a given frequency ω, k_0 and k_1 are fixed and eqn.(2.44) gives four possible values of l (real or complex). The relation between ω and l for real l is called the *dispersion relation*; it is shown in fig 2.5. There are two distinct branches, which

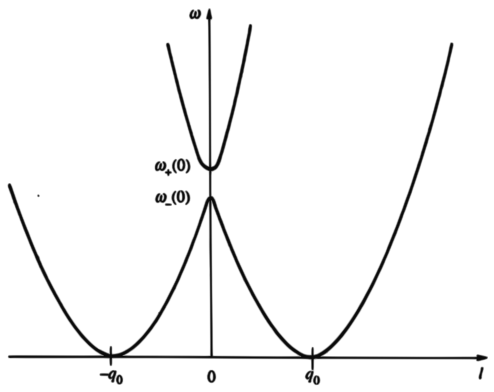

Figure 2.5: *Relation between frequency and vector l for propagation of electromagnetic modes in a cholesteric spiral.*

we call (+) and (-). To locate them, it is useful to consider first the case $l = 0$. This gives

$$k_0^2 - q_0^2 = \pm k_1^2. \tag{2.45}$$

Returning to the definitions of k_0 and k_1 (eqn. 2.41) one obtains the frequencies

$$\begin{aligned} \omega_+(0) &= \frac{cq_0}{n_o} \qquad n_o = \sqrt{\epsilon_\perp} = \text{ordinary index} \\ \omega_-(0) &= \frac{cq_0}{n_e} \qquad n_e = \sqrt{\epsilon_\parallel} = \text{extraordinary index} \end{aligned} \tag{2.46}$$

$\omega_+(0)$ corresponds to $a = -b$. From eqn(2.42) this describes a linear wave polarized along the direction $\theta(z) + \frac{1}{2}z$ (ordinary axis). Similarly, $\omega_-(0)$ corresponds to $a = b$, i.e. a linear wave polarized along the local extraordinary axis.

The interval $\omega_-(0) < \omega < \omega_+(0)$ will be called the frequency gap.

Bragg reflection

Let us choose a frequency ω inside the gap

$$\frac{cq_0}{n_e} < \omega < \frac{cq_0}{n_o}. \tag{2.47}$$

For such a case, we see from fig 6.5 that eqn (2.44) has only two real roots ($l = \pm l_1$). The other two roots are pure imaginary $l = \pm \imath\kappa$.

Consider now a thick slab ($d \to \infty$) attached from below, at normal incidence , by a light beam of polarization $\mathbf{i}(i_x, i_y)$. This will in general induce the slab two waves:

1. One travelling wave [amplitude proportional to $\exp(il_1 z)$].

2. One evanescent wave [amplitude $\sim \exp(-\kappa z)$].

By a suitable choice of the polarization $\mathbf{i}$,($\mathbf{i} = \mathbf{i}_R$) it is possible to extinguish the traveling wave component: this means that a beam of polarization $\mathbf{i}_R$ will be totally reflected. We conclude that the gap $[\omega_-(0), \omega_+(0)]$ corresponds to the frequency range for possible Bragg reflections.

2.6 The density of states

The concept of the density of states arises in many branches of physics. Here we focus on the photon density of states, which is important for the discussion of black-body radiation, for the emission properties of atoms and the laser effect. In this section we also explain how the derivation of the density of states can be adapted also for massive particles.

Consider the electromagnetic field within a finite volume V of free space as shown in the figure(2.6). For simplicity, we assume that the volume comprise a cube of edge length L, so that $V = L^3$. The volume is assumed to be large enough so that its dimension have no significant effect on the physical result. It then serves just as a computational tool that allow us to find the density of states in an easy way.

The general solution for the electromagnetic field within V can be written as a superposition of traveling waves of the form:

$$\mathcal{E}(\boldsymbol{r}, t) = \sum_{\boldsymbol{k}} \mathcal{E}_k e^{\imath(\boldsymbol{k}\cdot\boldsymbol{r} - \omega t)}, \tag{2.48}$$

with $\omega = c|\mathbf{k}|$ the first Maxwell equation, in the free space reduces to $\nabla \cdot \mathcal{E} = 0$ which is satisfied if:

$$\mathbf{k} \cdot \mathcal{E}_k = 0 \tag{2.49}$$

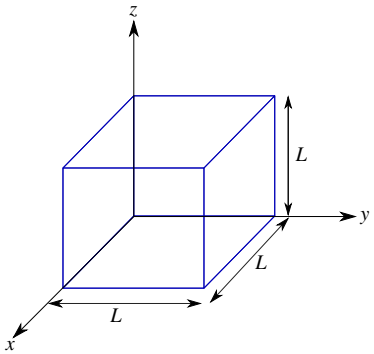

Figure 2.6: *Finite volume of free space considered for calculating the electromagnetic density of states*

and implies that the waves must be transverse: that is, $\mathcal{E}_k \perp \mathbf{k}$. This transverse condition allows for two independent wave polarizations for each value of $\mathbf{k}$.

Equation (2.48) gives us a general expression for the field within volume V. The expansion functions are sine waves, and the expression can therefore be thought as a Fourier series. Since we are dealing with a finite volume, we can write:

$$\mathcal{E}(\mathbf{r},t) = \sum_{k_x,k_y,k_z} \mathcal{E}_{\boldsymbol{k}} e^{\imath k_x x} e^{\imath k_y y} e^{\imath k_z z} e^{-\imath\omega t}. \tag{2.50}$$

the value of k_x, k_y and k_z are determined by the dimension of V, with:

$$\begin{aligned} k_x L &= 2\pi n_x \\ k_y L &= 2\pi n_y \\ k_z L &= 2\pi n_z \end{aligned} \tag{2.51}$$

where n_x, n_y and n_z are all integers. The possible value of the wave vector can therefore be written in the form:

$$\boldsymbol{k} \equiv (k_x, k_y, k_z) = \frac{2\pi}{L}(n_x, n_y, n_z). \tag{2.52}$$

Each set of integers (n_x, n_y, n_z) corresponds to two modes of the electromagnetic field: one for each polarization.

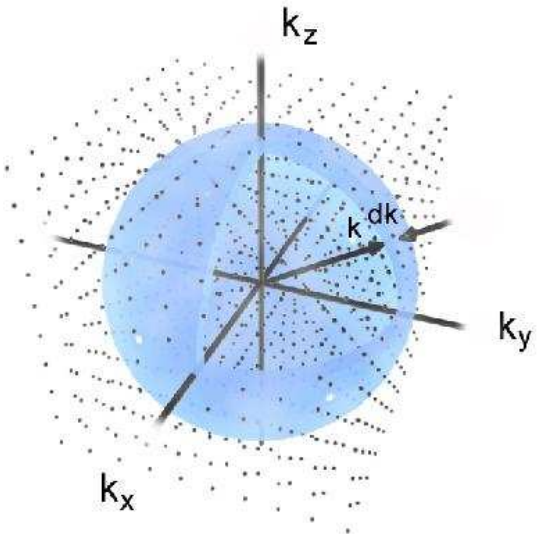

Figure 2.7: *Visualization of k-space showing values of k as points the number of allowed states is the number of these points contained in the shell of radius k and thickness dk.*

Figure 2.7 shows a plot of the allowed values of the wavevector in the space. The allowed values form a grid with a spacing of $2\pi/L$ between successive points.

Thus each allowed value of the $\boldsymbol{k}$-vector in the plane occupies an effective area of $(2\pi/L)^2$ of the two dimensional slice $\boldsymbol{k}$-space. In a more general way we can say that each $\boldsymbol{k}$-state will occupy an effective volume of $(2\pi/L)^3$ of the $\boldsymbol{k}$-space.

Now we want to know how many allowed $\boldsymbol{k}$-states there are with their magnitudes between k and $k+dk$. We write this number as $g(k)dk$. In three dimensions this number is obtained by dividing the volume of $\boldsymbol{k}$-space enclosed between spherical shells of radius k and $k+dk$ by the effective volume per $\boldsymbol{k}$-state, namely $(2\pi/L)^3$:

$$g^{3D}(k)dk = \frac{4\pi k^2 dk}{(2\pi/L)^3} = L^3 \frac{k^2}{2\pi^2} dk = V \frac{k^2}{2\pi^2} dk. \tag{2.53}$$

We then normalize by V to obtain:

$$g(k) \equiv \frac{g^{3D}(k)}{V} = \frac{k^2}{2\pi^2}. \tag{2.54}$$

Note that this value does not depend on the volume and confirm that the subdivision of space is merely a computational tool.

Having worked out the state density in the $\boldsymbol{k}$-space, we can now work out the number of states per unit volume per unit angular frequency range $g(\omega)$. To do this we map the values of k and $k+dk$ onto their corresponding angular frequencies, namely ω and $\omega + d\omega$, and remember that there are two photon polarizations for each $\boldsymbol{k}$-state. We thus write:

$$g(\omega)d\omega = 2 \times g(k)dk, \tag{2.55}$$

implying

$$g(\omega) = \frac{2g(k)}{d\omega/dk}. \tag{2.56}$$

We recall that $v_g = d\omega/dk$ and that at the edges of the Brillouin zone v_g approaches to zero (2.22), then at $k = \pm\pi/a$ $g(\omega)$ dramatically increases.

With $\omega = ck$ we finally obtain

$$g(\omega) = \frac{\omega^2}{\pi^2 c^3}. \tag{2.57}$$

This shows that the photon density of states is proportional to the square of the frequency.

The derivation of the density of states for photon modes can be adapted to other branches of physics. In the case of electron waves in crystals, we usually

require $g(E)$, the density of states per unit volume per unit energy range. We first work out the density of states in momentum space. The derivation is identical to that given above, with $g(k)$ given by eqn.(2.54). In analogy with eqn.(2.57), we then write:

$$g(E) = 2 \times \frac{g(k)}{dE/dk} \tag{2.58}$$

In this case, the factor of two comes from the fact that there are two electron spin states for each available $\boldsymbol{k}$-states, namely spin-up and spin-down. For free electrons we have:

$$E = \frac{\hbar^2 k^2}{2m_0}, \tag{2.59}$$

which then gives:

$$g(E) = \frac{1}{2\pi^2}\left(\frac{2m_0}{\hbar^2}\right)^{3/2} E^{1/2}. \tag{2.60}$$

For the one-dimensional case we can write:

$$g(E) = \frac{1}{2}\left(\frac{2m}{\pi^2\hbar^2}\right)^{1/2} E^{1/2} \tag{2.61}$$

Chapter 3

Radiative transition and Laser

In the previous chapter we have described how a photonic stop band arises in periodic media. In this chapter we will give an overview of the theory of optical absorption and emission in atoms and in molecules, which forms the basis concepts for our understanding of classical laser mechanisms. Next we will describe how can be possible, combining the presence of a stop band with the fluorescence properties of some molecules, to achieve mirror-less lasing from dye doped cholesteric liquid crystals.

3.1 Radiative transitions (of atoms)

The treatment of the interaction between light and atoms was pivotal in the development of quantum theory in the first half of the twentieth century. In 1913 Bohr postulated that a quantum of light of angular frequency ω is absorbed or emitted whenever an atom jumps between two quantized energy levels E_1 and E_2 that satisfy:

$$E_2 - E_1 = \hbar\omega, \tag{3.1}$$

where E_2 is the energy of the upper level and E_1 is the energy of the lower level. The theory was developed by Einstein in 1916-17 when he introduced the **Einstein coefficient** to quantify the rate at which the absorption and emission of quanta occur. In the same paper he discovered the process of stimulated emission, which later proved to be the basis of laser operation.

3.1.1 Einstein coefficient

The quantum theory of radiation assumes that light is emitted or absorbed whenever an atom (or a molecule) makes a jump between two quantum states. These two processes are illustrated in fig 3.1.

Absorption occurs when the atom jumps to a higher level, while emission corresponds to the process in which a photon is emitted as the atom drops down to a lower level. Conservation of energy requires that the angular frequency ω of the photon satisfies 3.1. In the next section we explain how quantum mechanics enables us to calculate the emission and absorption rates. At this stage we restrict ourselves to phenomenological analysis based on the **Einstein coefficient** for the transition.

The radiative process by which an electron in an upper level drops to a lower level as shown in fig 3.1(a) is called **spontaneous emission**. This is because the atoms in the excited state have a natural (i.e. spontaneous) tendency to de-excite and lose their excess energy. Each type of atom has a characteristic spontaneous-emission spectrum determined by its energy according to equation (3.1).

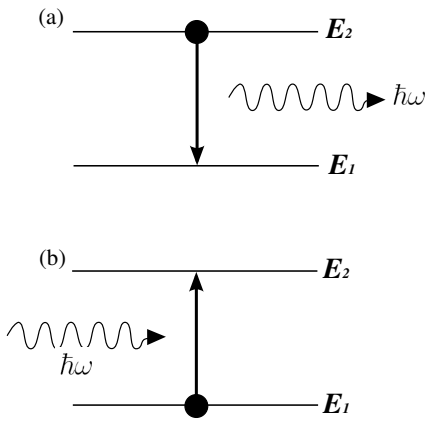

Figure 3.1: *Optical transitions between two states in an atom: (a)spontaneous emission, (b) absorption*

The rate at which spontaneous emission occurs is governed by the Einstein A coefficient for the transition. This gives the probability per unit time that the electron in the upper level will drop to the lower level by emitting a photon. The photon emission rate is therefore proportional to the number of atoms in the excited state and to the A coefficient for the transition. We thus write down the following rate equation for $N_2(t)$, the number of atoms in the excited state:

$$\frac{dN_2}{dt} = -A_{21}N_2. \tag{3.2}$$

The subscript "21" on the A coefficient in the eqn.(3.2) makes it plane that the transition starts at level 2 and ends at level 1.

Equation 3.2 can be solved for $N_2(t)$ to give:

$$N_2(t) = N_2(0)\exp(-A_{21}t) \equiv N_2(0)\exp(-t/\tau), \tag{3.3}$$

where

$$\tau = \frac{1}{A_{21}}. \tag{3.4}$$

τ is the **radiative lifetime** of the excited state. Equation 3.3 shows that the number of atoms in the excited state decays exponentially with a time constant τ due to the spontaneous emission. The value of τ for a transition at optical frequencies can range from about a nanosecond to several milliseconds, according to the type of radiative process that occurs.

The process of **absorption** is illustrated in fig 3.1(b). The atom is promoted from the lower level to the excited state by absorbing the required energy from a photon. Unlike emission, it is not a spontaneous process. The electron cannot jump to the excited state unless it receives the required energy from an incoming photon. Following Einstein's treatment, we write the rate of absorption transition per unit time as:

$$\frac{dN_1}{dt} = -B_{12}^{\omega} N_1 u(\omega), \tag{3.5}$$

where $N_1(t)$ is the number of atoms in level 1 at time t, B_{12}^{ω} is the Einstein B coefficient for the transition, and $u(\omega)$ is the spectral energy density of the electromagnetic field in $Jm^{-3}(rad/s)^{-1}$ at angular frequency ω. By writing $u(\omega)$ we are explicitly stating that only the part of the spectrum of the incoming radiation at angular frequency around ω, where $\hbar\omega = E_2 - E_1$, can induce the absorption transitions. Equation 3.5 may be considered to be the definition of the Einstein B coefficient.

The process of absorption and spontaneous emission that we have described are fairly intuitive. Einstein realized that the analysis was not complete, and introduced a third type of transition called **stimulated emission**. In this process, the incoming photon field can stimulate downward emission transition as well as absorption transition. The stimulated-emission rate is governed by a second Einstein B coefficient, namely B_{21}. The subscript is now essential to distinguish the B coefficients for the two different processes of absorption and stimulated emission.

In analogy with equation 3.5, we write the rate of stimulated emission transition by the following rate equation:

$$\frac{dN_2}{dt} = -B_{21}^{\omega} N_2 u(\omega). \tag{3.6}$$

Stimulated emission is a coherent quantum mechanical effect in which the photons

emitted are in phase with the photons that induce the transition.

Following the Einstein's analysis we can imagine to have a gas of N atoms inside a box with black walls at temperature T. We assume that the atoms only interact with the black body radiation filling the cavity and not directly with each other. The black-body radiation will induce both absorbtion and stimulated emission transitions, while spontaneous-emission transition will also be occurring at a rate determined by the Einstein A coefficient. The three types of transition are indicated in fig. 3.2. If we leave the atoms for long enough, they will come

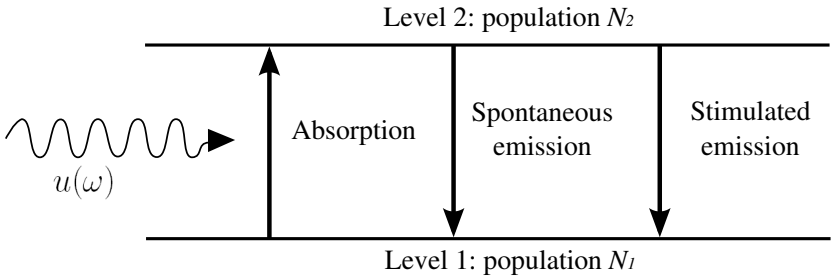

Figure 3.2: *Absorption, spontaneous emission and stimulated emission transitions between two levels of an atom in the presence of electromagnetic radiation with spectral energy density* $u(\omega)$.

to thermal equilibrium with the black-body radiation. In this steady-state conditions, the rate of upward transitions due to absorption must exactly balance the rate of downward transitions due to spontaneous and stimulated emission. From equations 3.2-3.6 we must therefore have:

$$B_{12}^{\omega} N_1 u(\omega) = A_{21} N_2 + B_{21}^{\omega} N_2 u(\omega). \tag{3.7}$$

Since the atoms are in thermal equilibrium with the radiation field at temperature T, the distribution of the atoms among the various energy levels will be governed by the law of thermal physics. The ratio of N_2 to N_1 will therefore be given by Boltzmann's law:

$$\frac{N_2}{N_1} = \frac{g_2}{g_1} \exp\left(-\frac{\hbar\omega}{k_B T} \right), \tag{3.8}$$

where g_1 and g_2 are the degeneracies of levels 1 and 2, respectively. Now the energy spectrum of the black-body source is given by the Planck formula:

$$u(\omega) = \frac{\hbar\omega^3}{\pi^2 c^3} \frac{1}{\exp(\hbar\omega/k_B T) - 1}. \tag{3.9}$$

The only way that eqns. 3.7-3.9 can be consistent with each other at all temperatures is if:

$$g_1 B_{12}^{\omega} = g_2 B_{21}^{\omega}, \tag{3.10}$$

and

$$A_{21} = \frac{\hbar\omega^3}{\pi^2 c^3} B_{21}^{\omega}. \tag{3.11}$$

Equation 3.10 tells us that the probability for stimulated absorption and emission are the same apart from the degeneracy factors. Furthermore, the interrelationship of the Einstein coefficients tells us that transitions that have a high absorption probability will also have high emission probability, both for spontaneous process and stimulated ones.

3.1.2 Radiative transition rates

The calculation of radiative transition rates by quantum mechanics is based on time-dependent quantum theory. The light matter interaction is described by transition probabilities, which can be calculated for the case of spontaneous emission by using **Fermi's golden rule**. According to this rule, the transition rate is given by:

$$W_{1\to 2} = \frac{2\pi}{\hbar} |M_{12}|^2 g(\hbar\omega), \tag{3.12}$$

where M_{12} is the **matrix element** for the transition, and $g(\hbar\omega)$ is the **density of states**.

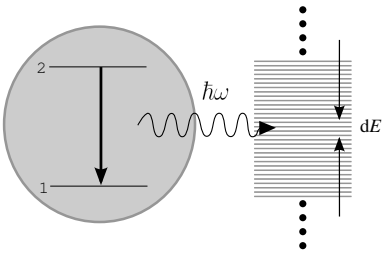

Figure 3.3: *Optical transitions between atomic states involving photon emission into a continuum of states*

Let us first consider the density of states factor that appears in the golden rule. The density of states is defined so that $g(\hbar\omega)dE$ is the number of final states per unit volume that falls within the energy range E to $E + dE$, where $E = \hbar\omega$. In the standard case of transitions between quantized levels in an atom, the initial and final electron states are *discrete*. In this case, the density of final states factor that enters equation 3.12 is the density of photon states.

In considering spontaneous radiative emission by an atom, we shall usually be interested in the situation where the photons are emitted in the free space. In this case, the photons are emitted into a continuum of states as illustrated schematically in fig.3.3

The density of photon modes is proportional to ω^2 in free space, as we a have seen previously (eqn. 2.57). This factor of ω^2, together with a third factor of ω to account for the photon energy, normally appears in the spontaneous-emission probability. Note, however, that the photon density of states can be modified by making the atoms emit into an optical cavity or into a photonic crystal. This modification of the photon density of states can have a profound effect on the radiative emission rate, as we shall consider later in this chapter.

3.2 Radiative transition (of molecules)

Once a molecule is excited by absorbtion of a photon, as we have already seen for atoms, it can return to the ground state with emission of light but many other pathways are also possible (fig. 3.4): internal conversion (i.e. direct return to the ground state without emission of light), intersystem crossing, itermolecular charge transfer and conformational change. Interactions in the excited state with other molecules may also compete with de-excitation: electron transfer, proton transfer, energy transfer, excimer and exciplex formation.

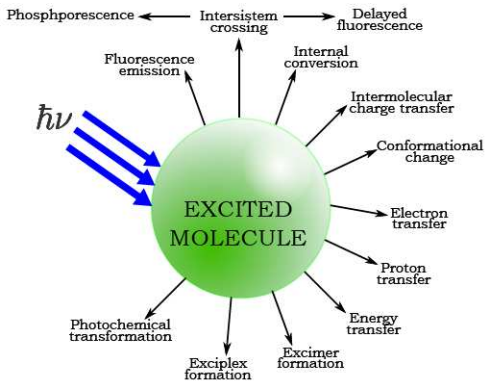

Figure 3.4: *Possible de-excitation pathways of excited molecules*

In this section we will see more in dept the radiative transition like luminescence effects. Luminescence is the emission of light from any substance and occurs from electronically excited states. Luminescence is formally divided into two categories, fluorescence and phosphorescence, depending on the nature of the excited state. In the excited singlet states, the electron in the excited orbital is paired (of opposite spin) to the second electron in the ground-state orbital. Consequently, return to the ground state is spin allowed and occurs rapidly by emission of a photon. The emission rates of fluorescence are typically $10^8 s^{-1}$ so that a typical fluorescence lifetime is near 10 ns. The lifetime (τ) of a fluorophore is the average time between its return to the ground state.

Phosphorescence is emission of light from triplet excited states, in which the electron in the excited orbital has the same spin orientation as the ground state electron. Transitions to the ground state are forbidden and the emission rates are

slow ($10^3 - 10^0 s^{-1}$), so that phosphorescence lifetime are typically milliseconds to seconds.

Fluorescence typically occurs from aromatic molecules. some typical fluorescent substances are shown in figure 3.6. Fluorescence spectral data are generally

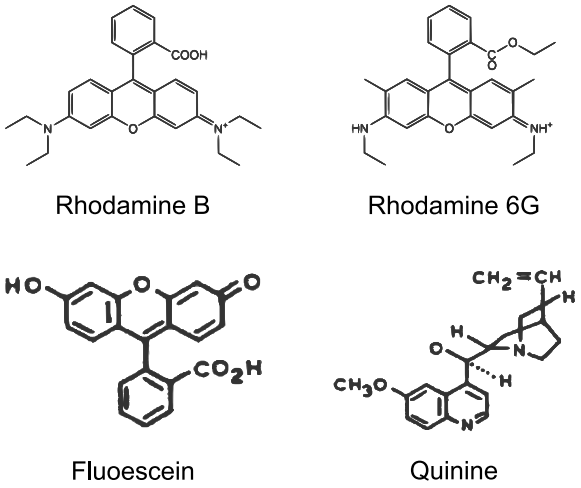

Figure 3.5: *Examples of fluorescent molecules*

presented as emission spectra. A fluorescence emission spectrum is a plot of the fluorescence intensity versus wavelength (*nanometers*). Emission spectra vary

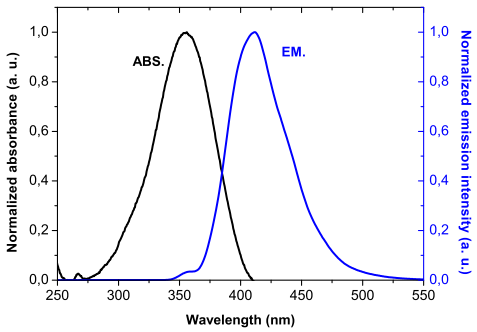

Figure 3.6: *Example of absorbtion and emission spectra.*

widely and are dependent upon the chemical structure of the fluorophore and the solvent in which it is dissolved. The spectra of some compounds, as it is possible to observe in the following figure 3.7, show significant structure due to the individual vibrational energy levels of the ground and the excited states.

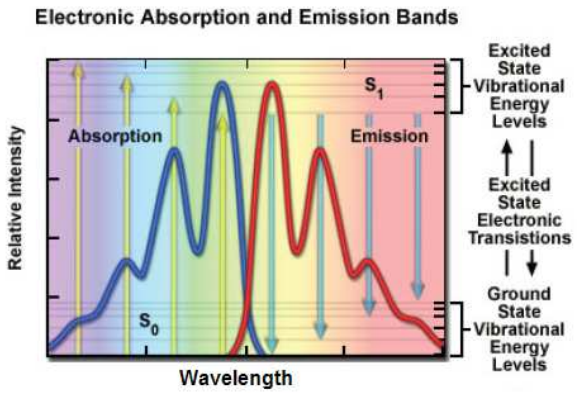

Figure 3.7: *Sketched spectra, showing the presence of several peaks corresponding to the transition between vibrational excited energy levels and ground state vibrational energy levels.*

3.2.1 Jablonski diagram

The processes which occur between the absorbtion and the emission of light are usually illustrated by a Jablonski diagram. Jablonski diagrams are often used as the starting point for discussing the light absorbtion and emission. They exist in a variety of forms, to illustrate various molecular processes which can occur in excited states. A typical Jablonski diagram is sketched in fig.(3.8) The singlet ground, first and second electronic states are depicted by S_0, S_1 and S_2 respectively. At each of these electronic energy levels the fluorophores can exist in a number of vibrational levels (denoted by numbers).

At room temperature, thermal energy is not adequate to significantly populate the excited vibrational states. Absorbtion typically occurs from molecules with the lowest vibrational energy. Of course, the large energy difference between S_0 and S_1 excited states is too large for thermal population of S_1, and it is for this reason we use light and not heat to induce fluorescence.

Following light absorbtion, several processes usually occur. A fluorophore is usually excited to some higher vibrational level of either S_1 or S_0. With a few rare exceptions, molecules in condensed phases rapidly relaxes to the lowest vibrational level of S_1. This process is called internal conversion and generally occurs in 10^{-12} s or less. Since fluorescence lifetimes are typically near 10^{-8} s, internal conversion is generally complete prior to emission. Hence fluorescence emission generally results from a thermally equilibrated excited state, that is, the

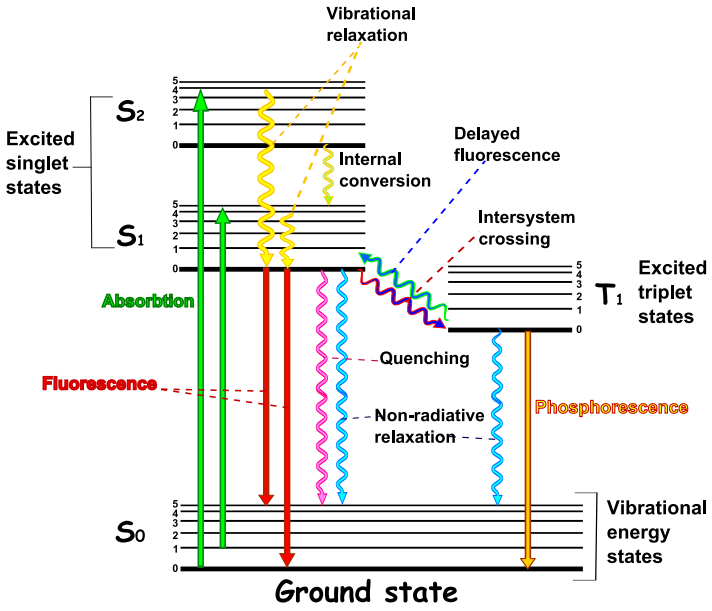

Figure 3.8: *One example of a Jablonski diagram*

lowest-energy vibrational state of S_1.

Return to the ground state typically occurs to higher excited vibrational ground-state level, which then quickly reaches thermal equilibrium. An interesting consequence of emission to higher vibrational states is that the emission spectrum is typically a mirror image of the absorbtion spectrum of the $S_0 \rightarrow S_1$ transition. This similarity occurs because electronic excitation does not greatly alter the nuclear geometry. Hence, the spacing of the vibrational energy levels of the excited states is similar to that of the ground state. As a result, the vibrational structures seen in the absorbtion and the emission spectra are similar.

Molecule in the S_1 state can also undergo to the first triplet state, T_1. Emission from T_1 is termed phosphorescence and is generally shifted to longer wavelengths (lower energy) relative to the fluorescence. Conversion of S_1 to T_1 is called intersystem crossing. Transition from T_1 to the singlet ground state is forbidden, and, as a result, rate contrasts for triplet emission is several order of magnitude small than those for fluorescence.

3.2.2 Characteristics of fluorescence emission

Examination of the Jablonski diagram (fig 3.8) reveals that the energy of the emission is typically less than that of the absorbtion. Hence, fluorescence typi-

cally occurs at lower energies or longer wavelength. This phenomenon was first observed by Sir. G. G. Stokes in 1852 in Cambridge, and then named after him.

Energy losses between excitation and emission are observed universally for fluorescent molecules in solution. One common cause of the Stokes shift is the rapid decay to the lowest vibrational of S_1. Furthermore, fluorophores generally decay to higher vibrational levels of S_0, resulting in further loss of excitation energy by thermalization of the excess vibrational energy. In addition to these effects, fluorophores can display further Stokes shift due to solvent effects, excited state reactions, complex formation, and/or energy transfer.

3.2.3 Fluorescence lifetimes and quantum yields

The fluorescence lifetime and quantum yield are perhaps the most important characteristics of a fluorophore. The quantum yield is the number of the emitted photons relative to the number of the absorbed photons. The fraction of fluorophores which decay through emission, and hence the quantum yield, is given by

$$Q = \frac{\Gamma}{\Gamma + k_{nr}} \tag{3.13}$$

where Γ is the emissive rate of the fluorophore and k_{nr} is its rate of non radiative decay to S_0.

The quantum yield can be close to unity if the radiation-less decay rate is much smaller than the rate of radiative decay, that is $k_{nr} \ll \Gamma$. We note that the energy yield of fluorescence is always less than unity because of Stokes losses.

The lifetime of the excited state is defined by the average time the molecule spends in the excited state prior to the return to the ground state. Generally, fluorescence lifetimes are near 10 ns, and can be expressed by

$$\tau = \frac{1}{\Gamma + k_{nr}}. \tag{3.14}$$

The lifetime of the fluorophore in absence of non-radiative processes is called the intrinsic or natural lifetime and is given by

$$\tau_n = \frac{1}{\Gamma}. \tag{3.15}$$

3.2.4 Fluorescence quenching and FRET

The intensity of fluorescence can be decreased by a wide variety of processes. Such decreases in intensity are called quenching. Quenching can occur by different mechanisms, such as collisions between molecules in solution. Beside collisional quenching, fluorescence quenching can occur by a variety of other processes. Fluorophores can form non fluorescent complexes with quenchers or other non molecular mechanisms such as attenuation of the incident light by the fluorophore itself or other absorbing species.

Another important process that occurs in the excited state is the Resonance Energy Transfer (RET). This process occurs whenever the emission spectrum of a fluorophore, called the donor, overlaps the absorbtion spectrum of another molecule, called the acceptor. The acceptor does not need to be fluorescent. It is important to understand that RET does not involve emission of light by the donor. RET is not the result of emission from the donor being absorbed by the acceptor. The donor and the acceptor are coupled by a dipole-dipole interaction. For these reasons, the term RET is preferred to term Fluorescence Resonance Energy Transfer (FRET), which is also in common use.

3.3 Optical cavities

Till now we have observed the resonant interaction between photons and atomic transitions of the same frequency. The atoms we considered were in the free space and the photon originated from external source. Now we wish to re-explore this process in more detail for the special case in which the interaction between the photons and the atom is enhanced by placing the atoms inside a resonant cavity.

First of all we need to remind some of the basic properties of optical cavities, restricting our attention to the simplest case of a planar cavity. This will be sufficient to illustrate the chief points, and the results can then be generalized to other types of cavity.

Consider the planar cavity shown in figure 3.9. The cavity consists of two plane mirrors M1 and M2, with reflectivity of R_1 and R_2, respectively, separated by an adjustable length L_{cav}. The space between the mirrors is filled with a medium of refractive index n and the mirrors are aligned parallel to each other so that the light inside the cavity bounces backward and forward between the mirrors.

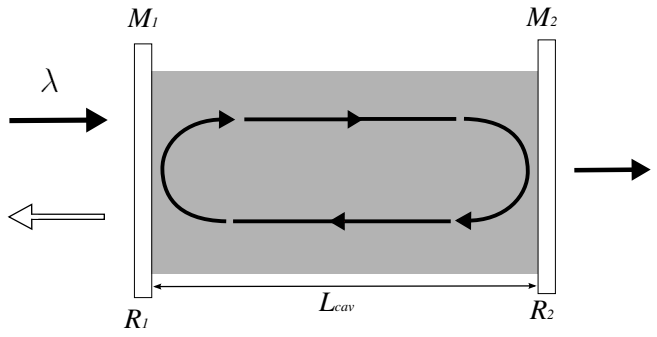

Figure 3.9: *A planar cavity of length L_{cav} with two parallel and mirrors M1 and M2 of reflectivity R1 and R2, respectively. The medium inside the cavity has a refractive index* n.

The properties of the planar cavity can be analyzed by considering the effect of introducing light of wavelength λ from one side and calculating how much get transmitted through to the other side. On the assumption that there are no absorption or scattering losses within the cavity, the transmission $\mathcal{T}$ is given by:

$$\mathcal{T} = \frac{1}{1 + (4\mathcal{F}^2/\pi^2 \sin^2(\phi/2))} \tag{3.16}$$

where

$$\phi = \frac{4\pi n L_{cav}}{\lambda} \tag{3.17}$$

is the round-trip phase shift, and

$$\mathcal{F} = \frac{\pi (R_1 R_2)^{1/4}}{1 - \sqrt{R_1 R_2}} \tag{3.18}$$

is the **finesse** of the cavity. It is easy to see from eqn 3.16 that the transmission is equal to unity whenever $\phi = 2\pi m$, where m is an integer. In this situation the cavity is said to be **on-resonance**. From eqn. 3.17 we see that the resonance condition occurs when the cavity length L_{cav} is equal to an integer number m of intracavity half wavelength:

$$L_{cav} = m\lambda/2. \tag{3.19}$$

The resonance condition thus occurs when the light bouncing around the cavity is in phase during each round trip.

The cavity resonance condition naturally leads to the concept of **resonant modes**. These are modes of the light field that satisfy the resonance condition and are preferentially selected by the cavity. Since the light field bouncing around

the cavity are all in phase, the waves interfere constructively and have much larger amplitudes than at non-resonant frequencies. The resonant modes have intensity inside the cavity enhanced by a factor $4/(1-R)$ compared to an incoming wave, while the out of resonance frequencies have their intensity suppressed by a factor $(1-R)$. The properties of the resonant modes play an essential part in determining the emission spectra of lasers.

3.3.1 Atom-cavity coupling

The coupling strength between the atom and the cavity can be classified as either strong or weak. In the following part we shall investigate the weak coupling.

Weak coupling occurs when the atom-cavity coupling constant g_0 is smaller than the loss rate due to either leakage of photons from the cavity or decay to non-resonant modes. Since the effect of the cavity is relatively small, it is appropriate to treat the atom-cavity interaction by perturbation theory.

As we have seen in the previous section the Fermi's Golden rule is used to calculate the emission rate for the atom in the free space. Here we are going to observe the revised rate for the atom coupled resonantly to a single mode cavity. We shall see that the main effect of the cavity is to enhance or suppress the photon density of states compared to the free space value.

Consider an atom in a single mode cavity of volume V_0 as shown in fig 3.10(a). The emission rate is given by Fermi's Golden rule. We assume that the cavity mode has a frequency ω_c with a half width $\Delta\omega_c$. The density of states function $g(\omega)$ for the cavity will then take the form shown in fig 3.10 (b). Since there is

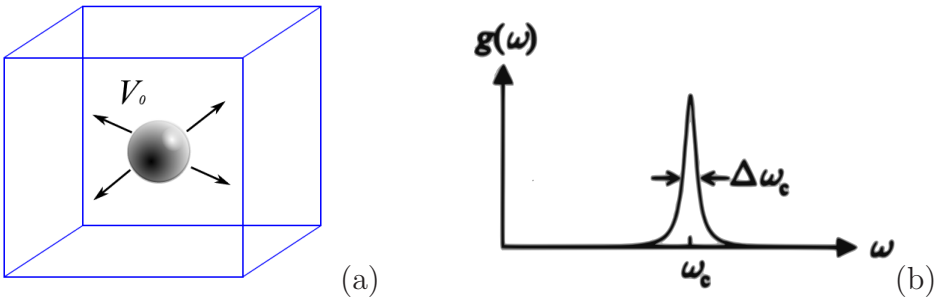

Figure 3.10: *(a)A two-level atom in a single-mode cavity with volume V_0. (b) Density of states function $g(\omega)$ for the cavity. The angular frequency of the cavity mode is ω_c, and $\Delta\omega_c$ is its linewidth.*

only one resonant mode, we must have:

$$\int_0^\infty g(\omega)d\omega = 1, \tag{3.20}$$

which is satisfied if we use a normalized Lorentzian function for $g(\omega)$ (cf. eqn **??**):

$$g(\omega) = \frac{2}{\pi\Delta\omega_c}\ \frac{\Delta\omega_c^2}{4(\omega-\omega_c)^2+\Delta\omega_c^2}. \tag{3.21}$$

If the frequency of the atomic transition is ω_0, then we must evaluate eqn 3.21 at ω_0 to obtain:

$$g(\omega_0) = \frac{2}{\pi\Delta\omega_c}\ \frac{\Delta\omega_c^2}{4(\omega_0-\omega_c)^2+\Delta\omega_c^2}. \tag{3.22}$$

At exact resonance between the atom and the cavity ($\omega_0 = \omega_c$), this reduces to:

$$g(\omega_0) = \frac{2}{\pi\Delta\omega_c} = \frac{2Q}{\pi\omega_0}, \tag{3.23}$$

where Q is the quality factor of the cavity, defined as:

$$Q = \frac{\omega}{\Delta\omega}. \tag{3.24}$$

3.4 Laser

The word 'laser' is an acronym that stands for ' Light Amplification by Stimulated Emission of Radiation'. Laser operation was first demonstrated in 1960, and since then, lasers have become essential tools in non-linear and quantum optics. In this section we give a brief review of the physical principles that underly laser operation.

3.4.1 Laser oscillation

Figure 3.11 shows a schematic diagram of a typical laser oscillator. The laser consists of a **gain medium** and two end mirrors called the **output coupler** and the **high reflector** with reflectivities of R_1 and R_2, respectively. Light bounces between the two mirrors and is amplified each time it passes through the gain medium. If the amplification in the gain medium is sufficient to balance the losses

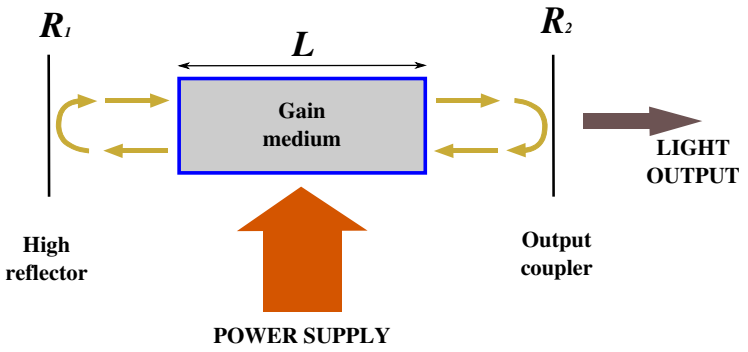

Figure 3.11: *Schematic diagram of a laser oscillator.*

during a round trip, then oscillation can occur and the laser will operate. The output of the laser emerges through the output coupler, which has a partially transmitting coating.

The light amplification that occurs within the gain medium is quantified by the gain coefficient $\gamma(\omega)$ defined by:

$$\frac{dI}{dz} = \gamma(\omega)I(z), \tag{3.25}$$

where I is the optical intensity, ω is the angular frequency of the light, and z is the direction of propagation of the beam, integration of equation 3.25 yields:

$$I(z) = I_0 e^{\gamma z}, \tag{3.26}$$

which shows that the light intensity grows exponentially inside the gain medium, in the absence of gain saturation (see below).

Let us consider the case in which the light beam is close to resonance with an atomic transition of angular frequency ω_0. The beam will trigger both absorption and stimulated-emission transition as shown in fig. 4.2. For amplification to occur, we require that the stimulated-emission rate should exceed the absorption rate, so that the number of photons in the beam increases as it propagates through the gain medium. From equation 3.5 we see that this occurs when:

$$B_{21}^{\omega} N_2 u(\omega) > B_{12}^{\omega} N_1 u(\omega) \tag{3.27}$$

which on substituting from eqn. 3.10, implies:

$$N_2 > \frac{g_2}{g_1} N_1. \tag{3.28}$$

In thermal equilibrium, the ratio of N_2 to N_1 is given by the Boltzmann formula of equation 3.8. This means that it is never possible to satisfy eqn. 3.28, and the light intensity decays as it propagates because the absorption rate exceed the stimulated-emission rate. Equation 3.28 can therefore only be satisfied in non-equilibrium conditions called **population inversion**. Population inversion is normally achieved by pumping energy into the medium to excite a large number of atoms to the excited state. The energy is derived from an external power source, as indicated schematically in fig 4.8.

The population-inversion density ΔN can be defined as:

$$\Delta N = N_2 - \frac{g_2}{g_1} N_1. \tag{3.29}$$

The gain coefficient that is achieved for an inversion density ΔN is given by:

$$\gamma(\omega) = \frac{\lambda^2}{4n^2\tau} \Delta N g_\omega(\omega), \tag{3.30}$$

where λ is the vacuum wavelength, n is the refractive index of the gain medium, τ is the radiative lifetime of the upper level, and $g_\omega(\omega)$ is the spectral lineshape defined in equation **??**. This shows that the gain is directly proportional to the inversion density and also to the transition probability via $1/\tau \equiv A_{21}$.

The population inversion required for laser oscillation is usually obtained by 'pumping' atoms to a higher level. Fig. 3.14 illustrates the general scheme for obtaining population inversion in a **four-level laser**. Atoms are pumped from the ground state to level 3 from where they decay rapidly to level 2, creating population inversion with respect to level 1. the pumping process to level 3 can be optical or electrical. The decay rate from level 1 back to the ground state must be fast to prevent atoms accumulating in that level and destroying the population inversion.

In normal operation the population inversion will be proportional to the pumping rate $\mathcal{R}$, which in turn is proportional to the power supplied by the pump source. The variation of the gain in the medium with the pumping rate will then be linear at first as sketched in fig 3.13.

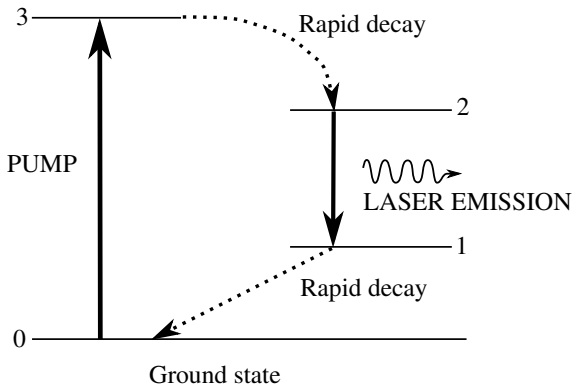

Figure 3.12: *Population inversion mechanism in a four level laser.*

However, a situation is eventually reached when the gain is sufficient to initiate laser operation. This is called **laser threshold**. At threshold, the laser begin to emit light, and the gain coefficient (and hence the population inversion) gets clamped at the threshold value.

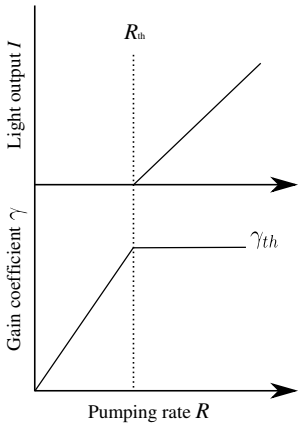

Figure 3.13: *Idealized variation of the gain coefficient and light output with the pumping rate R in a laser with a threshold R_{th}.*

The value of the gain coefficient at the threshold can be calculated by considering the amount of amplification required to maintain laser oscillation. In general, this is a rather complicated calculation, because the population inversion will often vary throughout the gain medium. Moreover, **gain saturation** occurs as the photon density inside the cavity increases. The analysis below is therefore only valid for a uniform gain medium in the weak-saturation limit.

In stable oscillation conditions, the increase of the intensity due to the gain must exactly balance the losses due to the imperfect reflectivity of the end mirrors and any other losses that may be present within the cavity. On following the beam through a round-trip of the cavity shown in fig. 3.11, we see that the oscillation condition can be written:

$$R_1 R_2 \xi e^{2\gamma L} = 1, \tag{3.31}$$

where L is the length of the gain medium and ξ is a factor that accounts for other losses such us scattering and absorption in the optics. The factor of two in the exponential allows for the fact that the light passes through the gain medium

twice during a round trip.

The oscillation condition in equation 3.31 can be written as:

$$\gamma = -\frac{1}{2L}\ln(R_1 R_2) - \frac{1}{2L}\ln\xi. \tag{3.32}$$

This defines the threshold gain γ_{th} required to make the laser oscillate. This gain will be achieved for a certain pumping rate $\mathcal{R}_{th}$, the gain cannot increase further since it is clamped by the oscillation condition. The extra energy of the pumping source thus goes into generating the light output, which increases linearly with $(\mathcal{R} - \mathcal{R}_{th})$ for $\mathcal{R} > \mathcal{R}_{th}$ in this simplified model, as shown in fig.4.10.

In an ideal laser in which the losses are low and the high reflector has near perfect reflectivity, the value of $\mathcal{R}_{th}$ is determined by the transmission of the output coupler. A low value of $(1 - R_1)$ will give a low threshold but also a low power output, because very little of the energy oscillating inside the cavity can escape. Conversely, a higher value of $(1 - R_1)$ increases the threshold, but also increases the output coupling efficiency, so that higher powers can in principle be obtained. In practice, the choice of the value of output coupler is often determined by the amount of power available from the pumping source.

3.4.2 Laser modes

The cavity is an essential part of a laser, providing the positive feed-back that turns an amplifier into an oscillator. Furthermore, it has a profound effect on the properties of the beam that emerges from the output coupler. In this section we briefly discuss the mode structure of the laser light that is determined by the cavity, starting with the spatial properties of the beam.

Consider the beam emerging through the output coupler of a laser as shown in fig. 4.11. The fact that the light rays have to bounce repeatedly between the

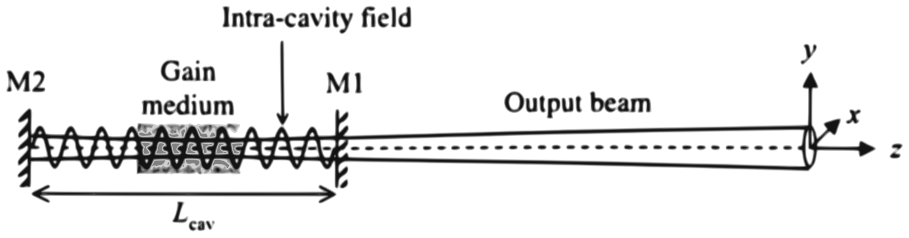

Figure 3.14: *Schematic representation of the output beam from a laser propagating in the z-direction.*

cavity mirrors leads to one of the most obvious properties of laser beams, namely that they are highly *directional*. In ideal circumstances, the beam will have only a very small divergence determined by the design of the cavity.

The variation of the electric field amplitude through a cross sectional slice of the beam is determined by the **transverse mode** structure. The modes are labeled by two integers m and n. If the beam is propagating in the z-direction as shown in figure 4.11 the (x,y)-dependence of the electric field amplitude for a particular mode is given by:

$$\mathcal{E}_{mn}(x,y) = \mathcal{E}_0 H_m(\sqrt{2}x/w) H_n(\sqrt{2}y/w) \exp\left(-\frac{x^2+y^2}{w^2}\right), \tag{3.33}$$

where H_m and H_n are Hermite polynomials, the first three of these Hermite polynomials are given by:

$$\begin{aligned} H_0(u) &= 1 \\ H_1(u) &= 2u \\ H_2(u) &= 4u^2 - 2. \end{aligned}$$

The parameter w that appears in equation 3.33 determines the width of the beam and is called beam spot size.

In general, the cross-section of the beam may be described by any of the transverse modes, or by a superposition of several of them. However, it is normal to try to operate the laser on the 00 mode, which has a Gaussian field distribution:

$$\mathcal{E}_{00}(x,y) = \mathcal{E}_0 \exp[-(x^2+y^2)/w^2] \equiv \mathcal{E}_0 \exp(-r^2/w^2), \tag{3.34}$$

where $r = \sqrt{x^2+y^2}$ is the radial distance from the center of the beam. The 00 mode is the closest approximation to an idealized ray of light that can be found in nature. It as the smallest divergence of all the modes and can be focused on to the smallest size.

Now let us consider the **longitudinal mode** structure of the laser, which relates to the variation of the electric field with z, where the z-axis lies along the cavity axis. The light bouncing repeatedly around the cavity must have nodes (field zeros) at the mirrors because they have high reflectivities. The intra-cavity field is therefore a standing wave, with an integer number of half wavelengths inside the cavity, as shown in fig 3.14. If the length of the cavity is L_{cav}, the

standing wave condition can be written as:

$$L_{cav} = \text{integer} \times \frac{\lambda}{2} = \text{integer} \times \frac{\pi c}{n_{cav}\omega}, \tag{3.35}$$

where n_{cav} is the average refractive index within the cavity. This can be rearranged to give the allowed angular frequencies of the cavity modes:

$$\omega_{mode} = \text{integer} \times \frac{\pi c}{n_{cav} L_{cav}}, \tag{3.36}$$

which implies that the modes are separated in angular frequency by:

$$\Delta\omega_{mode} = \frac{\pi c}{n_{cav} L_{cav}}. \tag{3.37}$$

Thus the longitudinal-mode spacing is larger in shorter cavities.

The longitudinal-mode structure, together with the properties of the gain medium, determine the emission spectrum of the laser. For a given mode to oscillate, its frequency must lie within the linewidth of the laser transition as determined by this lineshape function $g_\omega(\omega)$. It will normally be the case that the mode spacing is much smaller than the linewidth, and so there will be many modes that satisfy this condition, as illustrated in fig 3.15(a)

If the line broadening is inhomogeneous, as with Doppler-broadened lines in a gas laser, the different atoms that contribute to different parts of the spectrum can support lasing on any of the modes that have sufficient gain to overcome the cavity losses, and the laser will oscillate in many modes simultaneously. This type of operation is called **multi-mode**. In the case where the laser is operating well above threshold, most of the modes that fall within the spectral line of the transition will have gain to oscillate. In this situation, the spectral width of the laser is roughly the same as that of the equivalent line in a discharge lamp. Since the modes are effectively independent of each other in an inhomogeneous gain medium, their relative optical phases are random.

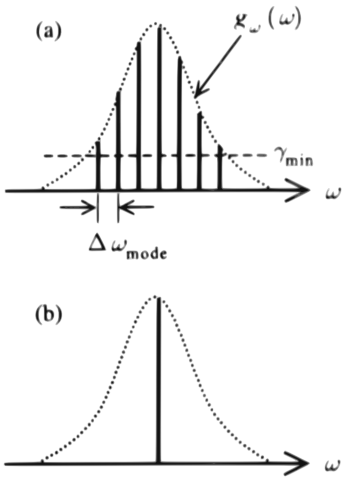

Figure 3.15: *(a)Multi-mode and (b) Single-mode operation of a laser with longitudinal line spacing $\Delta\omega_{mode}$.*

Fig.3.15(b) illustrates the **single-mode** operation of the laser in which only

the longitudinal mode is oscillating. Single-mode operations are typically achieved by introducing a frequency-selective element such as a Fabry-Perot etalon into the cavity. The etalon introduces a frequency-selective loss into the cavity, thereby picking out the single longitudinal mode with the lowest loss. In this mode of operation, the linewidth of the laser is very narrow, being determined by the properties of the cavity rather than the atomic transition.

A third important mode of operation of the laser is called **mode-locked**. In this case, the laser operates on as many longitudinal modes as the gain medium can support, but the phases of all the modes are locked together. The temporal properties of the output beam can be found by taking the Fourier transform of a comb of fields with a regular frequency separation given by eqn. 3.37 and with their amplitude modulated by the gain spectrum of the laser transition. The regular frequency spacing of the modes leads to a regular train of pulses separated in time by $2n_{cav}L_{cav}/c$. The duration Δt of the pulses is determined by the spectral width of the gain according to the time-bandwidth product:

$$\Delta\omega\Delta t \sim 1, \tag{3.38}$$

where $\Delta\omega$ is the spectral width of the gain medium. Shorter pulses are therefore generated by gain media with a very broad spectral range. Dye lasers for example have very broad gain bandwidths, and can be used to generate pulses in the femtosecond time range.

3.4.3 Mirrorless lasing

Laser oscillators consist, as we have described previously, of a laser medium which provide gain and a resonator structure which provide the feedback necessary for the build-up of oscillation. The resonator is commonly formed by two end mirrors terminating the laser medium. In 1971, Kogelnik & Shank proposed that the external cavity was not required for lasing and the Bragg reflections in periodic structure could play a role similar to the external mirrors. Such distributed feedback lasing was demonstrated, and it forms the basis of mirrorless lasing in liquid crystals today. In figure 3.16 is shown a simplified illustration which demonstrates the operation of a distributed feedback structure. In the diagram we show two waves represented by arrows, one which travels to the left and the other to the right. As each wave travels in the periodic structure, it receives light at each point along its path by Bragg scattering from the opposite traveling wave.

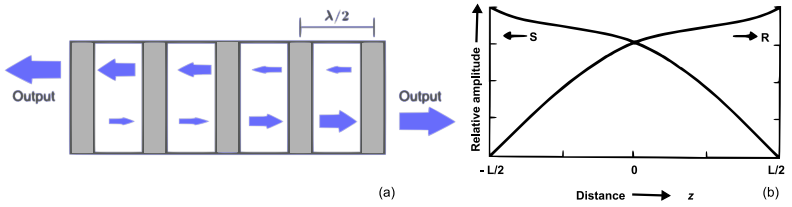

Figure 3.16: *(a)Illustration demonstrating laser oscillation in a periodic structure (b)Plot of the amplitude of left traveling wave S and right traveling wave R vs. distance*

This creates a feedback mechanism which is distributed throughout the length of the periodic structure. Since the periodic structure also has gain one can see that, with sufficient feedback, there will be a condition for oscillation. Spectral selection occurs due to the wavelength sensitivity of the Bragg effect.

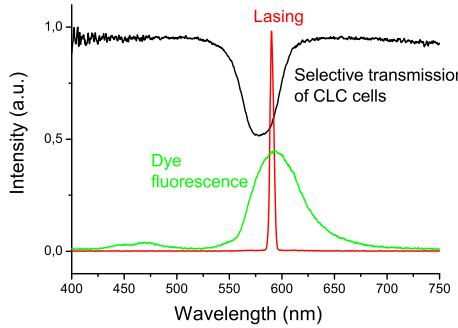

Figure 3.17: *Example of the mirror-less laser effect from a cholesteric liquid crystal doped with fluorescent molecules. In figure is represented the band gap of the cholesteric liquid crystal (black curve), the fluorescent emission of the dye used as gain medium (green curve) and the laser peak at the edge of the band gap (red curve).*

As we have described in the previous sections 2.4 and 2.5, in layered structures as well as in cholesteric liquid crystals, the Bragg reflection causes the presence of a stop band (black curve in fig. 3.17) in which the propagation of waves is forbidden. At the edges of these regions the group velocity approaches to zero and the density of states dramatically increases (sec. 2.6), then in this position we have the maximum probability to have a laser emission, as we have already described in sec. 3.1.2.

The presence of luminescent molecules within the cholesteric structure, that play the role of a gain medium, gives the condition for the oscillation. Matching then the fluorescence emission (fig. 3.17, green curve) with the stop band (black

curve), it is possible to observe laser emission close to the edge of the band gap (fig. 3.17, red curve).

3.4.4 Defect modes in the periodic and chiral structure

The important role of photonic defects has been understood from the very beginning of the investigation on photonic crystals. Suppose that the defect consists of a single layer of the one-dimensional photonic crystal that has a different width than the rest (fig.3.18)

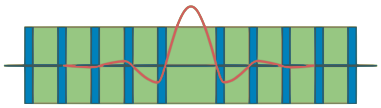

Figure 3.18: *A defect in a multilayer film, formed by enlarging one of the layers of dielectric. Also sketched is the displacement field strength associated with a defect state.*

We restrict our attention to the propagation along one axis and consider a mode with frequency Ω in the photonic band-gap. There are no extended modes with frequency Ω inside the periodic lattice, and introducing the defect will not change the fact. The destruction of periodicity prevents us from describing the modes of the system with wave vector k, but we can still employ our knowledge of the band structure to determine whether a certain frequency will support extended states inside the rest of the crystal. In this way, we can divide up frequency space into regions in which the states are extended and regions in which they are evanescent, as in figure 3.19.

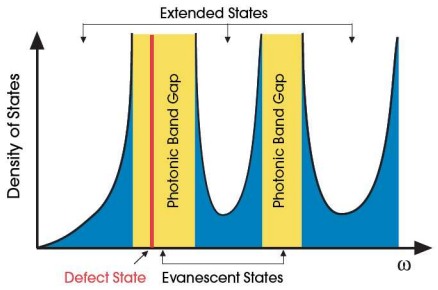

Figure 3.19: *The division of frequency space into extended and evanescent states. In this sketch the density of states is zero in the band gaps of the crystal (yellow). Modes are allowed to exist in these regions only if they are evanescent, and only if their translational symmetry is broken by a defect. Such a mode is shown in red.*

Defects may permit *localized* modes to exist, with frequencies inside photonic band gaps. If a mode has frequency in the gap, then it must exponentially decay once it enters the crystal.

The density of states of a system is the number of allowed states per unit increase in ω. if a single state is introduced into the photonic band gap, then the density of states of the system in figure 3.19 is zero in the photonic band gap, except for a single peak associated with the defect.

The use of defect modes inside the photonic band gap is an other mechanism for generating lasing at low thresholds.

Part II

Experiments

Chapter 4

Mirrorless lasing in liquid crystals

Citing the work of Kogelnik & Shank [27], in 1973, Schnur & Goldberg proposed and obtained a US patent on a tunable internal-feedback liquid crystal dye laser [28]. However, there is no corresponding demonstration or evidence of lasing in the literature. Their basic idea is to use a fluorescent dye dissolved in the liquid crystal to provide gain, and to use the periodic structure of helical cholesterics to provide distributed feedback. To demonstrate lasing, in addition to light emission, line narrowing, directional emission, excited state lifetime reduction, threshold behaviour and coherence must also be demonstrated. Ilchishin et al. [29] have demonstrated modification of the fluorescent emission, but the first unequivocal demonstration of lasing in polymer-stabilized cholesteric liquid crystals was by the group of Genack [30] and, shortly thereafter, independently in pure cholesterics by Taheri et al. [31].

The laser emission is directional, coherent, typical line widths, full width at half maximum (FWHM), are approximately 2 Å, with a pump thresholds of approximately 10 nJ and light-to-light efficiency of approximately 20%. Mirrorless lasing has been demonstrated using two dyes with Förster transfer [32, 33], as well as with no dye, where the liquid crystal itself is the active medium [34]. Lasing has been observed in free-standing helical cholesteric polymer films [35, 36]. Finkelmann synthesized cholesteric elastomers, whose pitch could be varied by biaxial extension [37]. These materials could be made to lase, and the lasing wavelength of these 'rubber lasers' could be tuned by stretching the samples [38]. Haase & Ozaki demonstrated mirrorless lasing in another periodic dielectric struc-

ture, ferroelectric liquid crystals [39]. The lasing wavelength in these materials can be tuned by an applied electric field [40, 41]. Recently, electrically [42] and mechanically [43] tunable lasing in helical cholesterics was demonstrated. Since the pitch depends on temperature, the lasing wavelength can be tuned by changing the temperature. Interestingly, changing the temperature results not only in smooth variations of the wavelength, but also in abrupt jumps [44, 45]. By the incorporation of photosensitive moieties, such as azo dyes, the cholesteric pitch can be varied by illumination. Tuning of the lasing wavelength by light has been demonstrated by a number of groups [46–49]. Shibaev et al. [50] have also demonstrated chemical tunability, where the lasing wavelength depends on pH. Two-photon lasing, where excitation is via two-photon absorption, and where lasing occurs at a shorter wavelength than that of the pump, has been demonstrated by Bunning [51] and Shirota et al. [52]. If two cholesteric films are put together so that the helical structure is not continuous across the interface, an allowed state associated with the defect appears in the band gap. Lasing can occur at this wavelength; such defect mode lasing has been demonstrated by a number of groups [53–55]. The dependence of lasing thresholds on sample thickness and dye concentration has also been studied recently [56].

In this chapter we present the achievements we have obtained in improving the performances of dye doped cholesteric liquid crystals laser. In particular we have focused our attention on two main issues: stability and emission.

4.1 Lasing from cholesteric liquid crystals: stability

One of the main drawbacks of CLC lasers limiting their technological application is their low stability. This is connected with two phenomena occurring under the influence of a powerful pumping: gradual deformation of the CLC layer planar orientation and degradation of the luminescent dye molecules. A lot of effort has been dedicated to solve these problems and to optimize the lasing conditions.

In the following subsections we will present different ways to improve the stability of the cholesteric liquid crystal lasers.

4.1.1 Rotating cell

The problem of dye molecules degradation is common to conventional dye lasers as well. To solve this problem, in these lasers the dye solvent is circulating continuously through the laser chamber avoiding the saturation effects from pumping [57]. Since in CLC dye doped lasers it is impossible to make the dye circulate separately from the CLC structure, to improve the stability of lasing emission we have developed a mechanism that allows the rotation of the whole CLC cell. In this case an improvement of stability in both dye molecules and CLC structure can be expected.

A conventional CLC laser cell with dimensions approximately 2x2 cm^2, with a thickness around 40 μm, was placed on a specially designed holder providing rotation of the cell around the axis perpendicular to the plane of the cell (Fig. 4.1). The rotation speed of the CLC cell was approximately 100 revolutions per minute

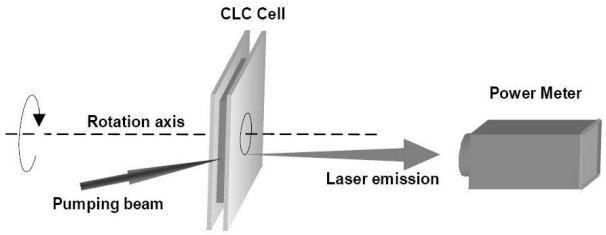

Figure 4.1: *Sketch of the experimental setup.*

and the radius of the circle described by the pumping beam was 5-7 mm. As pumping laser a nitrogen laser, Model VSL-337ND-S (Spectra Physics) was used. The pulse wavelength and duration were 337 nm and 4 ns respectively. The laser beam was focused by a lens (f = 10 cm) to reduce the spot size on the cell to few hundreds of micrometers. The pumping beam hits the sample at 45° with respect to the cell normal (a usual geometry for this kind of experiment). The repetition rate of pulses was 7 Hz and the average pumping power was 45 μW. A power meter (Thermo Oriel Instruments) was used to monitor laser emission. It must be noticed that an average power, averaged during several seconds of measurement (not per single pulse), was measured. CLC mixtures were composed of nematic ZLI-6816 and optically active dopant MLC- 6247 (Merck Ltd, Darmstad). The helical pitch in each mixture was set to provide lasing near the wavelength of dye fluorescence maximum. The following luminescent dyes were used:

1. UVITEX
   (2,5-2,5-thiophenediylbis(5-tert-butyl-1,3-benzoxazole);

2. Oxazine700
   (3,5,6-tetrahydro-1H,4H-hinolizino[9,9a,1-bc]benzo[i] phenoxazinon-13);

3. DCM
   (4-Dicyanomethylene-2-methyl-6-(*p*-dimethylaminostyryl)-4H-pyran, (Exciton).

All of these dyes effectively absorb the nitrogen laser pumping beam. DCM was used as a sensitizer in a Forster coupling effect with Oxazine700 as an emitter. The following dye doped CLC mixtures were investigated:

1. 99.4%[75.5%ZLI-6816 + 24.5%MLC-6247] + 0.6%Oxazine 700

2. 99.4%[63.5%ZLI-6816 + 36.5%MLC-6247] + 0.6%UVITEX

3. 99.2%[76.5%ZLI-6816 + 23.5%MLC-6247] + 0.6% DCM + 0.2%Oxazine 700.

The time stability of laser emission power for rotating and motionless cells was investigated. The measurements showed that the lasing power of motionless cell decreases significantly during half a minute (Figs. 4.2-4.4, *black*). For the rotating cell during the same time no noticeable change in the output power is detected (4.2(a, *red*)). Other investigations showed that strongly orienting surfaces improve the stability and efficiency of lasing. In cells, whose plates were covered with polyimide (LQ1800, Hitachi Chemicals) and containing UVITEX dye, the output power did not change during two hours (Fig.4.2 (a,*red*)), while the cell without the orienting polyimide layer showed lower initial power and lower stability (Fig.4.2 (b, *red*)).

However, when the Oxazine was used as dye in a cell with polyimide layers a decrease of the output power during one hour was observed (Fig. 4.3). As it could be expected, the cell with Forster transfer effect showed the highest output power, but during one hour the output power slowly decreased (Fig. 4.4). Sufficient slackening of degradation of the planar CLC structure and the luminescent dye in the CLC lasers was achieved rotating the CLC cell. An increase of lasing stability was demonstrated. The operating time of the laser increases by several times if compared with the fixed cells. A rotational movement of the cell was used because

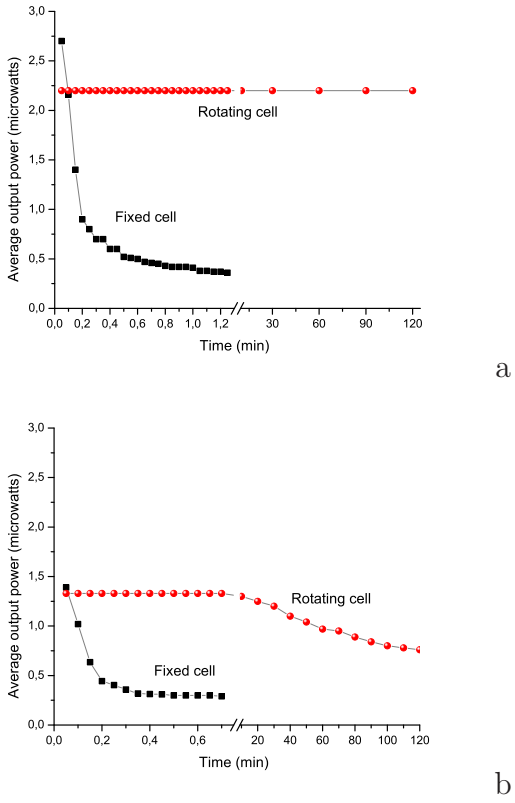

Figure 4.2: *Average output power for a 20 µm cell coated (a) and not coated (b)with polyimide and containing 0.6% UVITEX dye. The laser emission wavelength is at 443 nm.*

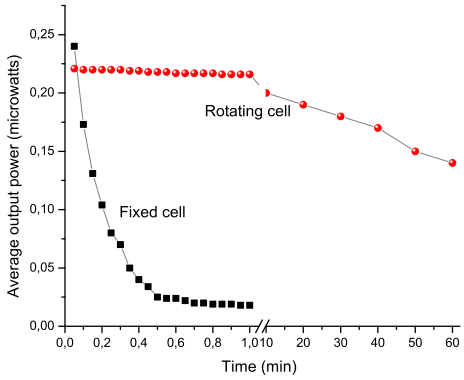

Figure 4.3: *Average output power for a 20µm cell coated with polyimide and containing 0.6% Oxazine 700 dye. The laser emission wavelength is at 623 nm.*

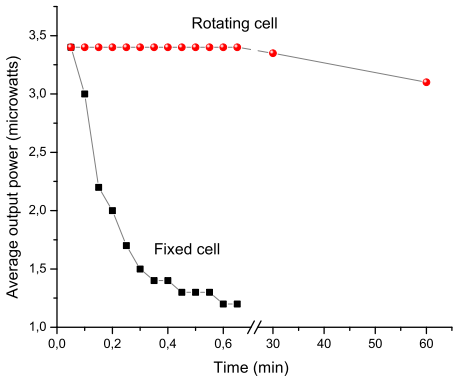

Figure 4.4: *Average output power for a 20µm cell coated with polyimide and containing 0.6% DCM and 0.2% Oxazine 700 for Foster transfer effect. The laser emission wavelength is at 615 nm.*

of its easy implementation. Degradation of the material in this case occurs along a narrow ring while the most part of the cell area remains unused. Applying more complex movements to the cell with respect to the pumping beam, allows to use the entire area of the cell and to obtain, as a result, a longer operating time of the laser. The remaining lasing instability for a moving cell is mainly expressed by the laser fluctuations which, are due to the spatial homogeneity of the CLC structure.

4.1.2 Multilayer sandwiched system

As previously stated, to improve laser stability we have have investigated a new concept for the cell assembly. In particular we have introduced a defect in the whole system. The introduction of defects enhanced fluorescence and laser emission in a dye doped cholesteric liquid crystal system [cite 27]. In this case lasing was observed inside the band gap. The enhancement in lasing efficiency and the reduction of pumping energy in defects induced structures in photonic crystals was predicted in [cite 28,29]. The introduction of a defect into the CLC could be achieved in two ways: by replacing a part of the host medium with a material that has a different dielectric constant e.g. two layers of CLC sandwich a thin layer of an isotropic medium [58]; by introducing a phase jump inside the CLC cell [59].

We have investigated the defect mode lasing in a multilayer system consisting

of a dye doped isotropic solvent sandwiched between two CLC cells.

The separation of the CLC and the active medium allows:

1. to avoid the degradation of the CLC structure caused by the absorption of the pumping energy,
2. to use dyes not soluble in LCs,
3. to use the optimal thickness both for the CLC layer and for the dye solution layer (thicker dye layer and thinner CLC layer).

We used the nematic MLC-6816 (Merck, cyclohexylcyclohexanes), transparent in UV range. A right handed chiral dopant MLC-6248 (Merck) was added to the nematic in order to induce the cholesteric structure. Rhodamine-6G was used as dye not soluble in LCs, and glycerol was used as isotropic solvent.

The cells, consisting in a dye/solvent layer sandwiched between two CLC layers, were the combination of four 0.8 mm thick glass plates separated by teflon spacers setting the thicknesses of each layer. The thickness of the CLC layers was 10 microns, and the thickness of the dye solution was 200 microns (Fig.4.5). To get good planar orientation of the CLC layers, the corresponding surfaces were coated with rubbed PVA (Polyvinyl alcohol) orienting layers. The second harmonic of

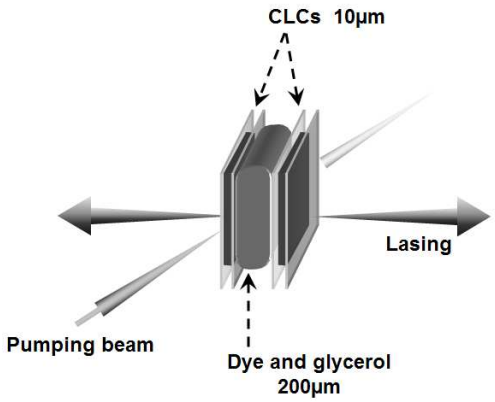

Figure 4.5: *Scheme of the sandwich cell*

a Q-switched Nd:YAG laser (Continuum, Surelite II) was used as pumping light source. The pulse wavelength, width, and repetition rate were 532nm, 4ns, and 1 Hz, respectively. The laser beam was attenuated and focused by a lens (f=20cm) to reduce the spot of the laser beam on the cholesteric cell to a few hundreds of micrometers. The pump beam irradiated the sample at an angle of 45° with

respect to the cell normal. An optical fiber, coupled to a spectrometer Avantes (AvaSpec-2000, with a resolution of 0.8 nm), collected the light emitted from the sample. The investigated structure was the one studied theoretically in [58], for which the typical defect mode lasing was expected. Indeed, multimode lasing within the stop band with several emission peaks was observed when the helical pitches of the two CLC layers were the same. To achieve single-mode lasing the CLC cells were filled with two distinct cholesteric mixtures, whose pitches were shifted so that only the edges of the band gaps overlapped. In Fig.4.6

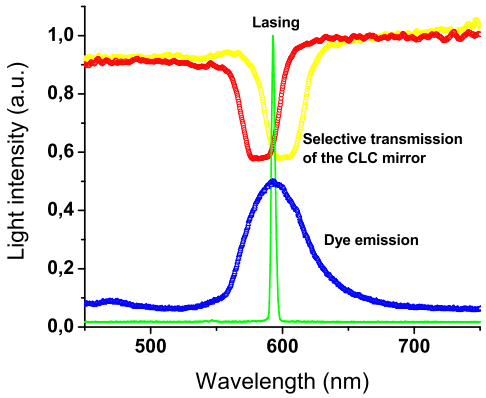

Figure 4.6: *Transmission spectra of the two cholesterics with different pitches (red and yellow), fluorescence of the dye (blue) and lasing spectrum from the sandwich cell (green).*

the transmission spectra of each CLC layer (*red and yellow curves*), the spectra of dye solution emission (*blue curve*) and lasing in this cell (*green*) are shown. A single mode lasing occurs in the overlapping part of CLC band gaps. In this experiment the CLC pitches were chosen to set the lasing peak near the maximum of the dye luminescence peak. In contrast with the conventional dye lasers with usual dielectric mirrors, in this kind of CLC lasers the wavelength of lasing is strongly connected with the CLC pitches. By choosing other CLC pitches, one obtains lasing at another wavelength. In Fig.4.7 the selective transmission of two different CLC layers superposed one to the other is shown: lasing occurs in the middle of the total band gap. The threshold of laser generation was estimated to be 0.75 μJ/pulse. A photograph showing the cell and the screen with the laser beam spots is presented in Fig.4.8. The distance between the cell and the screen is 30 cm. Also note that simple glass plates produced for medical applications were used in our experiments. Obviously, the quality of their surfaces is far from

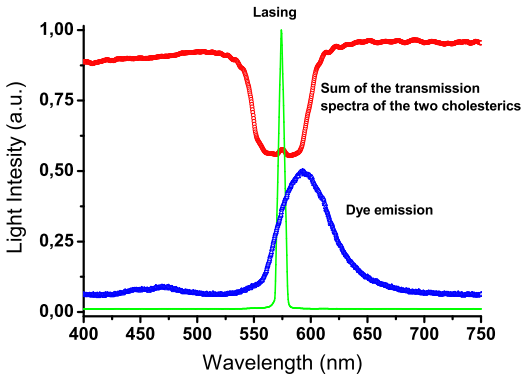

Figure 4.7: *Sum of the transmission spectra of the two cholesterics (red), fluorescence of the dye (blue) and lasing spectrum from the sandwich cell (green).*

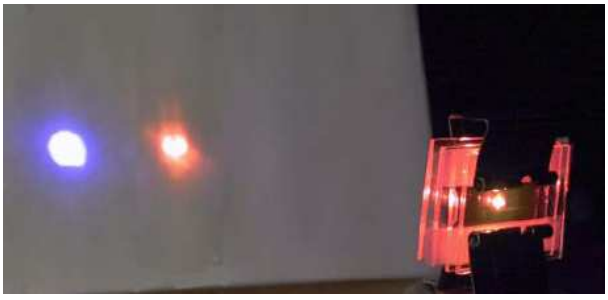

Figure 4.8: *Laser emission from the sandwich cell.*

being ideal for optical purposes, but, in spite of this, the divergence of the laser beam is considerably lower than the one usually observed in conventional dye doped cholesteric lasers. Besides Rhodamine-6G, another dye Stilbene-420, whose absorption and emission peaks are located in UV and violet ranges, was exploited as well. In this case, the CLC pitches were set to get lasing in violet spectrum range and a nitrogen laser (λ= 337nm) was used for pumping. Multimode lasing in the structures with equal CLC pitches and single mode one in the shifted pitch configuration were observed, confirming the general behavior

4.1.3 Surface treatment influence

In 4.1.1 we have stated that in a cell whose plates were covered with polyimide, as aligning polymer, the laser output power was higher and more stable in time if compared with a cell without any aligning polymer (fig. 4.2 a and b), then we assume that the role of the surface aligning treatment is important in enhancing the laser performances, as well as its efficiency and stability.

We have investigated the role of the surface treatment on the accommodation of the cholesteric helix and its influence on the laser characteristics. This study was focused on different polymers, commonly used in liquid crystals research:

- PI PolyImide [(LQ-1800) Hitachi chemicals]
- PVA (Poly-Vinyl alcohol) [Sigma Aldrich]
- PVP (Poly Vinyl Pirrolidone)

Different measurements were carried out using these polymers: pre-tilt angle, band gap properties and laser emission efficiency.

As nematic liquid crystals MLC-6815/6816 and as chiral dopants MLC-6247/6248 (Merck, Germany) were used. Nematic liquid crystals are UV transparent and have a good thermal stability while the chiral dopants have the proper helical twisting power in order to obtain pitches of the cholesteric helix comparable with the visible light wavelength. As photoluminescent dopants DCM *(4-Dicyanomethylene-2-methyl-6-(*p-*dimethylaminostyryl)-4H-pyran, (Exciton)* were used.

Cells were prepared using glass plates covered with a thin layer of rubbed polymers. PVA and PVP were prepared using a concentration of 0.5 wt% in water, spin coated and then cured in the oven for one hour at 110°C. PI was prepared at

two different concentrations 2 wt% and 10 wt% in 1-methyl-2-pyrrolidinone, spin coated and cured 1 h at 180°C and 1h at 250°C. The thin films were rubbed separately using different velvet cloths and the cells were assembled in two different configurations.

Figure 4.9: *Schematic representation of the assembled cell with the rubbing directions parallel and anti-parallel.*

In the first configuration glasses were aligned with the rubbing directions parallel to each other while in the second one the directions were antiparallel(fig. 4.9).

Three sets of cells were prepared. The first two sets, with 40 μm thickness, were prepared for band gap measurements and lasing experiments while the third set, with 5 μm thickness for pre-tilt angle measurements. To measure transmission properties, cells were filled with the mixture (74.1%MLC-6816 + 25.9%MLC-6248). For the lasing experiments a 0.4 wt% DCM was added to the mixture while for pre-tilt angle measurements homogeneously tilted cells were filled with plain MLC-6816.

Investigations on photoexcitation were performed using as a source a nitrogen laser, Model VSL-337ND-S (Spectra-Physics). The pulse wavelength, width, and repetition rate were 337 nm, 4 ns, and 1-10 Hz, respectively. The laser beam was focused by a lens f =10 cm to reduce the spot size onto the cell to few hundreds of micrometers. The pump beam hit the sample at 45° with respect to the cell normal, a usual experimental geometry for this kind of experiment. An optical fiber coupled to the spectrometer Avantes Fiberoptics Model AVASPEC-2048, with 1.4 nm resolution, collected the light emitted from the samples. A sketch of the laser set-up described is depicted in fig. 4.10.

A preliminary measure on the laser peak from two different cells, whose glasses were coated with PVA and PI respectively (fig 4.11)showed that the emission from the PVA coated cell is higher in comparison with the one coated with polymide.

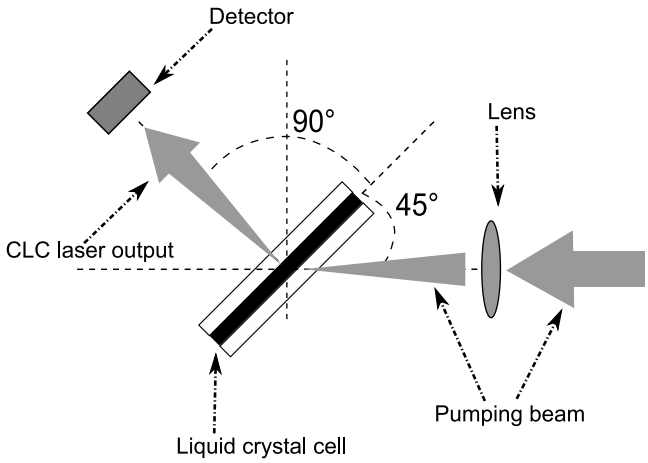

Figure 4.10: *Schematic representation of the usual experimental geometry for the investigation on the laser effect from cholesteric liquid crystal cells.*

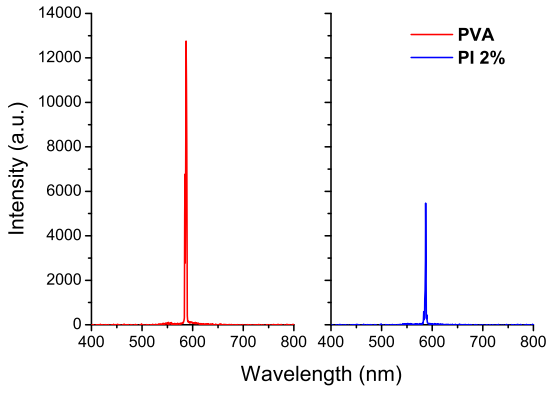

Figure 4.11: *Laser emission from a dye doped cholesteric liquid crystals mixture for two cells prepared PI 2%(blue) and PVA.(red)*

The influence on the photonic band gap position was evaluated for the rubbed parallel and antiparallel PVA and PI. From figure 4.12, it is evident that the

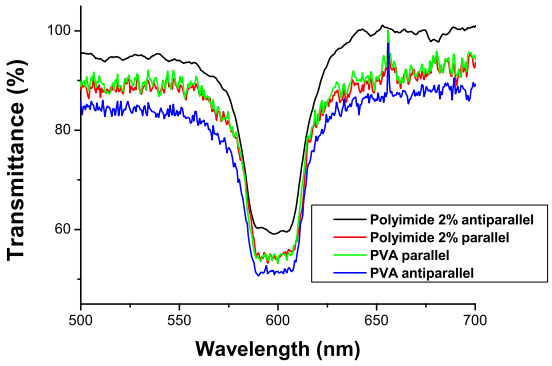

Figure 4.12: *Transmission spectra for the cholesteric mixture 74.1%MLC-6816+25.9%MLC-6248 confined in cells with PVA coated glass plates, aligned parallel (green) and anti-parallel (blue)and in cells with PI 2% coated glass plates aligned parallel (red) and antiparallel (black).*

different substrates and assembly of the cell do not influence the position of the selective reflection band that is always centered on 600 nm and has a width of about 25nm. We can infer that the alignment polymer is not influent on the pitch of the cholesteric helix.

Cells containing the cholesteric mixture doped with a photoluminescent dye were filled and the laser emission was investigated.

In figure 4.13 it is shown that the emission from the cell coated with antiparallel rubbed PI 2% is 15% less intense with respect to the one from the cell coated with antiparallel rubbed PVA. The emission from a cell coated with parallel rubbed PI 2% is about 30% less intense with respect to the one from the cell coated with PVA. The lasing intensity from the cell containing antiparallel rubbed PVA shows to be the most efficient one, around 30% more intense with respect to the parallel rubbed PVA. For all this set of measurements the pumping power was set at 1.15 μW.

After these preliminary measurements a deeper investigation was carried out, including different concentrations and different polymers, figure 4.15 shows, as expected from the preliminary results, that the lasing intensity from the cell assembled with antiparallel rubbed PVA 4.15(a) is the most efficient, if compared with the laser emission from all the other cells. For this second set of measures

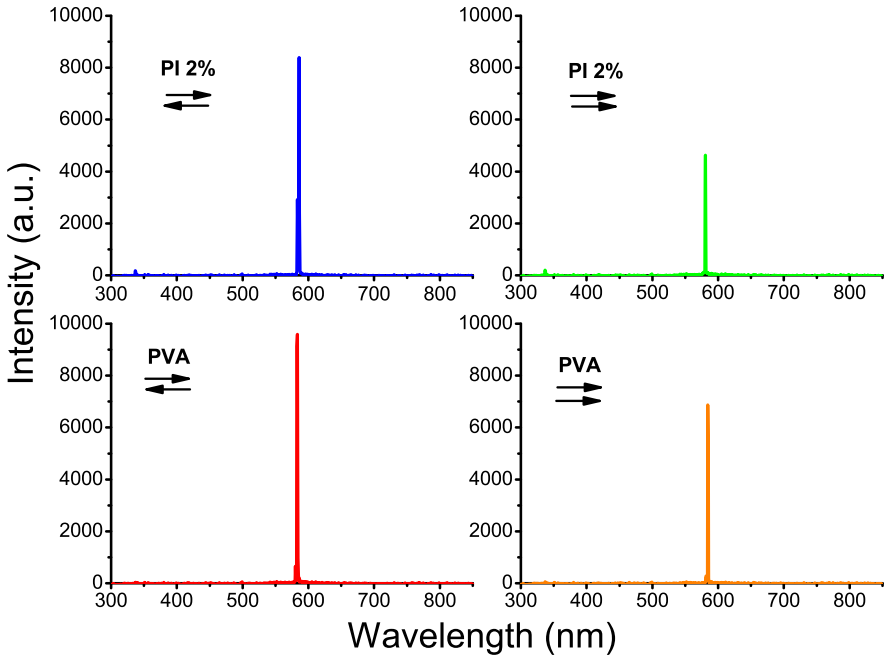

Figure 4.13: *Laser emission from the dye doped cholesteric liquid crystals mixture for cells with parallel and anti-parallel rubbed PI 2% (green and blue) and PVA (orange and red).*

the pumping power was fixed at 1.50 μW.

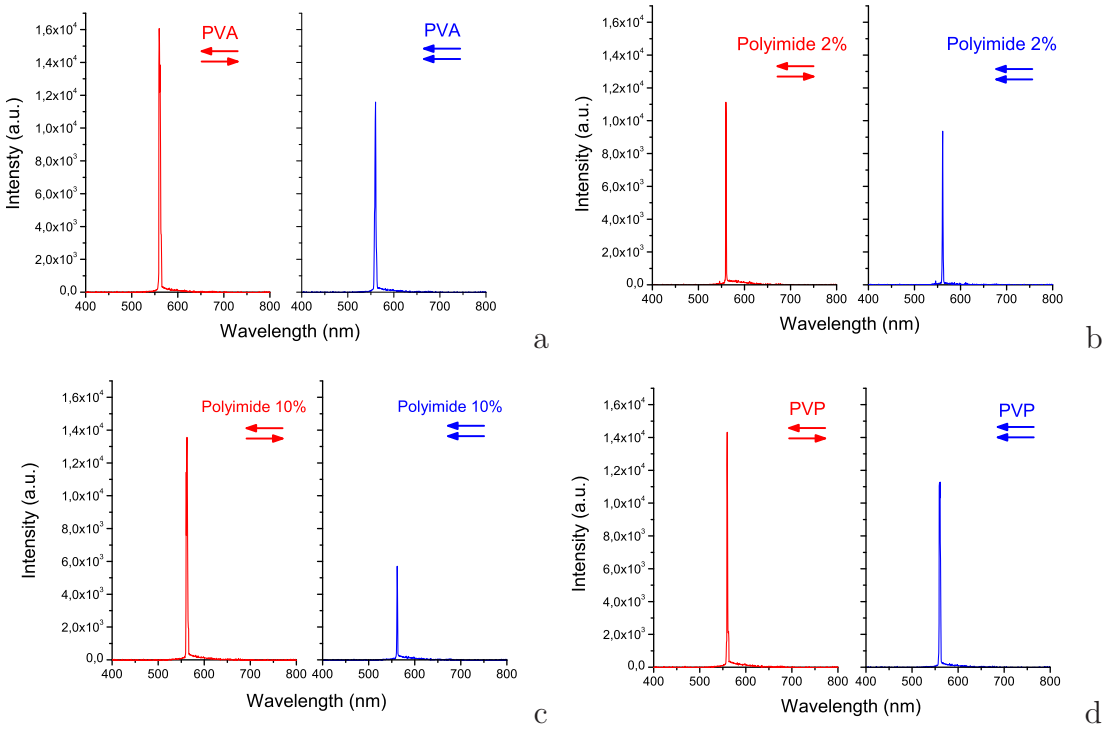

Figure 4.14: *Laser emission from the dye doped cholesteric liquid crystals mixture for cells with parallel and antiparallel PVA (a), Polyimide 2% (b) and 10% (c) and PVP (d).*

The pretilt angle was measured for the different aligning surfaces.

The rotating crystal method allows the accurate determination of tilt angles without need of measuring the cell thickness [60]. It is based on measurement of the optical phase shift as a function of rotation angle. The liquid crystal sample is manufactured in such a way that no twist or bend are present. It can be rotated around an axis parallel to the substrates, the director is in a plane perpendicular to the rotation axis of the sample. The incident beam from an He-Ne laser is split in two part: a reference and signal arm. The reference beam pass trough a linear polarizer with its axis at 45 degrees with respect the rotation axis of the sample. The signal go through a linear polarizer (at 45 degrees), the sample and a quarter wave plate with its axis at 45 degrees (the signal upon exit from the sample is elliptical polarized and the quarter wave plate transform it into a rotated linear polarized one). Both the signal and the reference impinges on a rotating analyzer and are recorded by two photodiodes connected to a lock in

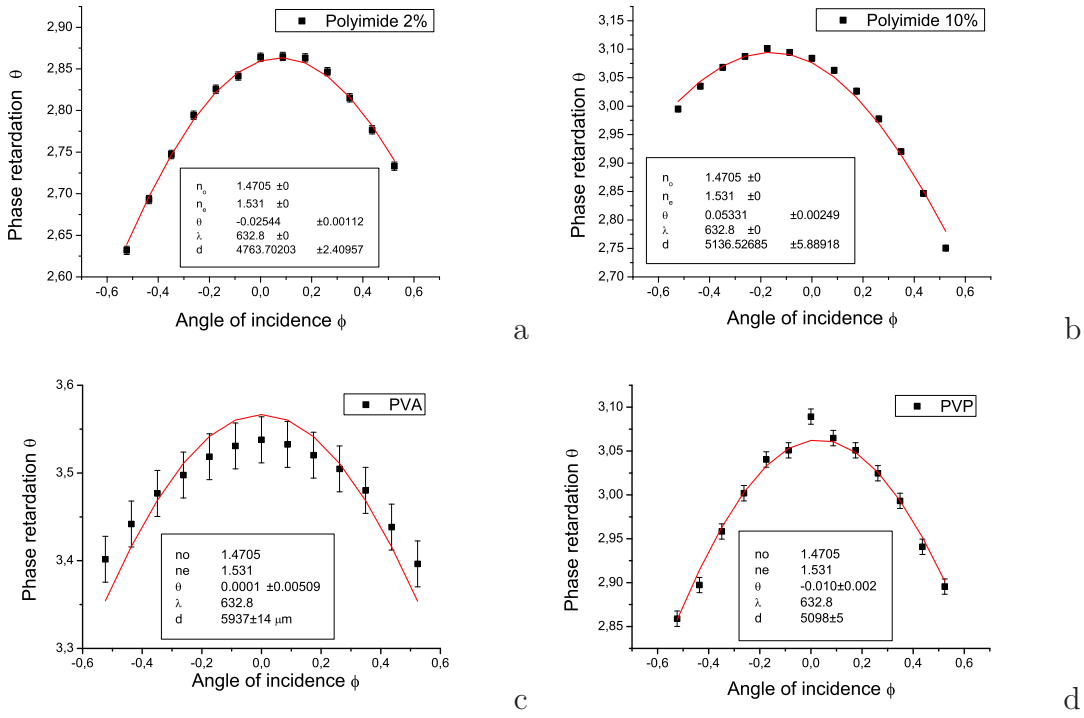

Figure 4.15: *Optical phase shift as a function of the rotation angle ϕ for cells prepared with Polyimide 2% (a), Polyimide 10% (b), PVA (c) and PVP (d).*

amplifier which measure their phase difference. This is reported in the formula below and depends on thickness (d), refraction indices (n_o, n_e), rotation angle (ϕ), tilt angle (θ).

$$\delta = \frac{2\pi d}{\lambda}\left[\frac{n_o^2 - n_e^2}{n^2}\sin\theta\cos\theta\sin\phi + \frac{n_o n_e}{n^2}\sqrt{n^2 - \sin^2\phi} - \sqrt{n_o^2 - \sin\phi}\right] \quad (4.1)$$

where $n^2 = n_o^2\cos^2\theta + n_e^2\sin^2\theta$.

In figure 4.15 is reported the optical phase shift as a function of the rotation angle ϕ for cells prepared with Polyimide 2% (a), Polyimide 10% (b), PVA (c) and PVP (d). The pretilt angle, expressed in rad, is almost zero for PVP and PVA while it is around 1° for Polyimide 2% and 3° for polyimide 10%.

We infer that a small pretilt angle allows a good accommodation of the cholesteric helix when the cell is assembled with antiparallel rubbed plates. This hypothesis is supported by the observation that when a cell with parallel rubbed plates is assembled, the cholesteric helix is not easily accommodated and a low laser emission intensity is obtained. Further investigation are currently carried out.

4.2 Lasing from cholesteric liquid crystals: tunability

As we have shown in the previous section, stability is a surmountable problem to have a proper emission from a dye doped cholesteric. On the other hand one of the main advantages to use these materials as laser sources relies on the possibilities to obtain a wide modulation of the emitted laser wavelength over almost all the visible spectrum, from ultraviolet to near-infrared.

Here we present different approaches to this issue. We have obtained tunability of the laser wavelength using materials as photosensitive nematics, photoluminescent chiral compounds and high birefringent nematics. Finally in the last section we report an innovative assembly of the liquid crystal cell that as allowed for the first time to obtain tunability of the emitted laser wavelength in a wide range, from 420nm to 790nm.

4.2.1 Cholesteric band-gap light control by using azoxy-based host materials

As we have seen in the first part the characteristics of cholesteric liquid crystals are very sensitive to external factors, such as, for example, electric and magnetic fields, temperature and if conformationally photo-active molecules are present, they can be also affected by light.

Recently, control of the selective reflection band (spiral pitch) in nemato-chiral mixtures was demonstrated when photosensitive molecules, namely nematic azoxy-based compounds, were used as the host material. Different non-photosensitive chiral materials were added to different azoxy-nematic liquid crystals and the pitch change caused by UV irradiation was investigated. A change in the pitch of 50−210nm was observed depending on the exposure time and the intensity of the light.

This effect is reversible: under illumination at wavelengths greater than 410 nm, the pitch shifts in the opposite direction. The dependence of the selective reflection band and the full-width-at-half-maximum of the band on the exposure time and the temperature dependence of the selective reflection band were investigated. The lowering of the phase transition temperature and narrowing of the width of the selective reflection band can be explained by a decrease in the orientational order parameter. The blue shift of the selective reflection band is due to a decrease in both the order parameter and the concentration of linear nematogenic molecules.

The chemical formulas of the materials used are shown in Fig. 4.16 The different azoxy-compounds used as the nematic host were:

1. p-n-ethyl-p-pentylazoxybenzene (EPAOB) with a nematic temperature range between 5oC and 40.5 °C,

2. ZhK-440 (NIOPIK) - a mixture of 2/3 p-n-butyl-p-methoxyazoxybenzene (BMAOB) and 1/3 p-nbutyl- p-heptonoiloxyazoxybenzene (BHAOB) with a nematic temperature range between $-5°C$ and 75°C.

   To investigate the dependence of photosensitivity on the concentration of the azoxy-compound, mixtures of ZhK-440 with different amounts of the non photo-isomerizable and UV/vis transparent nematic liquid crystal MLC-6815 (Merck) were prepared in the proportions 75:25%, 50:50%, and 25:75%.

3. ZhK-999, a mixture of ZhK-440 with 2 non-photoisomerizable compounds (NIOPIK) with a nematic temperature range between 0°C and 77.5°C.This mixture possesses a low dielectric relaxation time: at 20°C the dielectric anisotropy $\Delta\epsilon$ is $+2.2 \pm 0.2$ at 200 Hz and -2.1 ± 0.2 at 40 kHz.

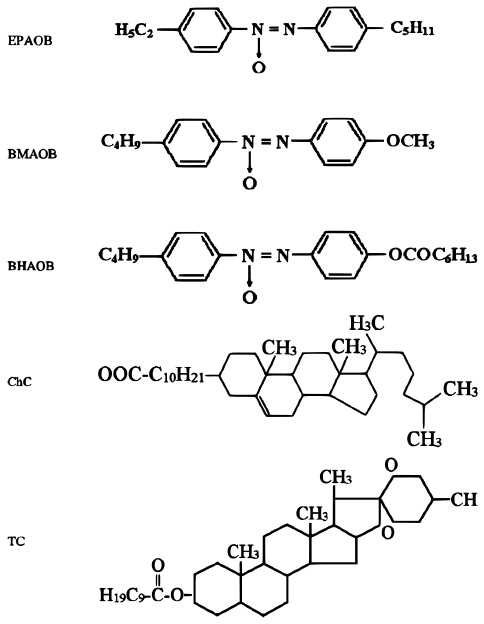

Figure 4.16: *Compounds used in this investigation*

The following chiral dopants were used:

1. MLC-6248 (2011R, Merck),

2. Cholesteryl Caprinate (ChC),

3. Tigogenin Caprate (TC) [61].

All experiments were carried out in cells of 10 μm thickness. The transmission spectra measurements were made at room temperature using a fiber-optics Avantes spectrophotometer. A 100W Mercury lamp and appropriate filters were used as the light source for illumination.

The distance from the lamp to the cell was approximately 20 cm. For investigating the trans-cis and cis-trans conversions, two types of interference filters were used, 365nm (F1) and 436nm (F2), along with two types of band pass filters, 240-390 nm (F3) and 410- 500 nm (F4). The intensity of UV light at the sample varied from 0.1 to 1 mW/cm^2 depending on the filter. The trans form of

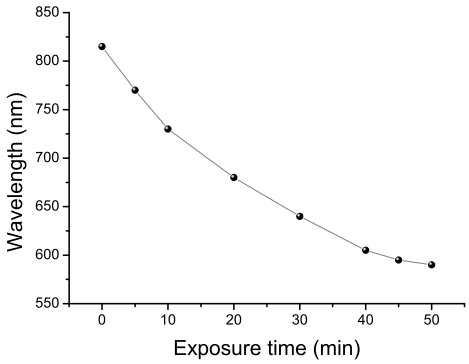

Figure 4.17: *Dependence of λ_0 for a mixture of 90% EPAOB and 10% TC on exposure time using filter F_1*

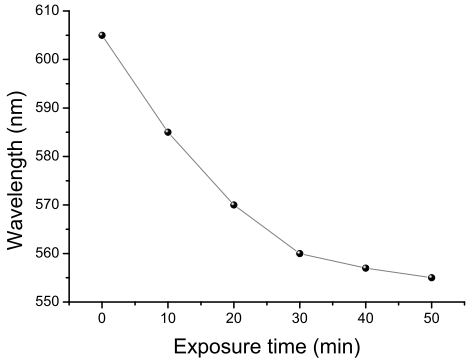

Figure 4.18: *Dependence of λ_0 for a mixture of 72% EPAOB and 28% ChC on exposure time using filter F_3*

azoxy-compounds absorbs in UV-violet region of spectrum up to about 400 nm, and as shown [62–65], the cholesteric pitch decreases with exposure to irradiation that has a wavelength between 330 and 400 nm. Thus during UV irradiation, the color of the cholesteric film changes from red to blue. This effect is reversible: the pitch returns to its initial state when the irradiating light has a wavelength greater than 410 nm.

Figs. 4.17 and 4.18 show the exposure time dependencies of the wavelength of the selective reflection peak (λ_0) for a mixture of EPAOB with TC using filter F1 or with ChC using filter F3.

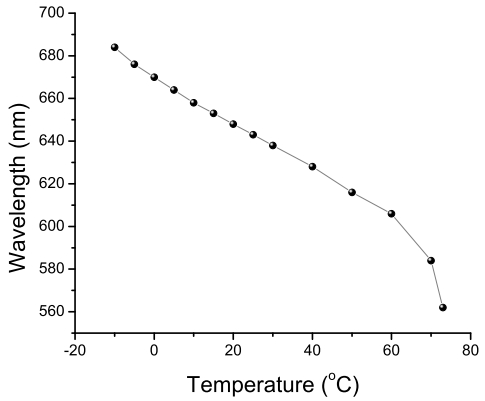

Figure 4.19: *Temperature dependence of λ_0 for a mixture of 75% ZhK-440 and 25% ZLI-2011.*

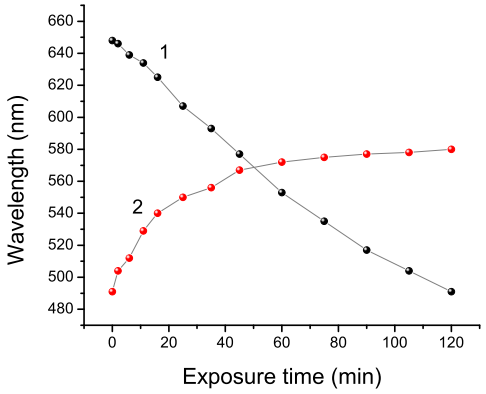

Figure 4.20: *Dependence of λ_0 for a mixture of 75% ZhK-440 and 25% ZLI-2011 on exposure time using filters F_1 (1) and F_2 (2)*

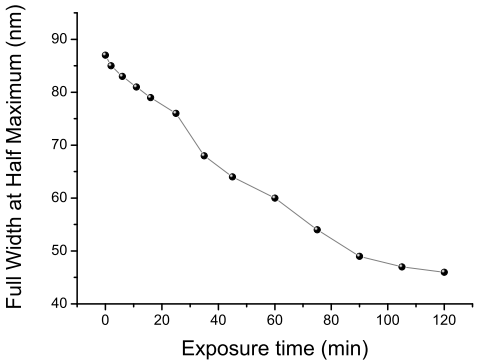

Figure 4.21: *Dependence of the full-width-at-half-maximum of the selective reflection for a mixture of 75% ZhK-440 and 25% ZLI-2011 on exposure time during UV radiation (365 nm)*

For the mixture of EPAOB and TC, the pitch shifted by 210 nm during 50 minutes of irradiation. A more detailed investigation was carried out with the mixture ZhK-440.

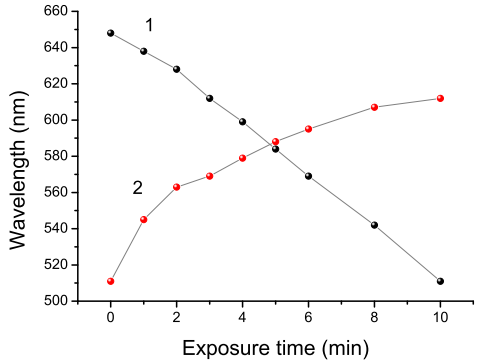

Figure 4.22: *Dependence of λ_0 for a 100% ZhK-440 sample on exposure time using filters F_3 (1) and F_4 (2).*

Figs.4.19-4.21 show the results for a mixture of 75% ZhK-440 and 25% ZLI-2011, including the dependence of λ_0 on temperature and exposure time, and the dependence of the full-width-at-half maximum of the selective reflection band on exposure time. As shown in Fig.4.20, after 120 minutes of irradiation using the interference filter, λ_0 shifted to shorter wavelengths by 160 nm.

After irradiation with 436 nm light, a shift in the opposite direction was observed due to cis-trans conversion, but not to its initial value. This indicated

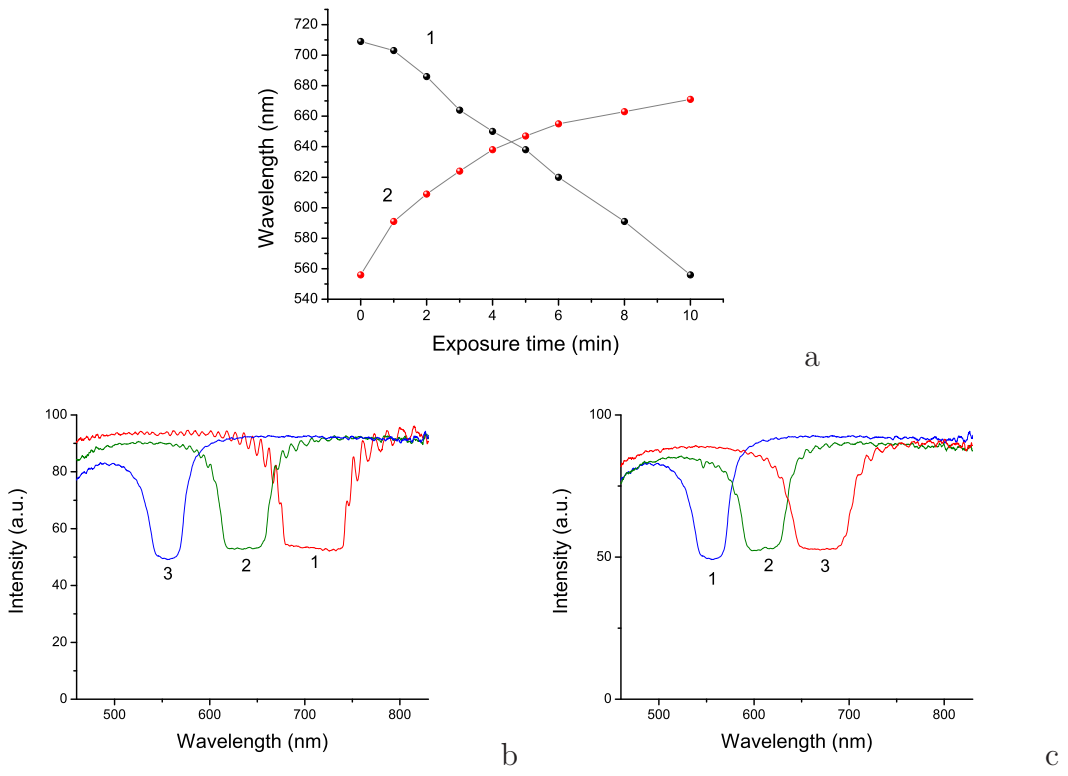

Figure 4.23: *(a) Dependence of λ_0 for a mixture of 75% (75% ZhK-440 and 25% MLC-6815) and 25% ZLI-2011 on exposure time using filters F3 (1) and F4 (2); (b) Transmission spectra for the same mixture after different exposure times using filter F3: (1) before irradiation; (2) after 5 minutes of irradiation; (3) after 10 minutes of irradiation; (c) Transmission spectra for the same mixture subsequent to UV irradiation (showing the shift of the selective reflection band in the other direction) at different exposure times using filter F4: (1) before irradiation; (2) after 2 minutes of irradiation; (3) after 10 minutes of irradiation.*

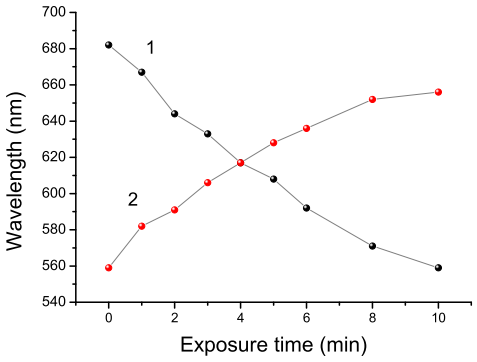

Figure 4.24: *Dependence of λ_0 for a mixture of 75% (50% ZhK-440 and 50% MLC-6815) and 25% ZLI-2011 on exposure time using filters F_3 (1) and F_4(2).*

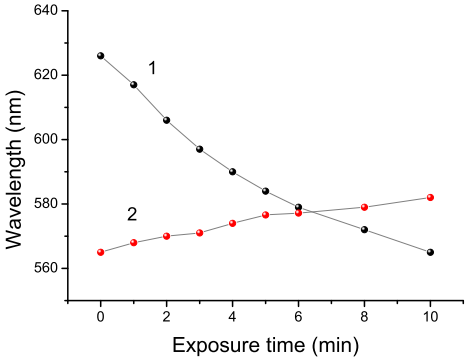

Figure 4.25: *Dependence of λ_0 for a mixture of 75%(25% ZhK440 and 75% MLC-6815) and 25% ZLI-2011 on exposure time using filters F_3 (1) and F_4 (2).*

that not all of the cis molecules transform back to the trans form. A return to the initial state was observed after waiting several days or upon re-heating to the isotropic phase. To obtain a faster shift and to understand the effect of different concentrations of azoxybenzene compounds in these CLCs, mixtures of Zhk-440 with another nematic compound were irradiated with light covering both the UV and visible ranges. The results are shown in Figs.4.22-4.25.

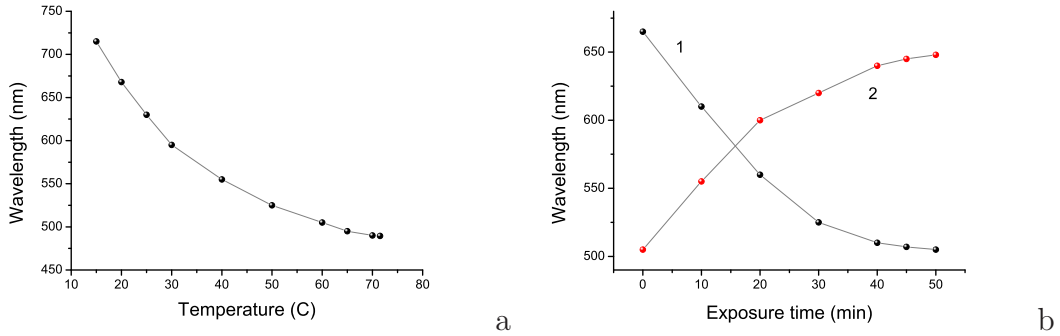

Figure 4.26: *(a) Temperature dependence of λ_0 for a mixture of 86.7% ZhK-999 and 13.3% TC; (b) Dependence of λ_0 for the same mixture on exposure time using filters F_1 (1) and F_2 (2)*

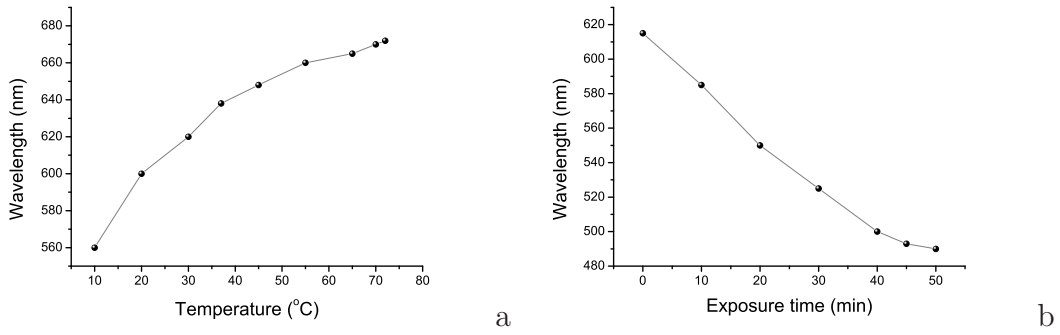

Figure 4.27: *(a) Temperature dependence of λ_0 for a mixture of 72% ZhK-999 and 28% ChC; (b) Dependence of λ_0 for the same mixture on exposure time using filter F_1.*

In the case of the broad filters and the 100% ZhK-440 sample, the blue shift was 140 nm after 10 minutes of irradiation. As it is clear from the figures, the shift of λ_0 decreased as the concentration of ZhK-440 decreased. Fig. 4.23 shows some examples of the transmission spectrum changes under irradiation. The last compound investigated was ZhK-999, which is a mixture of ZhK-440 with two

non-azoxycompounds developed as a nematic liquid crystal with a small dielectric relaxation.

TC and ChC were added to ZhK-999 and these mixtures were irradiated using different interference filters. The temperature dependence of λ_0 for these mixtures was also investigated. The results are shown in Figs.4.26 and 4.27.

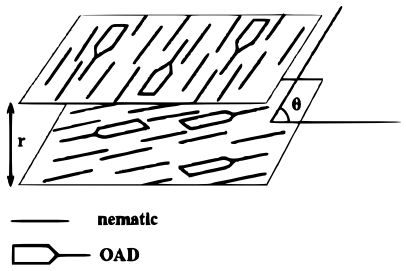

Figure 4.28: *Schematic diagram showing the arrangement of nematic and chiral dopant molecules in neighboring nematic layers of the cholesteric superstructure. The nematic and optically active dopant (OAD) molecules are depicted differently. The distance between layers is r and the angle between the directors of the two layers is θ*

Although $d\lambda_0/dT$ is negative when TC is used as the dopant and positive when the dopant is ChC, in both cases λ_0 decreases when irradiated with UV light. As a first step in understanding these results, the cholesteric structure must be considered.

It is known that the pitch in induced cholesteric systems (nematic-chiral mixtures) depends on the structure of both the nematic host and the chiral dopant [66–69]. Usually the pitch decreases with an increase of the chiral dopant concentration. The ability of the chiral dopant to torque a nematic phase into a twisted structure is called its helical twisting power, β, and is defined by the relation $\beta = (Pc)^{-1}$, where c is the dopant concentration.

Fig.4.28 shows two neighboring nematic layers in the helical arrangement of the cholesteric structure [70], where $P = 2\pi r/\theta$ (r is the distance between the two layers and θ is the angle between the preferred orientation of molecules or director in the two layers). Ref. [70] considers the influence of the stereochemistry of the optically active dopant on the pitch, i.e., on its β. It is evident that to change the pitch either r, θ, or both must change. Clearly the stereochemistry of the molecules plays an important role. The same influence of the molecular stereochemistry on the pitch applies to photoisomerizable molecules. Several factors are responsible for the influence of external fields on the pitch, among them are the variation of the orientational order parameter and the conformation

of the molecules.

A comprehensive theory explaining the behavior of CLCs at the molecular level has yet to be developed [71–74]. Regarding the control of the pitch with light illumination, in the early work of Sackmann [75], trans and cis azobenzene were added to a CLC and it was shown that λ_0 decreases linearly with an increase in the concentration of trans azobenzene and increases with an increase in the concentration of cis azobenzene. It should be noted that the CLC used by Sackman represents a compensated mixture of two cholesteryl derivatives, and the concentration dependence of various parameters for this mixture is quite complex [69]. Later it was shown that the addition of trans-azobenzene shifts the selective reflection band toward longer wavelengths, while the addition of cis-azobenzene produces the opposite change [62, 76–85]. The shift also depends on the length of the alkyl chain of the azobenzene. In careful experiments, Ruslim and Ichimura [78] found that adding unsubstituted azobenzenes to CLCs produced the opposite effect observed by Sackmann. This discrepancy was explained by noting that the temperature dependence of the pitch in the CLC needed to be taken into account. In Ref. [81], a schematic picture of the alignment of azobenzene derivatives in a CLC is included. The authors hypothesize that the trans-azobenzenes align parallel to the local director of the cholesteric molecules and therefore change the cholesteric pitch, while the cis-azobenzenes cannot align parallel to the local director due to their bent structure. It is also suggested that rod-like trans-azobenzene molecules promote the stabilization of the cholesteric phase, while the bent cis-azobenzene molecules lead to the disorganization of the orientationally ordered structure.

It must be taken into account that many substances based on azobenzene possess a nematic phase with trans isomers but only an isotropic phase with cis isomers [86, 87]. Therefore, upon irradiation with UV light, liquid crystal forming molecules are being transformed into non-liquid crystal forming molecules. Thus, cis molecules do not "participate" in the organization of the liquid crystal, and in the case of CLCs these molecules are "outside" of the molecular arrangement forming the supramolecular helical structure (as shown in the schematic picture in Ref. [81]). These cis molecules, therefore, can be considered as an "isotropic liquid dopant". Usually any isotropic achiral dopant causes an increase in the pitch. On the other hand, in induced cholesteric systems the trans-cis transformation of the isomerizable nematic host molecules leads to a lowering of the concentration of the nematic component of the mixture, resulting in a decrease of the pitch.

The results reported here along with previous investigations demonstrate that the loss of some of the liquid crystal forming molecules dominates and a decrease in the pitch is observed. Moreover, the photo-transformation simultaneously produces a change in both the polarizability and orientational order parameter of the liquid crystal molecules [88, 89]. The decrease of the order parameter produces a change of the refractive indices and a lowering of the phase transition temperature. Actually, the change of refractive indices is due to both a change in the order parameter and a change in the anisotropy of the polarizability of the molecules. The ordinary index increases and the extraordinary index decreases, leading to a decrease in the width of the selective reflection band in CLCs.

In the case of p-azoxyanizole, the decrease in the amount of orientational order causes the ordinary refractive index to increase slightly while the extraordinary refractive index decreases more [90]. So in CLCs the shift in the selective reflection band and the change of its width are due to changes in both the polarizability and the order parameter.

The behaviour of such systems depends on the concentration of cis molecules: increasing their concentration destabilizes the nematic order and in many cases the liquid crystal transforms to the isotropic phase when the concentration of cis molecules reaches a certain value.

In the experiments reported here, irradiation was stopped as soon as the transition to the isotropic phase started. Irradiation was also stopped when the selective reflection band started to shift into the absorption region of the azoxy-compounds.

In conclusion, it is demonstrated that CLC mixtures based on azoxybenzene nematic components show reversible light control of the selective reflection band with shifts as large as 210 nm. The results reported here show that trans-cis isomerization causes several competing and interdependent effects in CLCs, including on one hand, a change of the orientational order parameter, the isotropic phase transition temperature, and refractive indices, and on the other hand, a change in the concentration and shape of the molecules involved in the organization of the liquid crystal state with its helical superstructure. So although a full theoretical treatment is lacking, experiments demonstrate that the reversible control of the pitch in CLCs is a robust phenomenon and could very well be useful in a wide range of practical applications.

4.2.2 Chiral luminescent compounds for fine tuning

The possibility to use chiral luminescent dyes as promising materials for mirrorless laser application is presented in this section.

The proposed materials combine two necessary properties to achieve laser emission from dye doped cholesteric liquid crystals: chirality and luminescence. At present, dye doped CLCs contain at least three compounds: a nematic material, an optical active dopant, and a luminescent dye, that have to be carefully selected according to their properties of solubility, transparency and thermal stability. Here we envisage the possibility to use novel materials that can act at the same time as chirality promoters and luminescent compounds. Two different fluorene-based compounds one well defined trimer and an oligomer with chiral pendant chains, whose structure is depicted in figure 4.29, have been investigated.

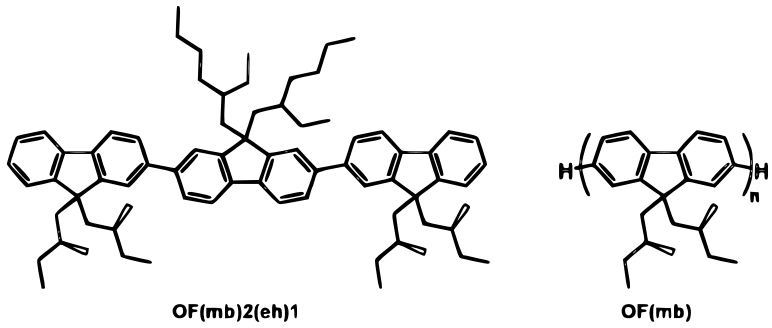

Figure 4.29: *Chemical formulas of the chiral luminescent compounds*

Oligofluorenes (OF) have been reported as very suitable blue-emitters for optical and electrooptical applications because of their good thermal and photo stability, and high emission efficiency. In addition, the facile substitution at the bridging C9 site of fluorene unit provides the possibility of controlling solubility, processability or molecular interactions both in the fundamental and excited state [91, 92].

The selected trimer OF(mb)2(eh)1 contains two chiral (S)-2-metylbutyl (mb) chains appended at the bridging C9 of the terminal fluorene units. Chen and coworkers have reported that this structural moiety gives rise to helical assemblies that can be preserved in the solid state, in special for lower oligomers that resist crystallization [93]. The trimer has also two racemic 2-ethylhexyl (eh) chains at the C9 of the central fluorene unit. The oligofluorene OF(mb) only contains chiral (S)-2-metylbutyl (mb) appended to the methylene C9 bridge. OF(mb)2(eh)1 was

prepared by a Suzuky coupling reaction of the adequate symmetrical diboronic ester of the 9,9- dialkylfluorene with the unsymmetrical monobrominated derivative of 9,9-di((S)-2-methylbutyl)fluorene in 1:2 molar ratio. OF(mb) was prepared by Ni(0)- mediated Yamamoto coupling polymerization from the corresponding dibromo monomer, and it has a relative number-average molecular weight Mn=3240 g mol^{-1} with polydispersity of around PI=1.3 according to GPC analysis against polystyrene standards. Therefore, according to the electronic spectra (see below description of the optical properties) and by comparing results from the literature, we have estimated that OF(mb) contains approximatively six fluorene units.

Luminophore	Thermal transition (°C)	λ_{abs}(nm)	λ_{em}(nm)	ϕ_{em}
OF(mb)2(eh)1	T_g: 11	351	396	0.81
OF(mb)	Ch 250 I [(a)]	370	414	0.78
[(a)] *below 250° C the compound shows a liquid crystalline phase of cholesteric type (Ch) but the glass transition (Tg) or melting (Tm) was not detected from DSC.*				

Table 4.1: Transition temperatures, absorption and emission wavelengths and quantum yields for the luminophores

Table 4.1 displays thermal properties of the investigated compounds. Thermal transition temperatures and mesophases were determined by Differential Scanning Calorimetry (DSC) using a Q2000 from TA Instruments, and Polarizing Optical Microscopy (POM) using an Olympus BH-2 polarizing microscope equipped with a Linkam THMS hot-stage central processor and a CS196 cooling system. All the samples were preheated with subsequent controlled cooling. The trimer OF(mb)2(eh)1 is an amorphous material with glass transition temperature below room temperature. The oligomer OF(mb) is semicrystalline powder that melts into a liquid crystal phase of cholesteric type as was determined by optical microscopy observations and X-ray diffraction patterns, in agreement with the description of Chen and coworkers [93]. The DSC curves do not show clear transitions, such as the glass transition, the melting or the clearing points. Nevertheless, optical microscopy inspections under cross-polarisers shows a gradual increasing of the viscosity that allows the development of characteristic textures at high temperatures, above 140-180°C. The mesophase is stable up to 250°C and transition into the isotropic liquid is accompanied by thermal decomposition of the sample, as corroborated by thermogravimetric analysis.

The optical properties of the fluorene-based luminophores were determined in diluted THF solutions. UV-vis spectra were recorded on a UV4-200 from ATI-Unicam using 10^{-4}- 10^{-5} M solutions. Emission spectra were obtained with a Perkin-Elmer LS50B spectrofluorimeter using solutions of ca. 0.01 absorbance (about 10^{-6} - 10^{-7} M) under excitation at the absorption maximum. Emission quantum yields (ϕ_{em}) were measured relative to 9,10-diphenyllanthracene (ϕ_{em} = 0.90 in cyclohexane) from corrected emission spectra.

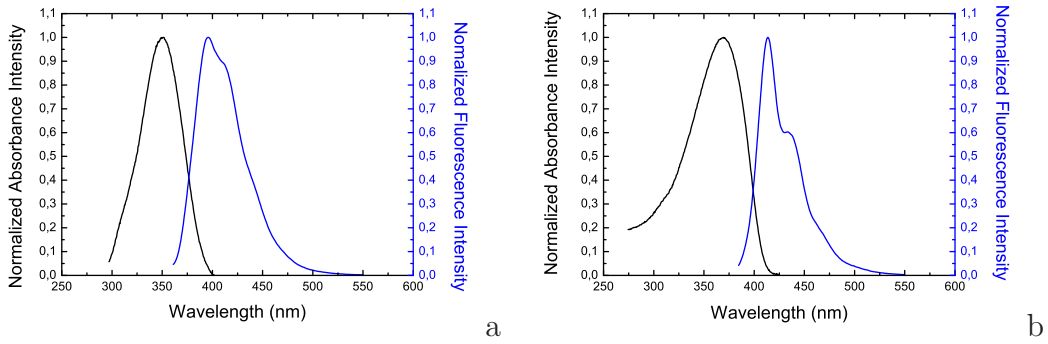

Figure 4.30: *Absorption (black) and emission (blue) spectra for (a) OF(mb)2(eh)1 and (b) OF(mb)*

In Figure 4.30 the absorption and emission spectra for (a) OF(mb)2(eh)1 and (b) OF(mb) are shown. The compounds exhibit an unresolved absorption band due to the $\pi - \pi*$ transition that it is red shifted for OF(mb). The selected chiral luminescent dyes are efficient emitters with emission quantum yields around 0.8 in the violet-blue range with a maximum between 396 and 414 nm. The absorption and emission wavelengths are related to the conjugation length, and the number or type of the pendant chains do not significantly alter them in solution. For our measurements we have used conventional chiral nematic mixtures and we have shown how the presented novel materials are able to twist or to untwist the cholesteric helix, maintaining at the same time good luminescent properties. For chiral nematic mixtures MLC-6815 and MLC-6816 were used as UV transparent nematic compounds and MLC-6247 and MLC-6248, as respectively left-handed and righthanded optically active dopants.

All the materials were supplied by Merck (Darmstadt, Germany). Different concentrations of the luminescent materials were added to the cholesteric mixtures in order to finely tune the photonic band gap. Mixtures were confined in 40 μm thick cells, made by two glass plates separated by mylar spacers. The plates

were coated with rubbed polyvinylalcohol (PVA) in order to obtain an homogeneous planar alignment of the CLC film. The transmission spectra of cholesteric mixtures were investigated for the pure cholesteric and for dye doped mixtures, fig.4.31 shows the transmission spectra of the cholesteric mixture and the shift of the photonic band gap when different concentrations of luminescent dye are doped to the cholesteric.

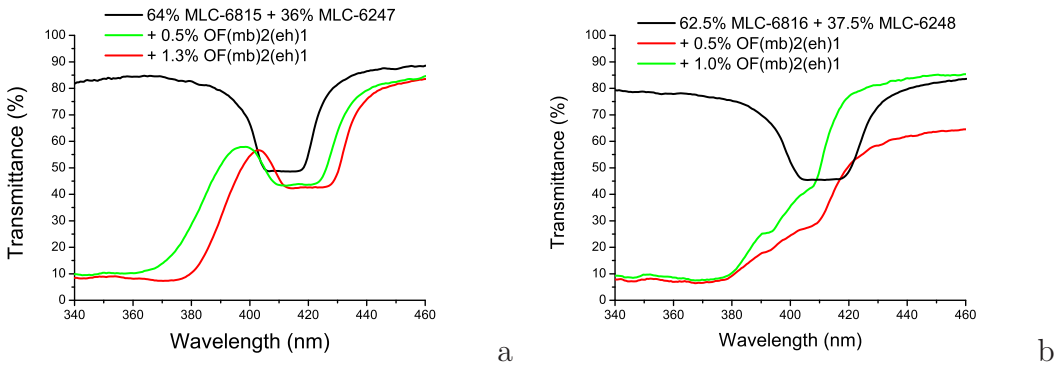

Figure 4.31: *(a)Transmission spectra for the cholesteric mixture 64% MLC-6816 + 36% MLC-6247 (black curve) and the mixture doped with 0.5% of OF(mb)2(eh)1 (green curve) and 1.3% of OF(mb)2(eh)1 (red curve).(b) Transmission spectra for the cholesteric mixture 62.5% MLC-6816 + 37.5% MLC-6248 (black curve) and doped with 0.5% OF(mb)(red curve) and 1.0% OF(mb)(green curve).*

In particular fig. 4.31(a) shows the variation in the photonic band gap when a small amount of chiral luminescent dye, respectively 0.5wt% (green curve) or 1.3wt% of OF(mb)2(eh)1 (red curve), is added to the cholesteric mixture 64% MLC-6815 + 36% MLC-6247 (black curve). The cholesteric mixture, prepared using MLC-6247 is left handed, since we had a red shift in the photonic band gap, we can conclude the chirality of the luminescent dye is right handed. 1.3% of OF(mb)2(eh)1, the limit amount before dye precipitation, causes a 30 nm shift, adding the same amount to the right handed chiral compound MLC 6248 the shift is 13 nm (fig.4.31b). This behavior can be explained considering that is less difficult to unwind an helix than increasing its torsion.

The handedness of OF(mb) is the same as OF(mb)2(eh)1 (Fig.4.32 a). Adding 1% of OF(mb) causes a shift in the stop band of the cholesteric mixture 62% MLC-6816 + 38% MLC-6247 and a shift in the long wavelength edge of the selective reflection band of about 25 nm when added to a left handed chiral mixture and of about 10 nm when added to a right handed chiral mixture(fig.4.32 b).

The laser emission was observed mainly at the long wavelength edge of the

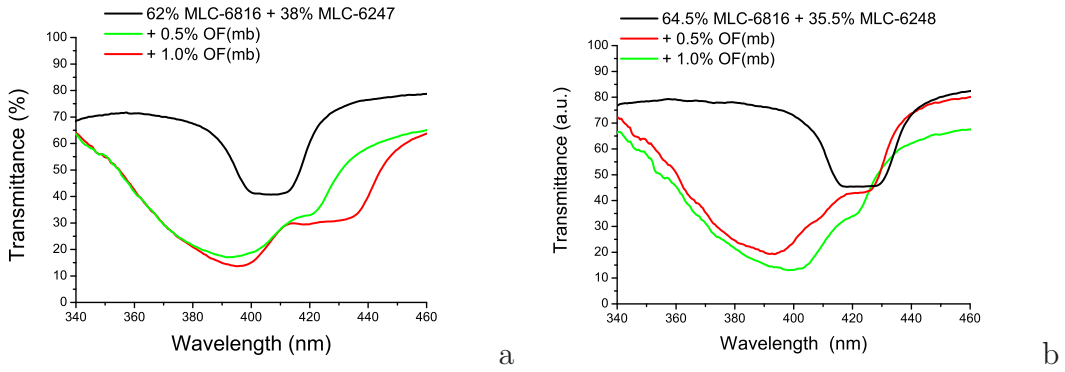

Figure 4.32: *(a)Transmission spectra for the cholesteric mixture 62% MLC-6816 + 38% MLC-6247 (black curve) and the mixture doped with 0.5% of OF(mb)2(eh)1 (green curve) and 1.0% of OF(mb)2(eh)1 (red curve). Transmission spectra for the cholesteric mixture 64.5% MLC-6816 + 35.5% MLC-6248 (black curve)and doped with 0.5% OF(mb) (red curve) and 1.0% OF(mb)(green curve)(b).*

selective reflection band, and can be explained on the basis of the influence of the selective reflection band on the fluorescence characteristic of dyes [94–96].

Investigations on photoexcitation have been performed using as a source a nitrogen laser, Model VSL-337ND-S. The pulse wavelength, width, and repetition rate were 337 nm, 4 ns, and 1-10 Hz, respectively. The laser beam was focused by a lens f = 10 cm to reduce the spot size onto the cell to few hundreds of micrometers. The pump beam hit the sample at 45° with respect to the cell normal, a usual experimental geometry for this kind of experiment (as depicted in fig 4.10).

An optical fiber coupled to the spectrometer Avantes Fiberoptics Model: AVASPEC-2048, with 1.4 nm resolution, collected the light emitted from the sample. Laser emission from different mixtures was obtained and fig. 4.33 shows the typical laser spot.

In figure 4.34 we report the lasing spectra of the left handed dye doped cholesteric mixtures, containing respectively (a) OF(mb)2(eh)1 and (b) OF(mb) while in fig.4.35 we report the lasing spectra for the right handed cholesteric mixtures containing respectively (a) OF(mb)2(eh)1 and (b) OF(mb), pumped with an energy of 2μJ.

In all cases the laser emission is slightly more efficient for mixtures containing a smaller amount of chiral luminescent dopant (red curve). This new class of materials possessing both chiral and luminescence properties could be very promising for laser applications. Further optimizations can improve their perfor-

Figure 4.33: *Spot of the laser emitted from the CLC cell on a screen placed at 10cm.*

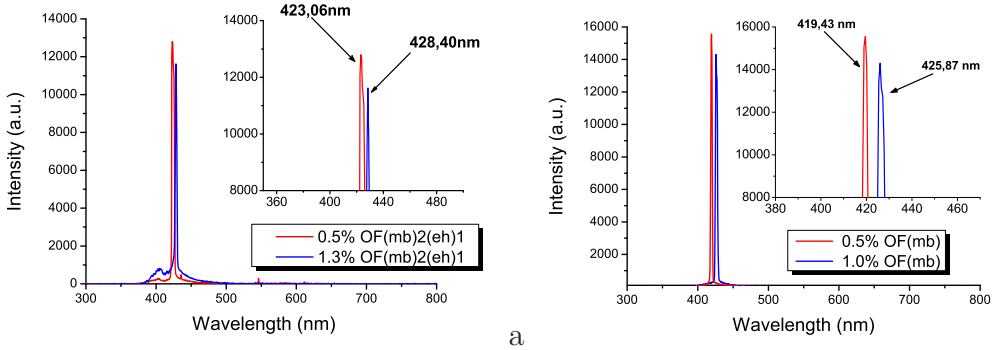

Figure 4.34: *Lasing from the left handed cholesteric mixtures doped with (a) 0.5% or 1.3% of OF(mb)2(eh)1 and (b) 0.5% or 1% of OF(mb).*

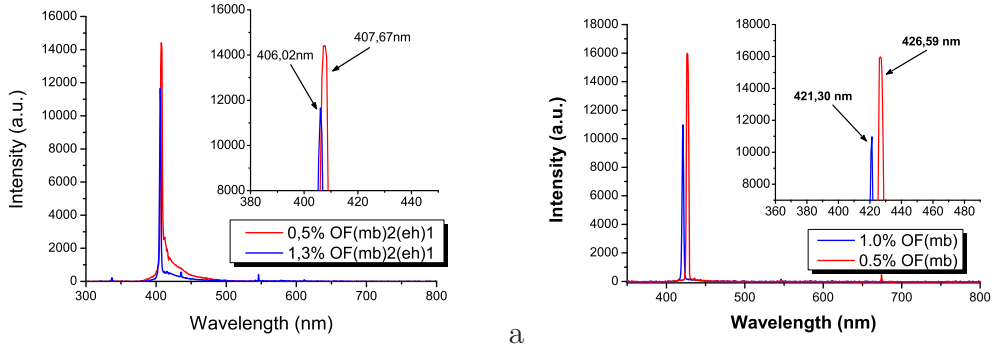

Figure 4.35: *Lasing from the right handed cholesteric mixtures doped with (a) 0.5% or 1.0% of OF(mb)2(eh)1 and (b) 0.5% or 1% of OF(mb).*

mances. In particular they could be designed to have a stronger helical twisting power, or to contain photosensitive moieties that can change conformation under light exposure. Finally changing the chromophore could be possible to have emission in different ranges of the optical spectrum.

4.2.3 Wide-band gap materials as new tuning strategy

A new tuning strategy for mirror-less liquid crystals laser consisting in a three layer cell with two cholesteric layers sandwiching an isotropic mixture of a photoluminescent dye is shown in this section. One of the chiral layers contains a wide band gap material while the second layer consists of a series of small band gap materials. Through the combination of these two layers, a series of mirrors that can selectively reflect different wavelengths is obtained.

Two new strategies were used to finely tune the laser emission and to widen the range of the emitted wavelengths (420 nm - 790 nm) using a multilayer system. The multilayer system consists in two separate cholesteric layers sandwiching a mixture containing a luminophore, which can also be not soluble in liquid crystals. The novelty of this system relies in the materials used for the cholesteric liquid crystal layers. One cholesteric layer contains a high birefringent nematic material and shows a wide photonic band gap. For the other cholesteric layer two different solutions are investigated: a mixture containing a photosensitive chiral compound and a mixture containing a common chiral dopant.

For the experiments both commercial and specially prepared materials were used. To obtain the wide photonic band gap layer, BL-006 or alternatively BL-090, with Δn approximately 0.3, as nematic compounds and MLC-6248 as optically active dopant were used. To prepare the second cholesteric layer, MLC-6816 as nematic compound, ZLI-3786 as photosensitive chiral compound and RM-257 as photo-polymer (all the above materials supplied by Merck) and the Irgacure 2100 (Ciba) as photoiniziator were used. As isotropic solvent glycerol was used and as luminescent commercial dyes ADS680HO and Rodhamine 6G, and a specially prepared luminophore were used.

As we have seen previously if the dye is not soluble in liquid crystals, the usual cell geometry can not be used. The sandwich cell was assembled as shown in Fig. 4.36, and it was composed by a first cholesteric layer containing a material with a well defined pitch and a second cholesteric layer containing chiral materials with different pitches.

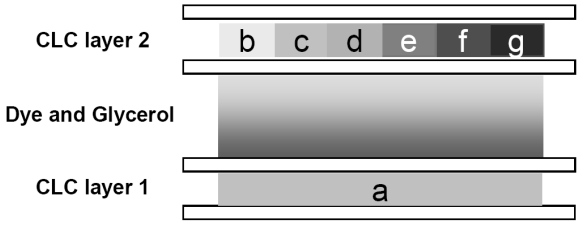

Figure 4.36: *Sketch of the sandwich cell.*

The mixture containing dye and glycerol was sealed in a 1 mm central glass cell while the two cholesteric mixtures were sandwiched between two glass and quartz plates coated with rubbed PVA (polyvinyl alcohol) to obtain a homogeneous alignment of the CLC layers. The thickness of the two cholesteric layers was 5 μm.

In order to tune the laser emission, two different strategies were exploited, the first one is based on the photo-transformation properties of the chiral compound ZLI-3786.

The chemical structure of this material is identical to the one of ZLI-811 (Merck) except that they are optical antipodes [97], i.e. they possess a different handedness. ZLI-3786, like ZLI-811 [98, 99], undergoes a photo-transformation if irradiated at wavelengths shorter than 300 nm. This transformation is a photo-Fries rearrangement, which is a well known phenomenon for aromatic esters. Its occurrence is revealed by the effect produced on the cholesteric helical pitch, which changes with the exposure time. To create a pitch gradient within the CLC layer containing ZLI-3786, distinct regions of the layer were exposed to UV for different times using a customized mask.4.37

The addition to the mixture of a photopolymer and a photoiniziator was needed to stabilize the cholesteric structure. The used illumination times were from 1 up to 5 minutes, to have photonic band gap varying continuously within the second cholesteric layer band gap.

Figure 4.38(red curve) shows the transmission spectrum for the mixture contained in the second cholesteric layer 99%[78% MLC-6816 + 22% ZLI-3786] + 1%[99% RM-257 + 1% Irgacure 2100]. On illuminating the second cell with a 100W mercury lamp, a process that results in a stable shift of the selective reflection peak was induced. Fig. 4.38 shows the transmission spectra of the mixture when it is irradiated for 1 min (green), 2 min (blue), 3 min (magenta),

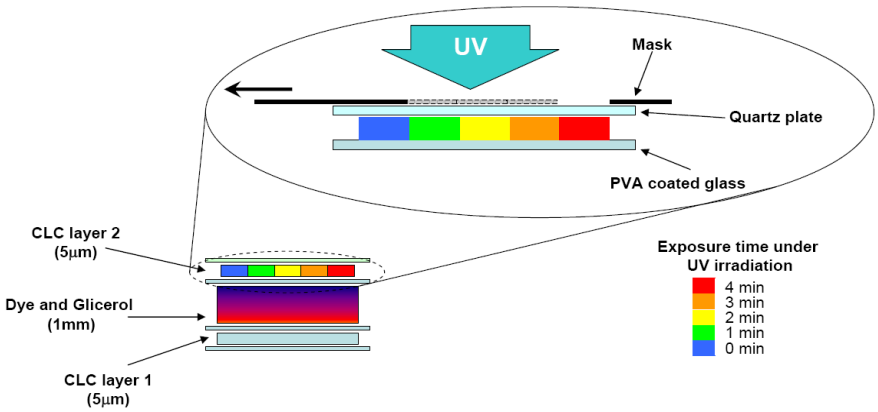

Figure 4.37: *Sketch of the creation of the pitch gradient by UV illumination for different times.*

4 min (orange) and 5 min (brown) respectively. The band gap shifts towards longer wavelengths with increasing exposure time, more than 100nm, indicating an elongation of the helix.

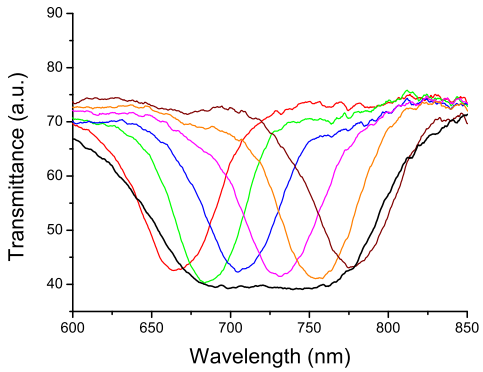

Figure 4.38: *Transmission spectra of the wide band gap cholesteric (black curve) 78% BL-006 + 22% MLC-6248 and of the small band gap cholesterics (red curve) obtained illuminating with a UV lamp different regions of a 99% [78% MLC-6816 + 22% ZLI-3786] + 1% [99% RM-257 +1% Irgacure 2100] mixture for 1 minute (green), 2 min (blue), 3 min (magenta), 4 min (orange) and 5 min (brown).*

As first cholesteric layer the following mixture was used: 78% BL-006 + 22% MLC-6248. The transmission spectrum of the wide band gap material is shown in Fig.4.38(black curve), the gap width is about 150nm.

Therefore we had a series of very narrow reflective bands from one side of the cell containing the luminescent dye and a wide photonic band-gap from the

opposite side (Fig. 4.37 and 4.38). Depending on the position of the pumping beam on the cell, one of the small band gap materials was selected. The dye emitted photons, whose wavelength was in the narrow range where the wide band gap and the selected smaller one overlap, underwent in optical resonance giving rise to a lasing effect.

In order to test the laser tuning, the cell was placed on a translation stage and the sample was moved in the plane orthogonal to the pumping laser beam. The emitted laser beam from different regions of the sandwich cell was then investigated, the different laser wavelengths are shown in Fig. 4.39.

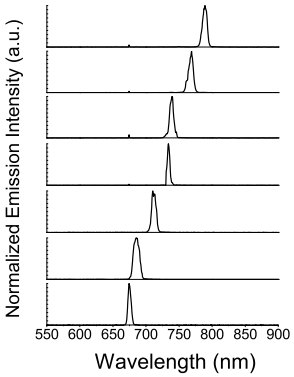

Figure 4.39: *Laser emission in the near infrared range from 675 nm to 790 nm.*

Using a dye not soluble in liquid crystals, a laser emission in the near infrared at 790 nm was observed for the first time.

In order to cover all the visible range, using this new tuning strategy, different dyes were used, in figures 4.40(a) and (b) are shown the transmission spectra and laser peaks for the Rodhamine 6G.

The second strategy to obtain the modulation of the photonic band gap position of the second chiral layer relies on the use of a series of CLC mixtures in which the chiral compound concentration changes. Three mixtures with different concentrations of the optically active dopant were prepared: 90.5% MLC-6816 + 9.5% ZLI-4572, 89.5% MLC-6816 + 10.5% ZLI-4572, 89% MLC-6816 + 11% ZLI-4572. Their transmission spectra are shown in Fig. 4.41 red, green and blue curves respectively.

The cell were partially filled, by capillarity, with one of the three mixtures; filling was then completed using in sequence the other two mixtures. After assembly, different wavelengths of the visible range were selectively reflected by the

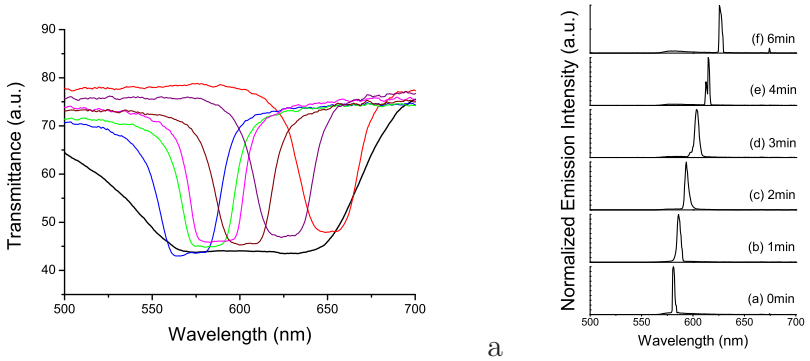

a b

Figure 4.40: *(a)Transmission spectra of the wide band gap cholesteric (black curve) 75% BL-006 + 25% MLC-6248 and of the small band gap cholesterics (blue curve) obtained illuminating with a UV lamp different regions of a 99% [74% MLC-6816 + 26% ZLI-3786] + 1% [99% RM-257 +1% Irgacure 2100] mixture for 1 minute (green), 2 min (magenta), 3 min (brown), 4 min (violet) and 5 min (brown). (b) Laser emission and tuning, for Rodhamine 6G.*

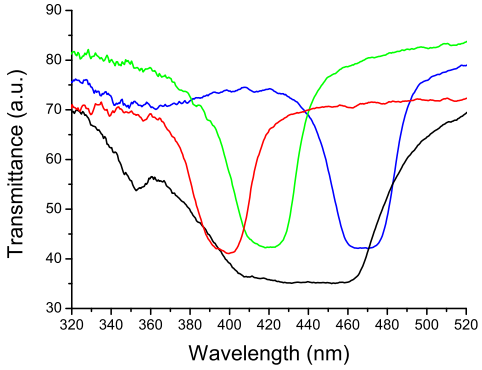

Figure 4.41: *Transmission spectra of the wide band gap cholesteric (black curve) 69,5% BL-090 + 31,5% MLC-6248 and of the small band gap cholesterics obtained using different chiral dopant concentrations (red) 90.5% MLC-6816 + 9.5% ZLI-4572, (green) 89.5% MLC-6816 + 10.5% ZLI-4572, (blue) 89% MLC-6816 + 11% ZLI-4572*

whole system. In this cell as first cholesteric layer the following mixture was used: 69.5% BL-090 + 31.5% MLC-6248. The transmission spectrum of the wide band gap material is shown in Fig. 4.41(black curve), the gap width is about 100 nm. As previously described, the combination of the two cholesteric cells, creates a set of mirrors in the overlapped regions (Fig. 4.41).

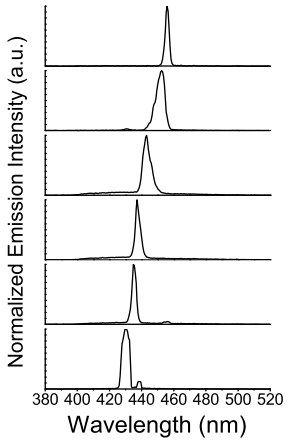

Figure 4.42: *Laser emission in the ultraviolet range from 430 nm to 460 nm*

As luminescent material we used the specially prepared luminophore OF(mb). OF(mb) is an oligomer with chiral 2-(S)-methylbutyl pendant chains. This particular luminophore was chosen as oligofluorenes (OF) have been reported to be very suitable blue-emitters for optical and electro-optical applications due to their good thermal stability and photostability, and high emission efficiency. OF(mb) was dissolved in glycerol. Again the assembled cell was shifted laterally with respect to the incoming pumping beam, the tuning of laser emission from 430 to 460 nm was observed (Fig. 4.42).

Assembling properly a set of such sandwich cells, a wide tuning of the laser emitted wavelength (from 420nm to 790nm). With a proper dye, longer laser emission wavelengths could be achieved that would be optimal for applications in biomedicine and cosmetics.

4.3 Lasing from an intermediate liquid crystal phase

We have investigate the possibility to obtain lasing in an intermediate LC phase (I) between cholesteric and smectic A phase. In an induced cholesteric system, as the mixture of a nematic LC and a chiral non-mesomorphic or mesomorphic dopant, [100, 101] if a smectogenic substance is used as a nematic host, one observes the typical picture of pre-transitional phenomena: [102] Due to the effect of helix divergence near the cholesteric to smectic A phase transition, the pitch increases with decreasing temperature. In the spirit of the de Gennes theory, near the phase transition from cholesteric to smectic A, an intermediate phase, called the "twist grain boundary" (TGB), was predicted in Ref. [103]. This complex "defect" phase is the frustrated phase derived from chiral molecules and stabilized by screw dislocations. [104]

The pre-transitional I phase was observed in chiral systems with three components: Two nematogenic LCs with different phase sequences (one with smectic A phase and another with smectic C phase) and an optically active non-mesomorphic dopant. [105, 106] In this work, we investigate a ternary system [105] made by two nematics:

- 4-cyano-4'-n-octylbiphenyl (8CB, Merck, Darmstadt)
- 4-n-octyloxybenzoate (HOPOOB, NIOPIK, Moscow)
- tigogenin caprate (TC) [102] as chiral dopant.

TC was synthesized from natural product tigogenin (Institute of Pharmaco-Chemistry, Academy of Sciences of Georgia). The mixture 82% in weight of (80% 8CB + 20% HOPOOB)+18% in weight of TC exhibits the cholesteric phase in the range of $43.8 - 47.7°C$ and the intermediate I phase between cholesteric and smectic A phase in the range of $41.6 - 43.8$°C.

Figure 1 shows the temperature dependence on the wavelength of the Bragg peak λ_B. Spectroscopic measurements by using non polarized light show that in a cholesteric phase the transmitted light intensity is about 50% of the impinging light. But in the temperature interval corresponding to the intermediate I phase, where λ_B does not depend on temperature, an unusually low intensity of transmitted light ($\sim 20\%$ of incident light) is observed [105] even if the investigation of circular polarization shows that this phase transmits and reflects both

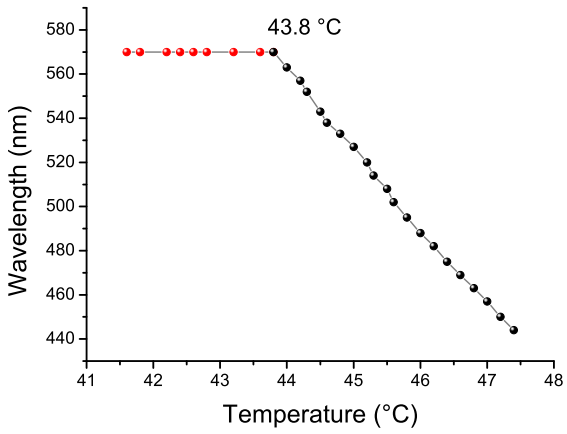

Figure 4.43: *Temperature dependence of the transmission peak wavelength λ_B, the mixture exhibits the cholesteric phase in the range 43.8-47.4 °C (red spheres) and the intermediate I phase between cholesteric and smectic A phase in the range 41.6-43.8 °C (black spheres)*

the right and left-handed circularly polarized light. [105] This indicates that the intermediate I phase is chiral. Calorimetric investigations gave evidence that the intermediate state is a separated mesophase [107]. X-ray investigations pointed out that this phase has a layered structure with a layer spacing of 33 Å, which compares with the spacing of the S_A phase [107]. All of these results suggest that this pre-transitional phase could be a TGB phase. However the texture, the pitch dependence on temperature and the behavior in an electric field [105, 106] are different from what is observed in a conventional TGB phase.

The explanation of both the right and left circularly polarized light reflection can be found in biological structures. The wings of the rare kind of beetles Plusoitis resplendens have a layered structure: between layers with a cholesteric-like structure, possessing the same handedness, a layer with unidirectional orientation of fibrils, owning half-wave $\lambda/2$ plate properties, is arranged [108]. This type of structure reflects both right and left circularly polarized light. It is interesting to note that recently a similar structure was proposed in Ref. [109] to realize a defect mode lasing in polymeric CLC.

This experimental work demonstrates the possibility to obtain a lasing effect in the intermediate I phase. To achieve this purpose, we doped this three-component mixture with the luminescent dye 4-dicyanomethylene-2-methyl-6-(p-dimethylaminostyryl)-4H-pyran (DCM from Exciton). The concentration of the

dye was 0.5wt%, which changed very slightly the original selective reflection characteristics. A 40 μm thick cell was made by two glass plates coated with rubbed polyimide (LQ1800 from Hitachi) in order to obtain a planar alignment of the CLC film. A conventional violet light-emitting diode (LED) with an emission peak at 405 nm was used for fluorescence measurements.

To observe laser emission the usual experimental geometry, previously described, was used.

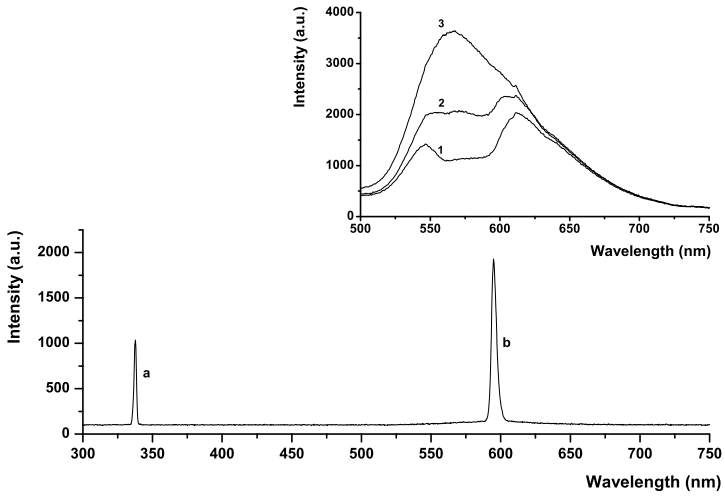

Figure 4.44: *Luminescence spectra in the intermediate I (1), cholesteric (2), and isotropic (3) phases at temperatures of 42 °C, 44 °C, and 50 °C, respectively (upper graph). In the lower graph, the peaks of laser generation from the intermediate I phase (b) and pump beam (a) are shown.*

As shown on the top of Fig. 2, luminescence spectra, obtained by LED illumination, were acquired in the isotropic phase (3), in the cholesteric phase (2) close to the intermediate I phase transition and in the intermediate I phase (1). The suppression of luminescence is larger in the intermediate I phase than in the cholesteric phase.

The lasing effect in the I phase has been checked at 42 °C. As shown on the bottom of Fig. 4.44, the lasing was observed at the long-wavelength edge of the selective reflection band. This is the first report of mirrorless lasing in an intermediate phase between cholesteric and smectic A. Regarding the structure of the I phase, we can consider the mosaic structure of the cholesteric phase, though it is also possible a TGB phase formation as suggested by the calorimetric and

x-ray measurements [107]. After further considerations, we do not exclude that the I phase could be similar to the structural composition used in Ref. [109], where a nematic layer, owning phase retarder properties, is arranged between two cholesteric layers with the same handedness. In our case, instead of nematic layers, smectic A layers oriented normal to the cell surfaces, and thus with director parallel to surfaces, could exist.

A further possibility is that a smectic A layer is sandwiched between two TGB layers. The peculiar structural properties of the I-phase are still under investigation, but the lasing effect from this anomalous nonhomogeneous chiral structure is a relevant example of defect mode lasing.

4.4 Devices

All the research carried out during these years was finally combined in the realization of a real device, that gave the possibility to obtain different laser wavelengths using one pumping source.

Combining the miniaturization of the liquid crystal cells with the fiber optics technology the developed prototype is portable and easy to handle (fig. 4.45), allowing also an easy addressing of the laser beams.

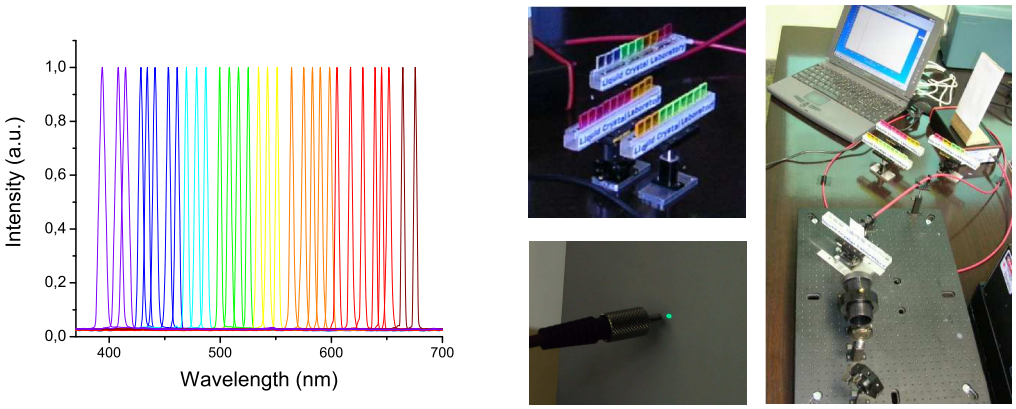

Figure 4.45: *Fine tuning of the laser emitted wavelength in all the visible range(left) and pictures of the first prototype (right).*

As we have seen so far, in the previous sections of this chapter, the problem of stability is the major drawback of these systems limiting considerably their technological applications. The movement of the entire liquid crystal cell allowed to increase duration in time of our devices (fig.4.46).

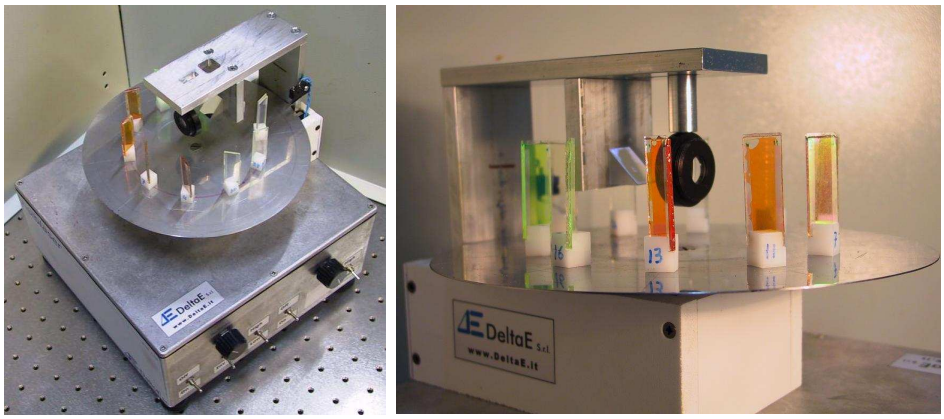

Figure 4.46: *Pictures of the second prototype (Visiblaser).*

The optimization of the devices is still going on in order to obtain finally a device usable as a light source for spectroscopy or medical investigations. The new three layered system (fig.4.36), shown in the previous sections 4.2.3, is going to be implemented in a new device capable to give a tuning of the laser emitted wavelength from 420 to 790 nm. In the figure 4.47 are pictured the cells the should be part of the new device.

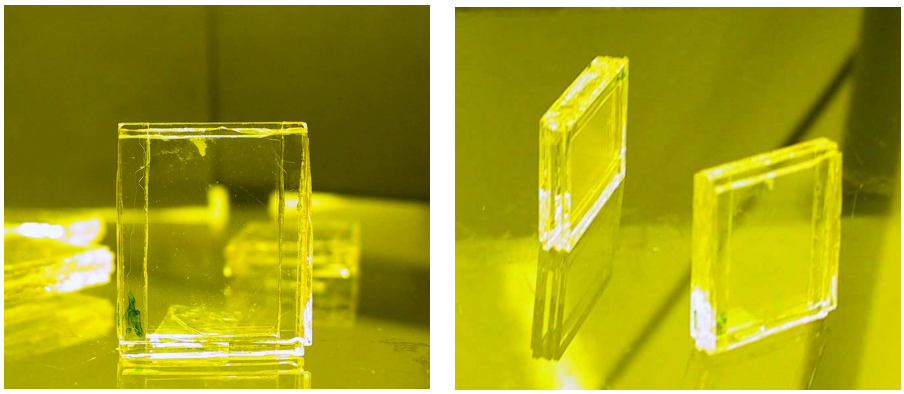

Figure 4.47: *Pictures of the three layered cell.*

Chapter 5

Cholesteric elastomers for tunable laser

As we have seen so far, since a periodical structure is essential in order to obtain mirror-less laser emission, cholesteric elastomers can be considered to play the role resonators.

Schmidtke et al. have demonstrated laser emission from a dye-doped cholesteric liquid crystal elastomer where the helical pitch was easily and reversibly modified by biaxial deformation of the elastomer itself [110]. In this method, the biaxial deformation results in a contraction of the helical pitch, by which the photonic band gap and the laser emission wavelength blue-shifted.

In our work, mechanical tunability of the photonic band gap, hence the structural evolution of the cholesteric pitch, was studied under uniaxial stretching conditions. We have used cholesteric liquid crystal elastomers to have a tunable laser device, fabricating a three-layer-structure (CLC-active medium-CLC). In this configuration, the active medium can be interpreted as a defect structure in the whole cholesteric system (4.1.2).

Moreover, the laser emission from this system is expected to occur with lower threshold energy than from a dye-doped single cholesteric medium [111].

In the following we will describe the experimental procedure necessary to prepare the cholesteric elastomers, the mechanical support and the active layer, then we will show the results of the optical characterization of the samples and the tuning of the laser emission.

5.1 Experimental procedure

The purpose of our experiments is to obtain a cholesteric liquid crystal elastomer, that can be used like a passive selective reflector for the creation of a resonator. Actually the major problem working with elastomers and in general with polymer liquid crystals is to obtain a well aligned film with the presence of large domains. Many different techniques related to the synthesis of these materials were developed during the years, here we focus on two of them. The first part of this work was mainly devoted to the preparation of a "monodomain" of CLC elastomer, while the second part was dedicated to the study of the photonic behavior of the elastomers.

5.1.1 Samples preparation

Two different cholesteric elastomers were synthesized using two different techniques and two different kinds of cross-linking compounds [38, 112]. In both cases the main compound used was a syloxane derivative:

- polymethylhydrosyloxane ($Mw = 60g/mol$)

its molecular formula is shown in fig. 5.1. The other components were attached to

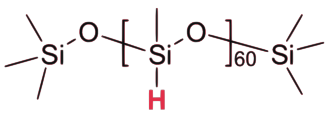

Figure 5.1: *Molecular formula of the polymethylhydrosyloxane*

this backbone by chemical reaction according to the following molar percentages

$$90\%\{80\%Nematic + 20\%Chiral - dopant\} + 10\%Cross - linker. \qquad (5.1)$$

It must be noticed that all the active sites of the backbone chain must be occupied by the other molecules interested in the reaction, i.e.

$$Backbone : Mixture = 1 : 1.$$

It is possible to change the concentrations of all the components, for example this is very important for the concentration of the chiral compound which deter-

mines the pitch length and consequently the reflected wavelengths. The following monomers were synthesized in order to prepare the CLC polymers:

- 4-pentylphenyl-4'-(4-butenoxy)benzoate ($Mw = 298g/mol$)
- Cholesterol pentenoate ($Mw = 468g/mol$).

They were designed as nematic unit and chiral dopant respectively. The nematic component was synthesized following some steps:

1. Williamson etherification
2. hydrolysis and acidification
3. esterification

as depicted in figure 5.2.

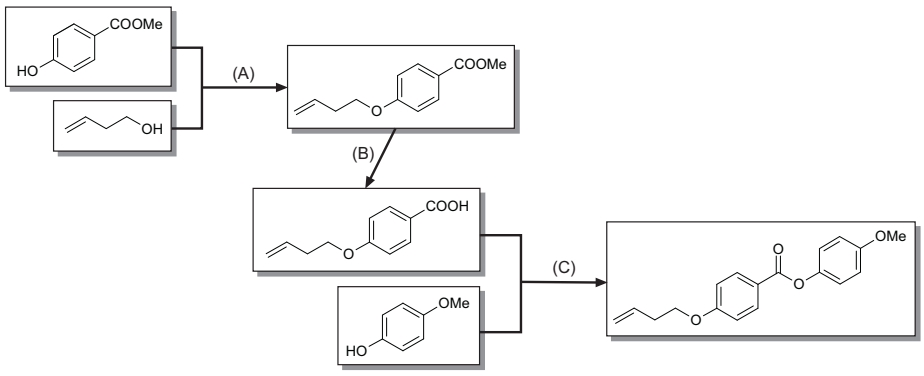

Figure 5.2: *Reaction scheme for 4-pentylphenyl-4'-(4-butenoxy)benzoate (A)* ***Williamson etherification****, (B)* ***hydrolysis and acidification****, (C)* ***esterification.***

The chiral dopant was synthesized starting from the cholesterol and elongating the active tale, as described in fig 5.3

Finally the last necessary component to prepare the CLC elastomers is the cross-linker, to perform our reactions we have used two of them:

- 1,4-di(undeceneoxy-benzene)
- 3-methyl-3-oxetane-(11-undecene-methenether)

The first is a thermal cross-linker, while the second is a UV reactive cross-linker, the molecular formula is drawn in fig. 5.4

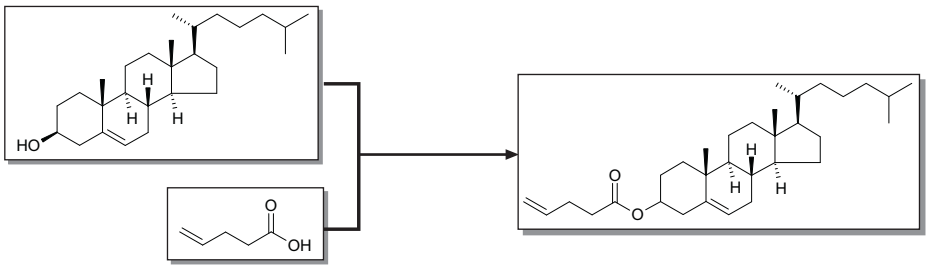

Figure 5.3: *Reaction scheme for cholesterol pentenoate*

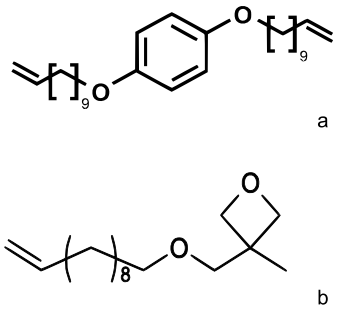

Figure 5.4: *Molecular formulas of the two cross-linkers: 1,4-di(undeceneoxy-benzene) (a) and 3-methyl-3-oxetane-(11-undecene-methenether) (b)*

5.1.2 Thermal synthesis of the CLC elastomer

The first procedure, used to synthesize and obtain elastomeric films, is the one proposed by Finkelman et alt. [113], known as anisotropic deswelling. According to this technique the synthesis was carried out as follows. All the components were mixed together (5.1) with 60μl of catalyst (COD = 1,5 Cyclooctadiene), 1ml of dichloromethane (DCM) and 13ml of toluene, using the thermal cross-linker. The whole mixture was then placed in a reactor, with a diameter of 5cm and 1cm in height. In order to avoid tack between the elastomer and the reactor, the inner wall of the reactor was covered with a PTFE (Polytetrafluoroethylene) film. Finally the reactor was fixed in a centrifuge setting the parameters of the centrifugation at 80 °C and 8500 rpm. After 45 min the chemical reaction had taken place and the result was a prepolymer similar to a gel. Thereafter the temperature of the centrifuge was diminished at 60 °C, the reactor lead was replaced with a pierced one in order to promote the solvent evaporation and the starting of the deswelling reaction. This second step was carried on for 4 hours to obtain a complete evaporation of the solvent. After the elastomer was removed from the reactor and it was additionally dried for 24 hours at 40 °C in a vacuum

oven.

Using this technique we obtained an opaque elastomer film. Then, even though the film was very thin, it was not suitable for our purposes.

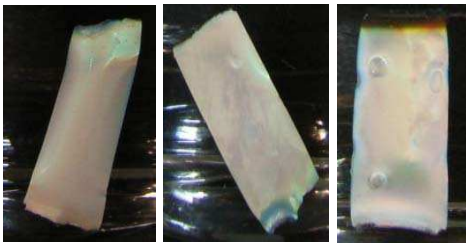

Figure 5.5: *Examples of Cholesteric elastomer obtained by the anisotropic deswelling.*

Anisotropic deswelling

During this process the centrifugal force constrains the molecules to align parallel to the reactor wall while the solvent evaporates the cross-linking acts.

To obtain cholesteric networks with a monodomain structure, it is necessary to achieve a network conformation that is consistent with the helicoidal structure of the cholesteric phase. Since a cholesteric phase is a twisted nematic phase, the local director $\hat{n}$ is not constant in space but helically arranged perpendicular to an axis that we call the z-axis. Because the local nematic chain conformation is prolate, the helicoidal arrangement of $\hat{n}$ in the z-direction will cause an overall oblate network conformation. This situation is very similar to a uniaxial compression of a nematic network in the z-direction that causes a planar orientation of the director with $\hat{n}$ perpendicular to the compression axis in the x,y-plane. [114] Unfortunately, a uniform uniaxial compression or biaxial mechanical deformation of a dry network or even of a swollen network causes experimental difficulties. To overcome these problems we make use of a deswelling process that is employed in the synthesis of the LC networks. Normally, a deswelling process is isotropic. The network deswells simultaneously in all dimensions and the spherical shape of the chain conformation of the network strands is not affected (Figure 5.6 a). However, if the deswelling process is performed anisotropically, the chain conformation becomes modified. To obtain an oblate conformation that should cause a uniform orientation of the cholesteric structure, we applied an anisotropic deswelling process as indicated in Figure 5.6 b. The process is accomplished in two steps to lock-in the network anisotropy.

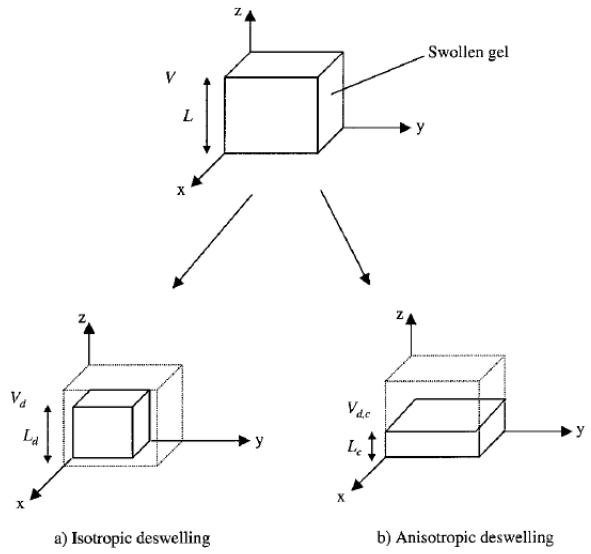

Figure 5.6: *Schematic representation of the isotropic (a) and anisotropic (b) deswelling process for Liquid crystal networks.*

In the first step, in a solution of the initial reactants, a weakly crosslinked gel is synthesized by a still incomplete crosslinking reaction. This isotropic gel exhibits a statistical, spherical network chain conformation. The second step represents the key point of the orientation process. In contrast to the isotropic deswelling described in Figure 5.6 a, the gel is allowed to deswell only in the z-direction while the dimensions in the x,y-plane stay constant (Figure 5.6 b). During the deswelling process, additionally the transformation of the isotropic gel into the cholesteric state takes place. Finally, under these conditions, the crosslinking reaction is completed. The resulting network exhibits an overall oblate chain conformation that should cause a planar orientation of $\hat{n}$ in the x,y-plane. The basic question remains as to whether the spontaneous twist elasticity of the cholesteric phase is sufficient to realize a uniform Grandjean texture with the helix axis parallel to the z-direction.

5.1.3 UV cross-linkable CLC polymer synthesis

In following we will describe the second technique used to prepare a proper CLC elastomer [112, 115].

Figure 5.7 shows the reaction scheme. 0.18g of polymethyl hydrosiloxane, 0.66g of 4-pentylphenyl-4' -(4-buteneoxy)benzoate, 0.12g of cholesterol pentenoate,

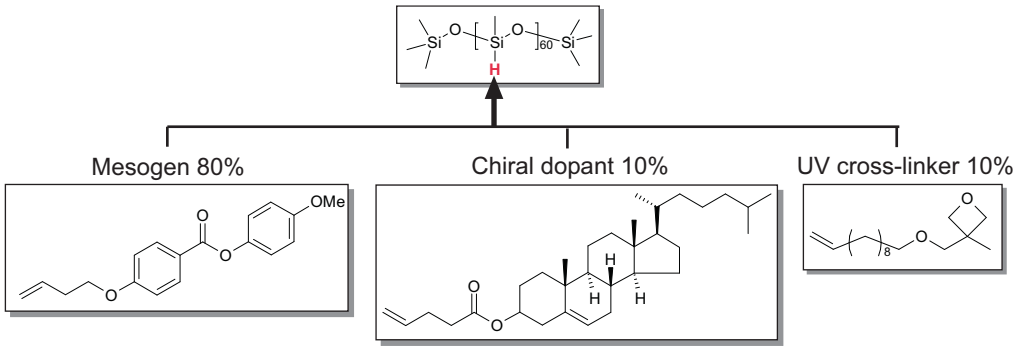

Figure 5.7: *Reaction scheme for UV cross-linkable choleseric LC polymer.*

and 0.063g of 3-methyl-3-oxetane-(11-undecene -methenether) were added to 3ml of toluene then stirred at 80 °C. 60μl of catalyst (COD), 1ml of DCM and 13ml of toluene were added to the solution then a reaction was carried out overnight. Another 20μl of the catalyst were added twice after five hours and twelve hours.

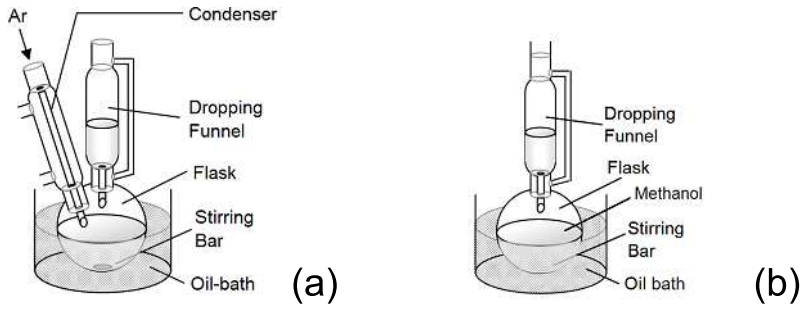

Figure 5.8: *Schematic representation of the chemical apparatus for the synthesis (a) and for the precipitation (b)*

The synthesized polymer was precipitated from methanol then vacuum dried at 60 °C overnight. The resulting polymer has an isotropic phase above Tc = 73 °C, the cholesteric phase below Tc, and the glass transition at Tg = 9 °C, figure 5.9.

The cholesteric nature of the liquid crystal phase is evident due to the characteristic iridescent colours of the material.

The addition of an initiator is needed to promote the UV cross-linking. The CLC polymer was dissolved in acetone then the solution was filtrated to remove all insoluble fragments and 0,5 wt%, or 1 wt% of 1-buthyl-3- methylimidazolium cloride was dissolved in the filtrated solution then vacuum dried at 40°C overnight.

The addition of the initiator allowed the cross-linking of the polymer. Adding

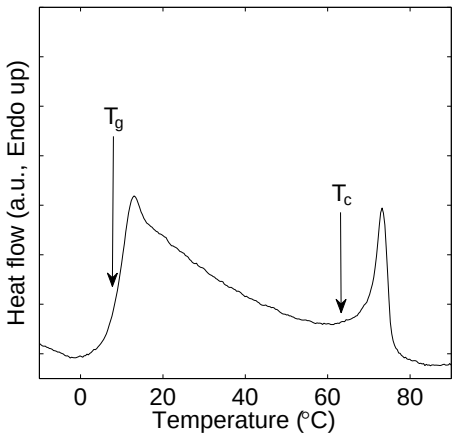

Figure 5.9: *Differential scanning calorimeter (DSC) trace of transitions in CLC polymer T_g and T_c denotes the glass transition temperature and the the critical temperature, respectively.*

0,5 wt% of the initiator a weak cross-linked was obtained while adding 1,0 wt% of the initiator a fully cross-linked elastomer was obtained, the absence of the initiator gives a non cross-linked elastomer.

Using this procedure the obtained elastomers were not in a form of a thin film but they are more like a little piece of rubber not yet suitable to be used in our measurements.

5.1.4 Alignment of the CLC elastomer

For optical measurements and applications well aligned thin cholesteric films are required. The film was prepared aligning the elastomer in a cell system, as it is well known in liquid crystals research.

A well aligned elastomer was obtained by using two techniques, in the first case the elastomer was pressed between two quartz plates, their surfaces was previously treated by spin coating with a water soluble polymer (PVA, Poly-Vinyl-Alcohol) and rubbed to promote an alignment direction. To control the thickness of the film two mylar stripes were inserted between the plates. The assembled cell was kept at 90 °C (in the isotropic phase) for three hours. The elastomer was then annealed for 48h at 60 °C, after cooling down at room temperature the sample was irradiated by UV light for cross-linking. The irradiation process was carried out only for those samples in which the initiator was added.

The same result was obtained first assembling the cell and then filling in an

oven at 300 °C and repeating the annealing and the irradiation processes.

Low molecular weight liquid crystal molecules align easily by this method, but due to the inherent viscosity of the CLC polymers, this process did not always provide a monodomain of cholesteric phase.

After the above described alignment procedures, the liquid crystal cell was soaked in water at 4 °C, to dissolve the PVA film. After for one week all the components of the cell were disassembled and it was possible to obtain a free standing film, floating on the surface of the water.

5.1.5 Mechanical support and active layer

Since the elastomer itself was very thin and fragile, a mechanical was necessary to handle it. For this reason we prepared a silicon elastomer. The mechanical support was prepared using a centrifuge in which the reactor walls were covered by a PTFE film. The reaction took place under centrifugation, the inner wall of the cylindrical reactor was covered with a PTFE film. 0.9 g of SYLGARD 184 BASE and 50μl of SYLGARD 184 CURING AGENT were dissolved in 2ml of toluene. The solution was placed within the reactor then it was closed by a lid having two small holes. A reaction was carried out under centrifugation at 5000rpm for 5 hours at 80 °C to obtain a uniform film thickness.

Using the so prepared silicon elastomer we collected the thin cholesteric film floating in water, as described in the previous section, then the whole elastomer-silicon system was dried at room temperature for 24h and vacuum dried at 40 °C overnight.

The same procedure used for the preparation of the mechanical support was also used to prepare the active layer. But in this case a photoluminescent dye was dispersed (0.05 wt%)into the silicon elastomer.

5.2 Tuning of the band gap and cross-linker effects

To measure the optical properties, of the elastomeric system the following experimental set-up was used 5.10.

Figure 5.10 shows an experimental set up for transmittance measurements . A quartz lamp equipped with a constant-current power supply (voltage output 7.5V) was used as a light source. The intensity of light was optimized by an adjustable

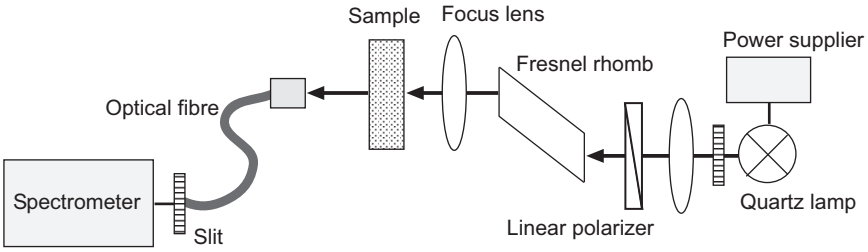

Figure 5.10: *Schematic representation of the experimental setup for transmission measurements.*

slit positioned at the window of the light source. The incident light was circularly polarized by a combination of a linear polarizer and a Fresnel rhomb. The linear polarizer was set to either +45° or -45° with respect to the optical axis to yield right and left handedness of circularly polarized incident light, respectively. The circularly polarized light was then normally incident on a sample mounted on a stretcher. The transmitted light was guided by an optical fibre to a spectrometer (Thermo- Oriel MS260i) with a spectral resolution of 1.5nm.

The CLC elastomer was stretched and the effects of sample elongation on the transmitted wavelengths were checked. We have also checked the effect of cross-linking on the optical properties of the system. The CLC elastomeric films were stretched from both ends in order to minimize the displacement of the measuring spot.

The performed measurements show (5.11) the tuning of the band gap position under mechanical uniaxial strain for non cross-linked and cross-linked elastomers.

In the non cross-linked CLC polymer (left), the selective reflection was only observed for right handed incident light, same handedness of the cholesteric helix. Since the depth of the band gap was almost constant over the whole elongation, it is clear that the chiral helical structure was maintained during the uniaxial strain. In the fully cross-linked CLC polymer (right), mechanical strain obviously distorted the helical structure. The selective reflection band for left handed incident light became comparable with the one for the right handed incident light at more than 30% elongation, proving that the original helical structure lost its chirality and then became a periodic structure having no chirality.

The effect of the cross-linker consists not only in the pitch variation but also in some deformations of the backbone, this gives rise to a periodic but achiral

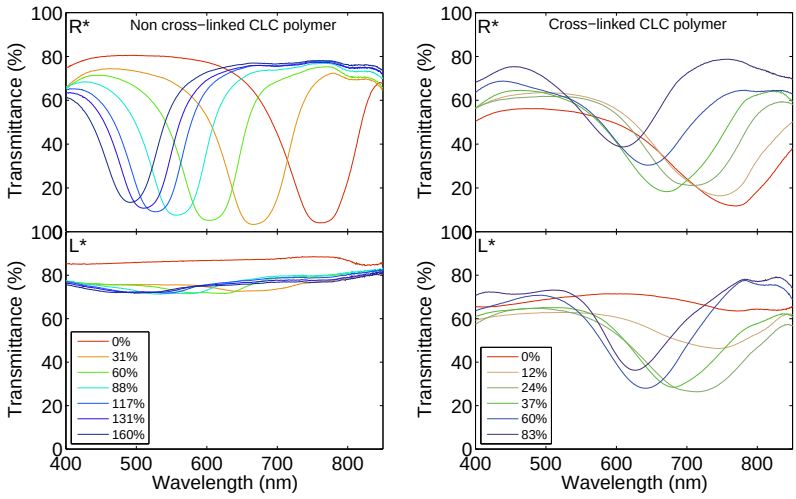

Figure 5.11: *Transmittance spectra of non cross-linked and fully cross-linked CLC polymer under uniaxial strain, R^* and L^* represents right and left handedness of the incidence light used, respectively. L^* spectra shows clear evolution of selective reflection band in the fully cross-linked CLC polymer, whereas no peak was seen in the non cross-linked CLC polymer.*

structure.

As shown in figure 1.15, a uniaxial stretching in the x direction (perpendicular to the helical axis) results in contraction in the y direction and the z direction (parallel to the helical axis). Since the contracted system has a shorter periodicity, both cross-linked and non cross-linked CLC elastomers experienced blue-shift of the selective reflection band when they were stretched (5.2). The contraction of the helical pitch, hence the contraction of the system in the z direction (ι_{zz}) is calculated from the peak shift [7] by:

$$\iota_{zz} = \frac{\lambda_c(\iota_{xx})}{\lambda_c(I)} \tag{5.2}$$

where $\lambda_c(\iota_{xx})$ is the band gap central wavelength of the selective reflection band under uniaxial strain ι_{xx}, and $\lambda_c(I)$ is the initial band gap central wavelength without strain.

Figure 5.12 plots λ_{zz} against the elongation along x to demonstrate how the system is deformed by the uniaxial stretching. In the case of non cross-linked CLC polymer, λ_{zz} follows the power law $\iota_{xx}^{-0.5}$. In this state, λ_{yy} also follows the same power law because of the incompressibility of the system. Therefore, the contraction occurs isotropically in both y and z directions.

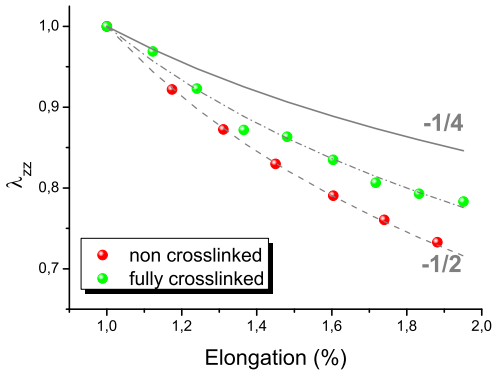

Figure 5.12: *The band-gap shift λ_{zz} (follows the contraction of cholesteric helix ι_{zz}) against imposed uniaxial strain. The non cross-linked CLC polymer plots on the line of $\iota_{xx}^{-0.5}$ showing the isotropic deformation (red), whereas the cross-linked CLC polymer plots on the line of $\iota_{xx}^{-0.38}$ showing the anisotropic deformation (green). The grey line represents the theoretical behavior of a fully crosslinked elastomer.*

On the other hand, in the case of fully cross-linked CLC polymer, λ_{zz} follows the power law $\iota_{xx}^{-0.38}$, implying λ_{yy} follows $\iota_{xx}^{-0.62}$. Therefore, the contraction occurs anisotropically in this system; more compressed in the y direction and less compressed in the z direction. Although this is an expected phenomenon, as mentioned in the first chapter (1.10.1), the value of scaling exponent is much smaller than the theoretical value of $-1/4$.

In order to further investigate the dynamics of cholesteric pitch under uniaxial strain, the relaxation process of the cholesteric helix under given constant strain, was studied by measuring transmittance spectrum evolution in time. Fig.5.13 plots the evolution of $\Delta\lambda(t)$ against time, where $\Delta\lambda(t)$ is the normalized peak shift of the selective reflection band, it was defined as:

$$\Delta\lambda(t) = \frac{\lambda(I) - \lambda(t)}{\lambda(I) - \lambda_{min}(0)} \tag{5.3}$$

where $\lambda(I)$ is the initial peak wavelength without strain, $\lambda(t)$ is the measured peak wavelength at a given time, and $\lambda_{min}(0)$ is the minimum peak wavelength (maximal shift) obtained at time $t = 0$. By this definition, $\Delta\lambda(t)$ stays equal to unity when the helix maintains the most contracted state without any relaxation, and it becomes zero if the pitch can return back to the initial non-strained value after a long relaxation.

As shown in fig 5.13 the effect of the cross-linker also influences the relaxation

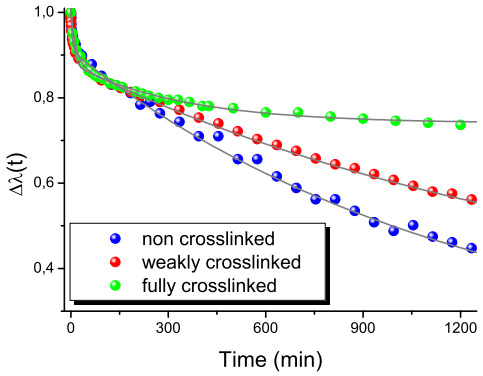

Figure 5.13: *Relaxation of the contracted helix under uniaxial strain: Non cross-linked (blue curve), weakly cross-linked (0.5wt% of initiator, red curve) and fully cross-linked (1.0 wt% of initiator, green curve) CLC elastomer.*

of the CLC elastomer after a constant stretching, the relaxation after stretching is faster when the the elastomer is not cross-linked. Then the use of a fully cross-linked elastomer is necessary for a more stable system.

5.3 Tunable lasing from CLC elastomers

Stimulated laser emission from CLC elastomers was verified by using a three layered structure a dye doped isotropic elastomer sandwiched between two cholesteric elastomers.

Different dyes (Rhodamine B, Rhodamine 6G and Pyrromethene-580) were used as photoluminescent dyes. In our "all-elastomer" device, we do not need to be precise about matching the band-gap position and the dye emission range, because it can be adjusted by uniaxial deformation, once the sample is mounted on the stretcher mechanism. When the position of the band gaps had overlapped the fluorescence emission range of the dye, then the laser emission was observed.

It is important to note that the laser emission was obtained in the middle of the selective reflection band where propagation of the light is restricted. This is expected since the flexible cholesteric liquid crystal elastomers in this configuration act as effective mirrors and the resonance in the cavity is most efficient in the middle of the reflection band [116].

Tuning of the laser peak with stretching was also achieved with this sample configuration as illustrated in fig. 5.14, where is shown the laser effect by using

the Rhodamine B as active dye.

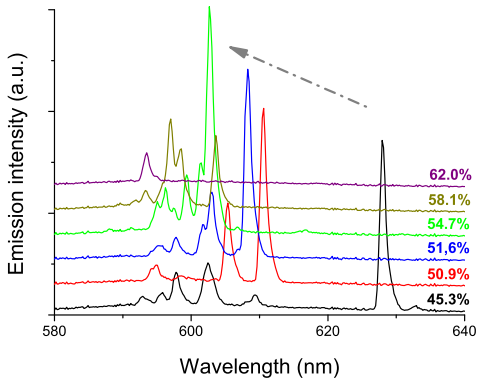

Figure 5.14: *Mechanical tuning of laser emission from the three layer system, using the Rhodamine B as luminescent dye. Elongation for each spectrum is shown on the right side. The pumping energy was about* $50mJ/cm^2$ *throughout the experiment.*

It is important to point out that no laser emission could be observed when the sample was unstretched, because the Rhodamine fluorescence emission and the selective reflection band gap of the cholesteric elastomers did not overlap. The lasing was observed only when the sample elongation was around 45% and the achieved tuning of the laser wavelength was 36nm, from 592 to 628 nm. One distinctive primary emission line and several weak secondary emission lines were observed simultaneously. Although the primary emission shifted depending on the sample elongation, weak secondary lines hardly shifted centering around the luminescent wavelength of the dye. The primary emission can be interpreted as a defect mode lasing since it always occurs near the λ_c, peak top of the selective reflection band. It shifted following the shift of the λ_c when the sample was uniaxially stretched.

5.3.1 From multi-mode to single-mode lasing effect: the "notch" configuration

As shown in fig 5.14 the lasing obtained from the three layered system was essentially a multi-mode effect, to achieve the single-mode lasing from these systems, we exploited the situation described in 4.1.2 [117]. In that work the single-mode lasing was obtained by using two cholesteric liquid crystals whose selective reflection bands were shifted one respect to the other in a way that only the edges of

band gaps overlapped.

To obtain the shift of the reflection bands were investigated two different methods:

1. chemical composition
2. differential stretching.

In the first case the concentration of the chiral compound was changed, as for low molecular weight liquid crystals, while in the second case the shift of the band gaps was obtained by a differential stretching of the two cholesteric elastomers, the two situations are depicted in fig. 5.15.

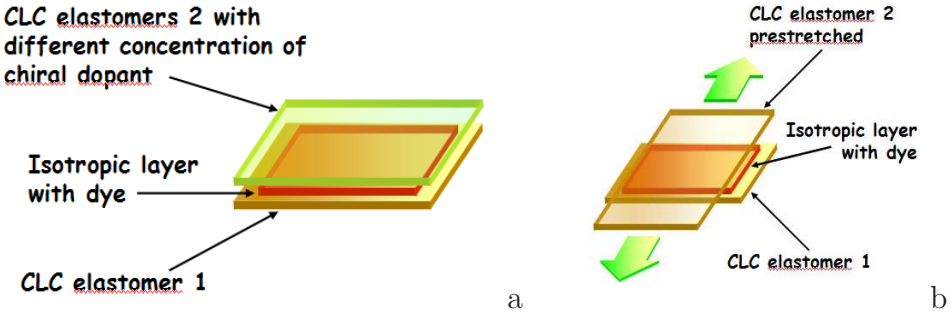

Figure 5.15: *Schematic representation of the three layered system obtained by changing the concentration of the chiral dopant (a) and by differential stretching (b).*

The transmittance measurements were carried out using the same set-up described in fig 5.10, the transmission spectrum of the system obtained using two cholesteric elastomers with different concentration of chiral dopant (20% of chiral dopant for the first elastomer and 23% of chiral dopant for the second one) clearly shows the region of overlapping of the two band gaps (fig.5.16 black curve), like a hill in the middle of the reflective band gap. We called this hill "notch". In figure 5.16 are also reported the transmission spectra of the elastomer containing 20% of chiral dopant (blue curve) and of the elastomer containing 23% (red curve). The optical response to the uniaxial mechanical strain shows that the "combined" gap shifts in the same way as for a single cholesteric elastomer. Figure 5.17(a) shows the shift of the combined band gap for different percentages of strain. The system at rest position, without any strain (grey curve), was stretched many times and the position of the band gap was observed to shift to lower wavelengths increasing the percentage of strain (10% red curve, 28% cyan curve, 39% green curve and

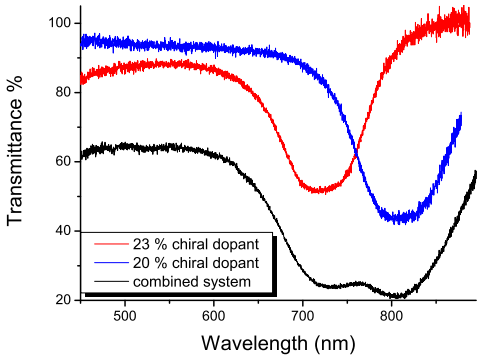

Figure 5.16: *Transmittance spectrum of the layered system (black curve) obtained using two cholesteric elastomers with different concentration (20% blue curve and 23% red curve) of the chiral dopant.*

51% magenta curve). Following the shift of the band gaps, also the "notch" shifts to lower wavelengths fig. 5.17(b).

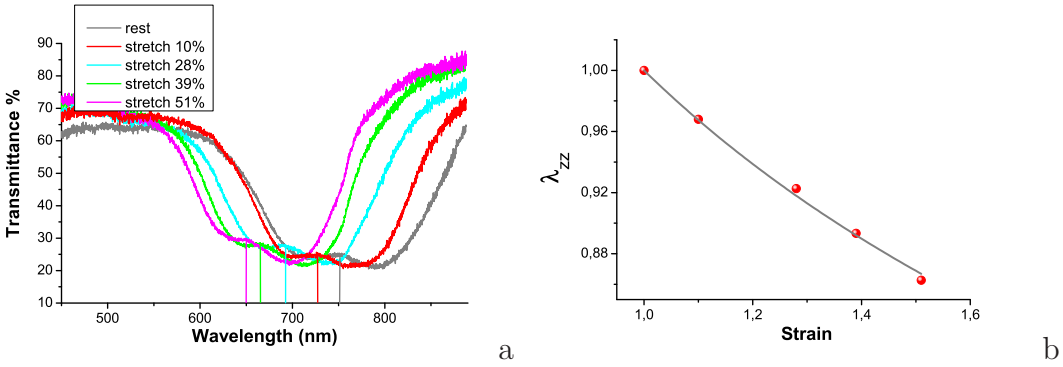

Figure 5.17: *Transmittance spectra of the layered system obtained changing the concentration of the chiral dopant, under uniaxial strain [rest position grey curve, 10% of strain red curve, 28% cyan, 39% green and 51% magenta] (a). The shift of the "notch" follows the shift of the band gaps due to the uniaxial strain as a single elastomer (b).*

The second investigated method consisted in using two cholesteric elastomers with the same concentration of chiral compound and pre-stretching one of them. Assembling a layered system using this technique the shift of the two gaps was obtained, a well defined overlapped region as can be observed from fig 5.18 was achieved in this case.

The assembled system was then in all stretched in order to obtain the band gap shift of the whole layered structure. In fig. 5.19(a), are shown the transmittance

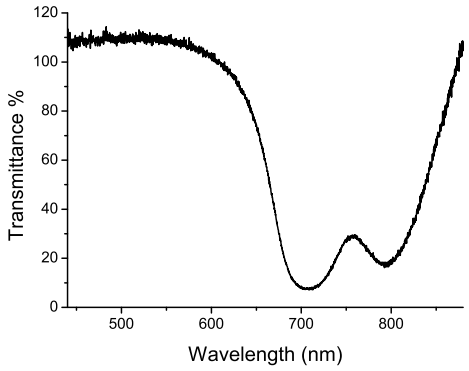

Figure 5.18: *Transmittance spectrum of the layered system obtained using the differential stretching of the two cholesteric elastomers.*

spectra that shift to lower wavelengths under different percentages of strain (rest position grey line, 5% of strain orange, 13% cyan, 19% green and 26% magenta). From fig. 5.19(b) it is possible to observe that also in this case the "notch" shifts to lower wavelengths following the shift of the two band gaps.

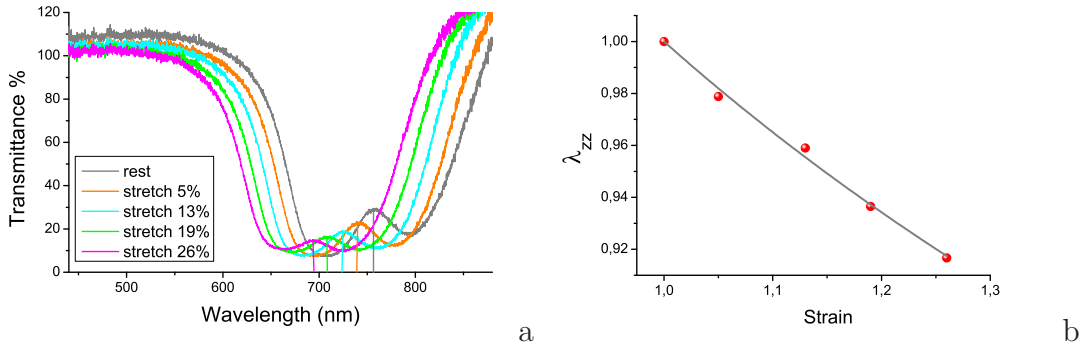

Figure 5.19: *Transmittance spectra of the layered system obtained by differential stretching, under uniaxial strain [rest position grey curve, 5% of stain orange, 13% cyan, 19% green and 26% magenta](a), the shift of the "notch" follows the shift of the band gaps due to the uniaxial strain as a single elastomer (b).*

To achieve the laser effect we chose the pre-stretching configuration, because in this case the band gap was better defined and even because the obtained samples were more homogeneous with respect to the samples obtained by changing the concentration of the chiral compound.

The entire structure was pumped by using a 532nm pulsed laser beam (pulse duration $\approx 4ns$) from a frequency doubled ND:YAG laser (AOT). In figure 5.20

it is shown a picture of the experimental set-up used to achieve laser emission from the elastomeric system.

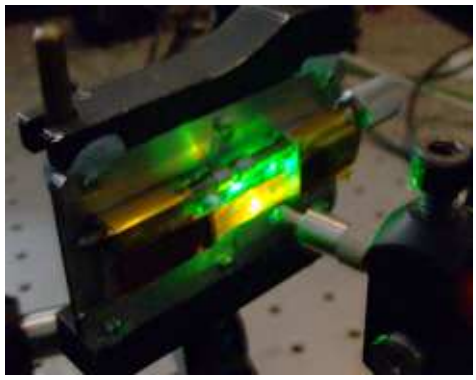

Figure 5.20: *Picture of the set up used for laser emission studies.*

Laser emission was observed at the "notch" as well as the modulation of the laser wavelength in response of the stretching of the elastomeric layered system.

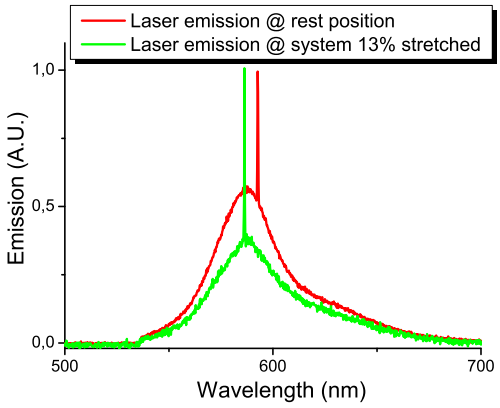

Figure 5.21: *Laser emission from the three layered system, the laser emission was modulated by mechanical stretching of the entire cholesteric elastomeric system. The red curve represents the laser obtained without any stretching of the system, while the green one shows the laser emission from the 13% stretched system.*

In fig. 5.21 it is shown laser emission from the layered structure where the active layer was prepared using the pyrromethene-580 as photoluminescent dye (red curve), and the modulation of the emitted wavelength due to a uniaxial mechanical elongation of 13% (green curve).

Unfortunately, the observed emission was not stable enough to measure the threshold energy. Emission intensity became quickly smaller, then it disappeared completely. This was certainly due to the photo-bleaching of the dye under pumping. We only could crudely estimate the threshold energy as $7mJ/cm^2$ since it was the minimum energy to achieve laser emission while moving the pumping spot across the sample. The estimated energy is much lower than $191mJ/cm^2$, the threshold energy in dye-doped single cholesteric elastomer of Shmidtke et al. [110]. This evaluation is in agreement with the report of Song et al [111] where they reported a lower threshold in the case of three layered system with respect to single cholesteric.

Using the shift of the two band gaps it was possible for the first time to obtain a single line laser emission from a layered elastomeric system, as well as the modulation of the laser wavelength by uniaxial strain.

In order to improve the stability of the system, we have the idea to use a porous layer as active layer. Using this layer the dye solution will slowly circulate through the layer, preventing in this way the localized photo-bleaching similarly to conventional dye lasers. This research is still in progress.

Chapter 6

UV sensors

Exposure to ultraviolet radiation can be dangerous for human health. The higher energy photons have sufficient energy to produce photochemical alterations that may induce biological effects. Both beneficial effects such as vitamin D synthesis as well as unwanted effects as skin cancer, result from exposure to ultraviolet light. The organs that are most critically affected by a long exposure to UV light are eyes and skin since they are readily exposed. The biological effects are directly related to the wavelength of the incident photons. UV radiation can be divided into three main categories UVA (320-400 nm), UVB (280-320 nm) and UVC (100-280 nm). Wavelengths in the UVB region are absorbed into the skin, producing erythema, burn and eventually skin cancer. Laboratory studies have shown that the first step of carcinogenesis are the UV induction of the DNA damage and the occasional mistake in the repair of this damage that leads to the incorporation of wrong bases into the genetic material. In the past years scientists have put a lot of emphasis on the necessity to monitor the daily UV exposure to solar light. In the 80's McKinley and Diffey proposed an erythemal response spectrum (ERS) related to human skin, i.e. a spectrum of the relative sensitivity of the skin as a function of the wavelength of the incident radiation. This spectrum has become a widely accepted standard [118].

The minimal erythemal dose (MED) has been defined by medical researchers as the minimal dose necessary to produce a visible erythemal reaction. Exposure to UV radiation longer than one MED is dangerous, but also repeated exposures to radiation levels below one MED could have a cumulative effect and produce an erythema. In the past years several devices were developed to monitor the erythemal effect of UV radiation. The most popular among them are based on

the Robertson-Berger Spectrophotometer developed in the 70's. The principle of operation of this device is the following: the sunlight passes through a quartz window and then through a UV transparent filter (Schott UGS) that absorbs almost all the visible light except a small part of red light (700-850 nm). The radiation transmitted by the filter hits a UV sensitive phosphorescent material, (MgWO.sub.4) that absorbs radiation and emits it as visible green light. The fluorescence light goes through a second filter (Corning 4010) that stops the red light. The intensity of the fluorescence light is measured by a solid state photodiode GaAsP, not sensitive to red light and with a maximum of sensitivity at the green wavelength. This device is a solar blind detector system that responds to UVB.

In the following years other devices able to sufficiently mimic the human skin were developed, in which no phosphorescent materials were present. In those devices the sunlight passes through a detector sensitive to UVB radiation and a photodiode receives directly the radiation coming from the filter [119–122].

Recently the use of liquid crystalline materials as active elements in UV sensors has been proposed. In particular two cholesteric liquid crystal mixtures, that change their color when exposed to UV radiation, have been proposed. The first mixture is based on a cholesteric system (nematic + optically active dopant) doped with ergosterol (provitamin D2) or with 7-dehydrocholesterol (provitamin D3) [123, 124]. In the second cholesteric mixture a nematic component, sensitive to UVB and based on a derivative of cinnamate (CH=CH-COO) [125], has been used. In both cases the change of selective reflection wavelengths (helical pitch), following UV exposure, is the basic effect. The main drawback is that in these systems a simple change in the color of the mixture cannot give quantitative information on the effective absorbed UV dose.

6.1 UV sensors based on cyanobiphenyls

We have developed a new class of UV detectors based on liquid crystals. The system is based on the optical effect of a liquid crystalline photo-luminescent mixture prepared using cyanobiphenyl materials, together with nematic liquid crystals and chiral dopants. The nematic liquid crystal is used to control the transition temperature from nematic to isotropic, in order to give a better stability to the mixture even at high temperatures. The chiral component is used to enhance the absorption hence the emission efficiency of the whole mixture.

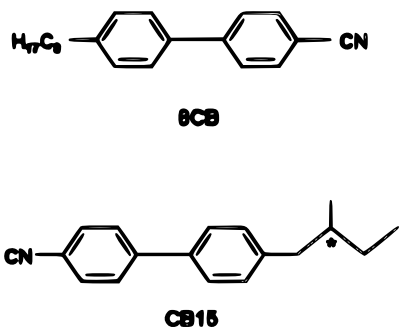

Figure 6.1: *Chemical structure of photoluminescent materials CB-15 and 8CB.*

The following photosensitive materials are used: cyanobiphenyls 8CB [4-n-octyl-4'-cyanobiphenyl] and CB15 [4-(2-methylbutyl)-4'-cyanobiphenyl], their chemical structure is shown in figure 6.1. CB15 also has chiral properties. The cholesteric MLC-6248 as chiral dopant and the nematic MLC-6816 as host material are used. All liquid crystals are supplied by Merck (Darmstadt, Germany).

The fluorescent behavior of 4-alkyl-4'-cyanobiphenyl (nCB) materials has been extensively studied in homogeneous solutions as well as for the pure material [126]. In low concentrations the excited singlet state $1nCB*$ has a strong emission at 330nm with a short lifetime ($\sim 1ns$) but at higher concentrations there is an excimers formation $2(nCB)*$ that efficiently emit at 400nm with a longer lifetime ($\sim 10ns$). In the nematic phase of neat nCB the excimer formation is favored by the molecular core packing, whereas the excimer formation is less efficient in the smectic A phase due to the higher viscosity. In the isotropic phase both the monomer and excimer emissions contribute to the fluorescence [127–129].

In our system the mixture containing the cyanobiphenyl material is placed in a sandwich cell, between two quartz plates with a thickness in the range between 1 and few tenths of microns. A fiber optic spectrophotometer and an Halogen-Deuterium lamp (AVS-S2000 and DH-2000, Avantes, The Netherlands) are used for absorption measurements together with an heating stage for optical bench (Serie F, Calctec, Italy) to investigate the stability of these mixtures at increasing temperatures. For photoluminescence measurements a mercury lamp is used as UV light source (HG 100 AS, Jelosil, Italy).

In figure 6.2 are shown the drawings of the typical experimental setup for absorption [a] and emission measurements [b]. The spectrophotometer sensor is aligned at 90° with respect to the light source and at 45° with respect to the LC cell perpendicular.

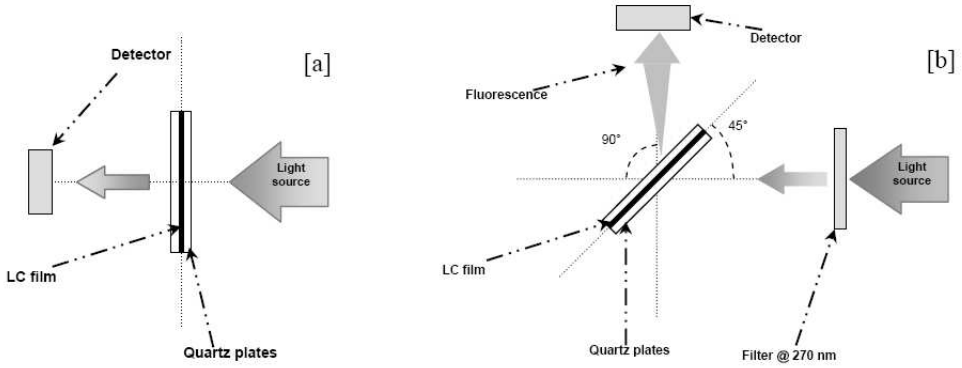

Figure 6.2: *Experimental setup used for absorption measurements [a] and for photoluminescence measurements [b].*

The visual angle is not of dramatic importance because the photoluminescence is an incoherent emission of light and it has not favourite directions. The used geometry described above has been chosen to avoid detection of the main beam. Figures 6.3 and 6.4 show the absorption spectra of two mixtures with different concentrations of photoluminescent material [a) 92% MLC-6816 + 8% CB-15; b) 70% MLC-6816 + 30% CB-15] obtained for different cell thicknesses (5μm red curve, 10μm green and 20μm blue), in comparison with the ERS (black). It is evident that varying the concentration of the photo-luminescent material as well as the thickness of the cell it is possible to modulate the absorption spectra of the mixtures to make it as similar as possible to ERS.

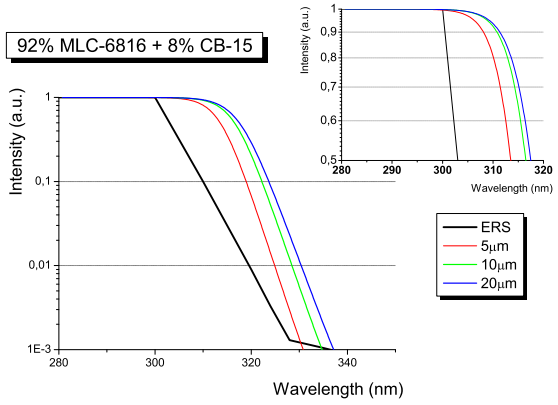

Figure 6.3: *Absorption spectra of mixture a) 92% MLC-6816 + 8% CB-15 for different cell thicknesses, 5μm red curve, 10μm green and 20μm blue, in comparison with the ERS (black) .*

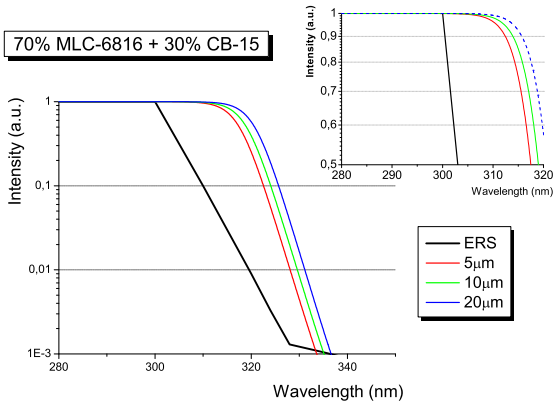

Figure 6.4: *Absorption spectra of mixture b) 70% MLC-6816 + 30% CB-15 for different cell thicknesses 5μm red curve, 10μm green and 20μm blue, in comparison with the ERS (black).*

A new mixture has been analyzed using another photosensitive material 8CB and a chiral dopant [c) 78%(92% MLC-6816 + 8% 8CB) + 22% MLC-6248]. In figure 6.5 it is shown the absorption behavior of the mixture for different cell thicknesses (2μm red curve, 5μm green and 7μm blue) and in figure 6.6 is made a comparison between this mixture and mixture a) for two cells of the same thickness, always using the ERS as reference spectrum (black). Mixture c) seems to better mimic the ERS with respect to mixture a). Figure 6.7 shows the emission spectra of mixtures a) and c) for the same cells. It is interesting to note that the mixture containing 8CB has a bigger intensity of the photo-emitted light with respect to the one provided by the mixture containing CB15 even if the concentration of this material is higher.

These results suggest that mixture c) better resembles the human skin behavior and gives a better compromise between the cell thickness and the photoluminescent material concentration, providing at the same time an absorption spectrum closer to ERS and an intense emission peak. A high emission intensity is easier to detect in a device that uses photodiodes to provide quantitative information about sunlight absorption.

Finally figure 6.8 shows the absorption spectra for the last mixture as a function of temperature. It is clearly seen as the absorption spectrum is stable from room to high temperature like 80°C. This property is of fundamental importance when designing a particular device that will undergo a continuous exposure to the direct sunlight. Stability and good emission properties are important but also

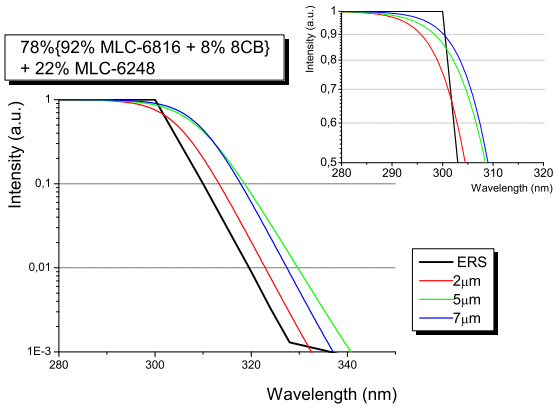

Figure 6.5: *Absorption spectra of mixture c) 78%92% MLC-6816 + 8% 8CB + 22% MLC-6248 for different cell thicknesses, (2μm red curve, 5μm green and 7μm blue, in comparison with the ERS (black).*

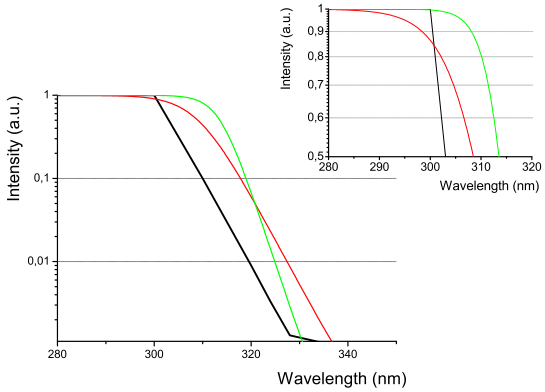

Figure 6.6: *Comparison between absorption spectra for mixture a) 92% MLC-6816 + 8% CB-15 and mixture c) 78%{92% MLC-6816 + 8% 8CB} + 22% MLC-6248 at the same cell thickness (5μm).*

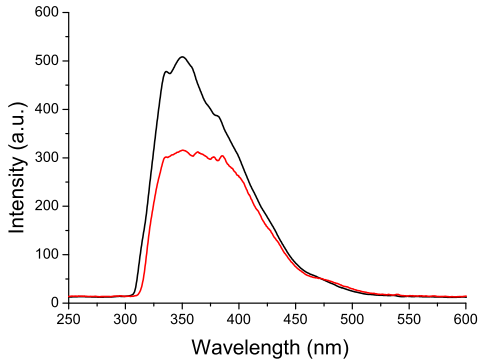

Figure 6.7: *Comparison between photoluminescence emission spectra for mixture a) 92% MLC-6816 + 8% CB-15 and mixture c) 78%{92% MLC-6816 + 8% 8CB} + 22% MLC-6248 at the same cell thickness (5μm).*

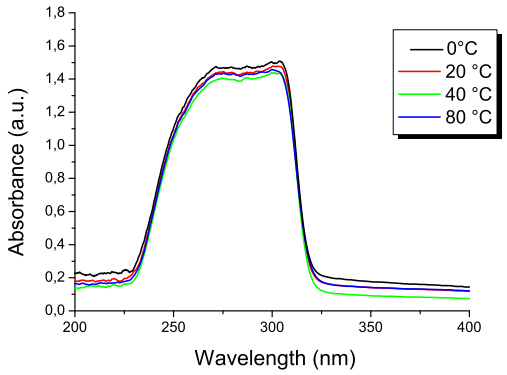

Figure 6.8: *Temperature dependence of the absorption spectrum for mixture c) 78%{92% MLC-6816 + 8% 8CB} + 22% MLC-6248; black line $T = 0^{\circ}C$, red line $T = 20\,^{\circ}C$, green line $T = 40^{\circ}C$ and blue line $T = 80^{\circ}C$.*

other characteristics of the sensor such as the low costs of production together with its capability to be encapsulated in a flexible substrate are of fundamental importance in the development of a device. In a possible prototype, a filter could be placed in front of our sensor in order to prevent the visible light to hit our mixture, then the photoluminescence could pass through a second filter in order to select the maximum wavelength of emission. A photodiode could be placed just after the second filter in order to quantitatively measure the emitted light.

6.2 UV sensor based on a photo-luminescent dye

The main disadvantage of the detector proposed in the previous section is related to the fact that the light emitted by the mixture is still very close to the UV part of the electromagnetic spectrum. In present section another photosensitive liquid crystalline mixture is presented to improve the performances of the previous one based on cyanobiphenyl materials. In this case a photoluminescent dye,with a high emission in the visible range, is included within the liquid crystal mixture of nematic and chiral compounds.

The cholesteric liquid crystal mixture was prepared using a nematic compound and a chiral dopant. As in the previous case the nematic liquid crystal was used to control the transition temperature from nematic to isotropic, in order to give a better stability to the mixture even at high temperatures. The chiral component was used to enhance the absorption hence the emission efficiency of the whole mixture. Finally the mixture is doped by a photoluminescent dye: N,N dimethyl-4(4-nitrostyryl)aniline, its chemical formula is shown in figure 6.9. The homologue (diethyl-) of this dye was used in [130] to estimate the order

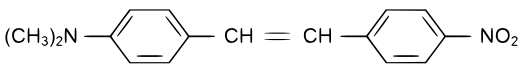

Figure 6.9: *Chemical formula of the photoluminescent dye.*

parameter of a nematic liquid crystal by its polarized luminescence. The dye absorbs in 220 - 350nm range and emits at 573nm, due to a $\pi - \pi^*$ transition. Again the cholesteric MLC-6248 as a chiral dopant and the nematic MLC-6816 as a host material are used. MLC-6816 belongs to cyclohexylcyclohexanes and has only the nematic phase ($30^\circ \rightarrow N \rightarrow 76.5^\circ \rightarrow I$), MLC-6248 is a non-mesogenic compound with the following temperature diagram: $K \rightarrow 48^\circ \rightarrow I$.

The choice to use a common solvent, in which simply dissolve the dye, is not a viable one for a device that has to be exposed to direct sunlight.

All liquid crystals are supplied by Merck (Germany). For our experiment the following liquid crystal mixture is prepared: $99.7\%\{80\%MLC-6816+20\%MLC-6248\}+0.3\%dye$ The concentration of the dye is fixed at 0.3 wt% due to the solubility of this material in the liquid crystal compound. The liquid crystal mixture is placed in a sandwich cell between two fused silica plates with a thickness in the range between 1 and several tens of microns. It is known that some dyes are very soluble in LC. If a small amount of dichroic dye ("guest") is dissolved in nematic LC ("host"), the dye molecules align along the preferable orientation of the LC molecules (director). The obtained mixture possesses dichroic absorption. The same effect is observed for a cholesteric liquid-crystal (CLC) host: if a small amount of dye, possessing linear dichroic absorption, is dissolved in the CLC, the elongated dye molecules follow the helical director orientation and the helical arrangement transforms linear dichroism into a circular dichroism. By LC-molecule reorientation, the absorption properties can be affected. This helical structure optimizes the absorption of light from the mixture.

The typical experimental setups and the instrumentation used for absorption and emission measurements are the same presented in the previous section 6.2. In solution, the photoluminescent dye absorbs UV radiation and emits light in the visible range.

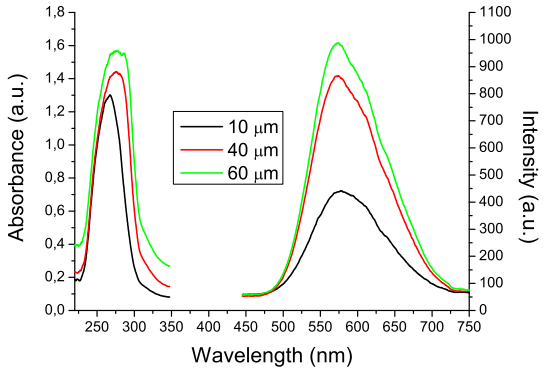

Figure 6.10: *Absorption (left) and emission (right) spectra of the liquid crystal-dye mixture for different thicknesses, 10 black line , 40 red line and 60μm green line.*

In figure 6.10 the absorption and emission spectra of the liquid crystal-dye mixture for different thicknesses, 10 (black line), 40 (red line) and 60 μm (green

line), of the cell are shown.

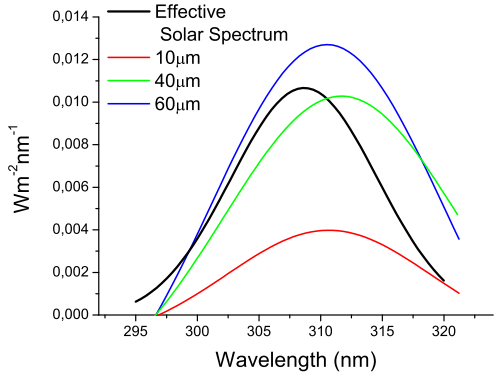

Figure 6.11: *Spectral irradiance of the mixture confined in cells with different thicknesses, 10 red, 40 green and 60μm blue line, compared to the effective solar spectrum (black line).*

Figure 6.11 shows how our mixture behavior, for different cell thicknesses (10 red, 40 green and 60μm blue line), is close to the effective solar spectrum (black line). A modulation of the absorption spectrum and the right condition that better mimic the human skin behavior is obtained varying the thickness of the cell. Data in figure 4 suggest that a cell with 60 μm thickness is the best choice. Figure 6.12 shows how the absorption spectrum is constant in temperature from 0 °C to 80 °C. Figure 6.13 shows a comparison between the emitted fluorescent

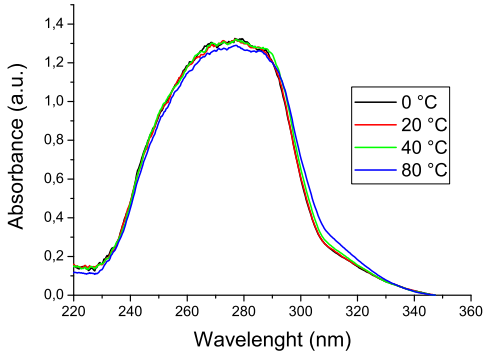

Figure 6.12: *Absorption spectrum of the mixture as a function of temperature; black line $T = 0\,^{\circ}C$, red line $T = 20\,^{\circ}C$, green line $T = 40\,^{\circ}C$ and blue line $T = 80\,^{\circ}C$.*

light from a mixture with cyanobiphenyl materials and the mixture with the photoluminescent dye when illuminated with a mercury lamp filtered at 270nm.

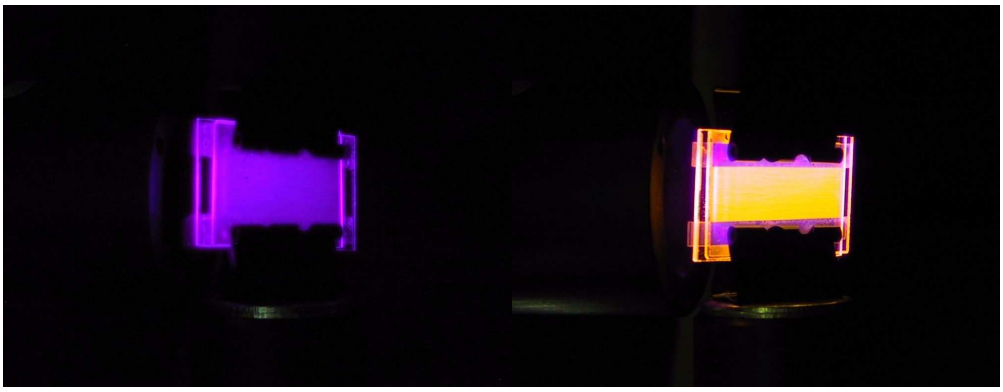

Figure 6.13: *Light emitted by a cell containing a cyanobiphenyl mixture (right) and by a cell containing the cholesteric-dye mixture (left) when illuminated with a Mercury lamp filtered at 270nm.*

It is clearly seen that the emission intensity coming out from the liquid crystal and dye mixture is more intense than the one coming out from the other cell. Moreover the emission wavelengths in the yellow-orange range is easier to detect in a device that uses commercial photodiodes to provide quantitative information. Finally the possibility to mix the dye with a polymer, for instance, Poly-methyl-methacrylate, transparent to UV, has been examined. The mixture results more stable mechanically and in temperature but its absorption properties are affected by the solvatochromic effect that makes it not suitable for a UV dosimeter. Stability and good emission properties are important but also other characteristics of the sensor such as the low costs of production together with its capability to be encapsulated in a flexible substrate are of fundamental importance in the development of a device. In a possible prototype, a filter could be placed in front of our sensor in order to prevent the visible light to hit our mixture, then the photoluminescence could pass through a second filter in order to select the maximum wavelength of emission. A photodiode could be placed just after the second filter in order to quantitatively measure the emitted light.

These new class of UV sensor provide a way to develop a device that indicates for instance the daily dose of UV exposure for applications in medicine, pharmacology or cosmetics.

Conclusion and future work

A typical liquid crystal laser consists of a liquid crystal host and a fluorescent laser dye, where the liquid crystal host provides the feedback and the laser dye provides the gain. The original concept of lasing in liquid crystals was put forward in early '70s, then it took 25 years before liquid crystal lasing was actually experimentally demonstrated. During all these years from the prediction to the demonstration of lasing in liquid crystals, a considerable research effort has been conducted for a better understanding of the optical properties of materials exhibiting photonic band gap.

This thesis is focused on photonic band gap structures produced in liquid crystals, which can be organized as materials with a regular, periodic dielectric structure (as it is the case of the cholesteric phase) and then may be used to generate coherent laser light. The idea to build up lasers using liquid crystals is quite old and well known and many techniques to achieve the modulation of the laser emitted wavelength were developed during the last twenty years. In this thesis, the use of azo- and azoxy- compounds has allowed to obtain the very advanced all optical tunability, i.e. the laser system is totally controlled by light. Some special designed compounds (fluorene derivatives) allowed a fine tuning of the emitted wavelength and moreover the design of special samples permitted to obtain lasing from a wide range of dyes and its tuning in a wide range of wavelengths.

Due to practical problems, mainly related to the stability of the lasing system, as well as to its efficiency, so far actual technological applications of these kind of devices have been severely limited. In fact, up to now, they have never been used in a commercial device. A lot of effort is therefore devoted to solve these problems and hence to improve the technological feasibility and reliability of the

cholesteric liquid crystal lasers.

We described several different mechanisms to improve the lasing stability, as the development of a rotation movement of our samples during the lasing emission and the possibility to assemble multilayered cells that present the advantage to separate the cholesteric structure from the dye layer, increasing at the same time the efficiency of the system. These practical solutions allow to build micro-lasers whose emission is very stable in time and which, at the same time, can use a dye which is not soluble in the liquid crystal material. Moreover, we performed a deep study of surface treatments of the plates assembling the cell that contains the liquid crystal, to find the better accommodation for the cholesteric helix, giving rise to the more efficient laser emission. Finally, all these results have been used to develop a series of prototypes, also exploiting their miniaturization to be combined with the fiber optics technology.

Advanced results have been obtained by studying the optical properties of cholesteric liquid crystal elastomers and we succeeded in obtaining laser emission assembling a particular three layered system, where the central layer was doped by a luminescent dye and the external layers were made by suitable photonic elastomers. The mechanical uniaxial stretching of the entire elastomeric system then also allowed for the first time the tuning of the emitted laser wavelength. Also in this case, a lot of problems related to the stability of the laser emission comes out. In the next future, they could be solved by a porous layer that will allow the slow flowing of a dye solution.

Other experimental results are related with the application of a cholesteric liquid crystal combined with photoluminescent compounds to develop novel UV sensing devices. In particular this part of the research was mainly focused on the mimic of the behavior of the human skin under direct sun light exposure.

As discussed, the soft matter nature of these materials and their response to external stimuli leads to many different applications, with the main examples in the field of mirror-less lasers. The broad wavelength tuning range of liquid crystal lasers, coupled with their microscopic size, narrow line-widths, high optical efficiencies, and their suitability for fiber optics, is opening up new developments in relevant areas such as medical diagnostics, dermatology, holography, etc. A lot of issues are still under investigation and a lot of work remains to improve and enlarge the applicability of these materials.

Bibliography

[1] M.G. Friedel. The mesomorphic states of matter. *Annales de Physique*, 18:273–474, 1922.

[2] O. Lehmann. On flowing crystals. *Zeitschrift für Physikalische Chemie*, 4:462–472, 1889.

[3] P.G. de Gennes and J.Prost. *The Physics of Liquid Crystals*. Oxford: Clarendon Press, 1993.

[4] S. Chandrasekhar. *Liquid Crystals*. Cambridge University press, second edition, 2004.

[5] Prof. L. Blinov. Thermotropic liquidc rystals, part b, January-March 2006. handout of the doctoral course.

[6] H.S. Kitzerow and C. Bahr. *Chirality in liquid crystals*. Springer-Verlag, New York, 2001.

[7] M. Warner and E.T. Terentjev. *Liquid Crystal Elastomers*. Oxford science publications, 2003.

[8] P. Xie and R. Zhang. Liquid crystal elastomers, networks and gels: advanced smart materials. *Journal of material chemistry*, 15(26):2529–2550, 2005.

[9] M. Warner E.M. Terentjev, R.B. Meyer and Y.Mao. Untwisting of a cholesteric elastomer by a mechanical field. *Physical Review Letters*, 85(11):2320, 2000.

[10] A.R. Tajbakhsh P.Cicuta and E.M. Terentjev. Photonic gaps in cholesteric elastomers under deformation. *Physical Review E*, 70:011703, 2004.

[11] P. Vukusich. Natural photonics. *Physic World*, pages 35–39, February 2004.

[12] L. Brillouin. *Wave propagation in periodic structures*. Wiley, New York, 1946.

[13] J.D. Joannopoulos R.D. Mead and J.N. Winn. *Photonic crystals: molding the flow of light*. Princeton University press, Princeton, 1995.

[14] E. Yablonovitch. Photonic band-gap structures. *J. Opt. Soc. Am. B*, 10(2):283–295, 1993.

[15] E. Yablonovitch. Inhibited spontaneous emission in solid-state physics and electronics. *Physical review letters*, 58:2059, 1987.

[16] Feng Duan and Jin Guoiun. *Introduction to condensed matter physics*. World Scientific Pubblishing, Singapore, first edition, 2005.

[17] J.M. Ziman. *Principles of the theory of solids*. Cambridge University press, Cambridge, 1972.

[18] P.M. Hui and H.F. Johnson. Photonic band-gap materials. *Solid State Phys.*, 49:151, 1996.

[19] P. Yeh. *Optical waves in layered media*. John Wiley & Sons, New York, 1990.

[20] M. Fox. *Quantum optics, an introduction*. Oxford University press, New York, 2006.

[21] V.I. Kopp, Z.-Q Zhang, and A.Z. Genack. Lasing in chiral photonic structures. *Progress in Quantum Electronics*, 27:369–416, 2003.

[22] B. Valeur. *Molecular Fluorescence: Principles and Applications*. Wiley-VCH Verlag GmbH, Weinheim, 2001.

[23] J.R. Lakowicz. *Principles of fluorescence spectroscopy*. Plenum press, 2nd edition, 1999.

[24] R.D. Meade A.M. Rappe K.D. Brommer E. Yablonovitch, T.J. Gmitter and J.D. Joannopoulos. Donor and acceptor modes in photonic band structure. *Phys. Rev. Lett.*, 67(24):3380–3383, 1991.

[25] J.E. Kim H.Y. Park J.-C. Lee Y.C. Yang, C.S. Kee and Y.-J. Jeon. Photonic defect modes of cholesteric liquid crystals. *Phys. Rev. E*, 60(6):6852–6854, 1999.

[26] A. Scherer A. Yariv J.D. O'Brien P.D. Dapkus O. Painter, R.K. Lee and I. Kim. Two-dimensional photonic band-gap defect mode laser. *Science*, 284:1819–1821, 1999.

[27] H. Kogelnik and C.V. Shank. Stimulated emission in a periodic structure. *Appl. Phys. Lett.*, 18(14):152–154, 1971.

[28] L.S. Goldberg and J.M. Schnur. Tunable internal-feedback liquid crystal dye laser. *US patent 3 771 065*, 1973.

[29] I.P. Il'chishin, E.A. Tikhonov, V.G. Tishchenko, and M.T. Shpak. Generation of tunable radiation by impurity cholesteric liquid crystals. *Sov. JEPT Letters*, 32:24–27, 1980.

[30] V.I. Kopp, B. Fan, H.K.M. Vithana, and A.Z. Genack. Low-threshold lasing at the edge of a photonic stop band in cholesteric liquid crystals. *Opt.Lett.*, 23:1707–1709, 1998.

[31] P. Palffy-Muhoray B. Taheri and H. Kabir. Lasing in cholesteric band-gap materials. In *ALCOM Symp. Chiral materials and applications*, pages 18–19, Cuyahoga Falls, 1999.

[32] A.F. Muñoz P. Palffy-Muhoray S.V. Serak B. Taheri E. Alvarez, M. He and R. Twieg. Mirrorless lasing and energy transfer in cholesteric liquid crystals doped with laser dyes. *Mol. Cryst. Liq. Cryst.*, 369, 2001.

[33] H.F. Gleeson V.A. Grozhik-J.P. Guillou S.V. Serak, E.O. Arikainen and N.A. Usova. Laser-induced concentric colour domains in a cholesteric liquid crystal mixture containing a nematic azobenzene dopant. *Liq. Cryst. Today*, 29, 2001.

[34] A. Muñoz, P. Palffy-Muhoray, and Taheri. Ultraviolet lasing in cholesteric liquid crystals. *Opt. Lett.*, 26:804–806, 2001.

[35] J. Shmidtke, W. Stille, H. Finkelmann, and S.T. Kim. Laser emission in a dye doped cholesteric polymer network. *Adv. Mater*, 14:746–749, 2002.

[36] P.V. Shibaev, K. Tang, A.Z. Genack, V. Kopp, and M.M. Green. Lasing from a stiff chain polymeric lyotropic cholesteric liquid crystal. *Macromolecules*, 35:3022–3025, 2002.

[37] S.T. Kim and H. Finkelmann. Cholesteric liquid single-crystal elastomers (lsce) obtained by the anisotropic deswelling method. *Macromol. Rapid Commun.*, 22, 2001.

[38] A. Munoz P. Palffy-Muhoray H. Finkelmann, S.T. Kim and B. Taheri. Tunable mirrorless lasing in cholesteric liquid crystalline elastomers. *Adv. Mater*, 13:1069–1072, 2001.

[39] M. Ozaki, M. Kasano, D. Ganzke, W. Haase, and K. Yoshino. Mirrorless lasing in a dye-doped ferroelectric liquid crystal. *Adv. Mater.*, 14:306–309, 2002.

[40] K. Yoshino D. Ganzke M. Kasano, M. Ozaki and W. Haase. Electrically tunable waveguide laser based on ferroelectric liquid crystals. *Appl. Phys. Lett.*, 82, 2003.

[41] T. Kitasho D. Ganzke-W. Haase M. Ozaki, M. Kasano and K. Yoshino. Electro-tunable liquid crystal laser. *Adv. Mater.*, 15, 2003.

[42] R. Caputo A. De Luca C. Versace N. Scaramuzza C. Umeton R. Bartolino G. Strangi, V. Barna and G.N. Price. Color-tunable organic microcavity laser array using distributed feedback. *Phys. Rev. Lett.*, 94(063903):1–4, 2005.

[43] A. Chanishvili, G. Chilaya, G. Petriashvili, R. Barberi, R. Bartolino, M.P. De Santo, M.A. Matranga, and F.Ciuchi. Lasing in an intermediate twisted phase between cholesteric and smectic a phase. *Appl. Phys. Lett.*, 88:101105 1–3, 2006.

[44] M. Ozaki K. Funamoto and K. Yoshino. Discontinuous shift of lasing wavelength with temperaure in cholesteric liquid crystals. *Jpn. J. Appl. Phys.*, 42(L):1523–1525, 2003.

[45] W. Cao C. Bailey B. Taheri M.F. Moreira, I.C.S. Carvalho and P. Palffy-Muhoray. Cholesteric liquid-crystal laser as an optic-fiber based temperature sensor. *Appl. Phys. Lett.*, 85, 2004.

[46] V.P. Shibaev A.Y. Bobrovsky, N.I. Boiko and J.H. Wendorff. Cholesteric mixtures with photochemically tunable, circularly polarized fluorescence. *Adv. Mater.*, 15, 2003.

[47] G. Petriashvili R. Barberi R. Bartolino G. Cipparrone A. Mazzulla A. Chanishvili, G. Chilaya and L. Oriol. Phototunable lasing in dye doped cholesteric liquid crystals. *Appl. Phys. Lett.*, 83, 2003.

[48] S.V. Gryshchenko I.P. Ilchishin, O.V. Yaroshchuk and E.A. Shaydiuk. Influence of the light-induced molecular transformations on the helix pitch and lasing spectra of cholesteric liquid crystals. In *ALCOM Symp. Chiral materials and applications*, volume Proc. SPIE-5507, pages 229–234, 2004.

[49] D. Chiappetta V. Milner A. Genack P.V. Shibaev, R.L. Sanford and A.Bobrovsky. Light controllable tuning and switching of lasing in chiral liquid crystals. *Opt. Expr.*, 13, 2005.

[50] J. Madsen P.V. Shibaev and A.Z. Genack. Lasing and narrowing of spontaneous emission from responsive cholesteric films. *Chem. Mater.*, 16, 2004.

[51] V.K.S. Hsiao A.N. Cartwright P.N. Prasad L.V. Natarajan V.P. Tondiglia R. Jakubiak R.A. Vaia G.S. He, T.-C. Lin and T.J. Bunning. Tunable two-photon pumped lasing using a holographic polymer-dispersed liquid-crystal grating as a distributed feedback element. *Appl. Phys. Lett*, 83, 2003.

[52] H.-B. Sunand S. Kawata K. Shirota. Two-photon lasing of dye doped photonic crystal lasers. *Appl. Phys. Lett.*, 84, 2004.

[53] T. Matsui M. Ozaki, R. Ozaki and K. Yoshino. Twist-defect-mode lasing in photopolimerzed cholesteric liquid crystals. *Jpn. J. Appl. Phys.*, 42, 2003.

[54] J. Schmidtke and W. Stille. Photonic defect modes in cholesteric liquid crystal films. *Phys. J. E-Soft Matter*, 12, 2003.

[55] M.H. Song. Effect of phase retardation on defect mode in polyeric cholesteric liquid crystals. *Adv. Mater*, 16, 2004.

[56] B. Taheri A. Marino W. Cao, P. Palffy-Muhoray and G. Abbate. Lasing thresholds of cholesteric liquid crystals lasers. *Mol. Cryst. Liq. Cryst.*, 429, 2005.

[57] F.P. Schafer. *Principles of Dye Laser Operation in Dye lasers*, chapter 1, pages 1–89. Springer-Verlag, Berlin Heidelberg, third enlarged and revised edition, 1990.

[58] J.E. Kim Y.C. Yang, C.S. Kee and H.Y. Park. Photonic defect modes of cholesteric liquid crystals. *Phys. Rev. E*, 60, 1999.

[59] V.I. Kopp and A.Z. Genack. Twist defect in chiral photonic structures. *Phys. Rev. Lett.*, 89(3)(033901):1–4, 2002.

[60] H.A. van Sprang. Combined tilt and thickness measurements on nematic liquid crystal samples. *Mol. Cryst. Liq. Cryst.*, 199, 1991.

[61] G. Petriashvili A. Chanishvili, G. Chilaya and P. Colligs. *Phys. Rev. E*, 71, 2005.

[62] V.A. Mallia and N. Tamaoki. *Chem. Soc. Rev.*, 33, 2004.

[63] G. Petriashvili A. Chanishvili, G. Chilaya and D.Sikharulidze. In *Abstracts of 6th European Conference on Liquid Crystals*, volume 2, page P3, Halle, Germany, 2001.

[64] G. Petriashvili R. Barberi R. Bartolino A. Chanishvili, G. Chilaya and M.P. De Santo. *Mol. Cryst. Liq. Cryst.*, 434, 2005.

[65] G. Petriashvili A. Chanishvili, G. Chilaya and D. Sikharulidze. *Mol. Cryst. Liq. Cryst.*, 409, 2004.

[66] L.N. Lisetski T.S. Piliashvili G.S. Chilaya, Z.M. Elashvili and K.D. Vinokur. *Mol. Cryst. Liq. cryst.*, 74, 1981.

[67] G Chilaya. *Revue. Phys. Appl., 16, 193.*, 16, 1981.

[68] G.S. Chilaya and L.N. Lisetski. *Sov. Phys. Usp.*, 24, 1981.

[69] G.S. Chilaya and L.N. Lisetski. *Mol. Cryst. Liq. Cryst.*, 140, 1986.

[70] G.S. Chilaya Z.M. Elashvili, T.S. Piliashvili and K.G.Z. Djaparidze. *Z. Chem*, 19, 1979.

[71] J.C. Mastrangelo S.W. Chen, H. Shi and J.J. Ou. *Prog. Polym. Sci*, 21, 1996.

[72] F. Oestreicher G. Chilaya and G. Scherowsky. *Mol. Mater.*, 9, 1998.

[73] G. Semenkova L.Kutulya, V. Vashchenko and N. Shkolnikova. *Mol. Cryst. Liq. Cryst.*, 331, 1999.

[74] A. Ferrarini G. Gottarelli G. Licini C. Rosini S. Superchi S. Pieraccini, M.I. Donnoli and G.P. Spada. *J. Org. Chem.*, 68, 2003.

[75] E. Sackman. *J. Am. Chem. Soc.*, 93, 1971.

[76] T. Nagase K. Kuruhara, T.Kanda and T. Nonaka. *Appl. Phys. Lett*, 73, 1998.

[77] H. Nakazumi T. Yamaguchi T. Inagava and M. Irie. *Chem Mater*, 12, 2000.

[78] C. Ruslim and K. Ichimura. *J. Phys. Chem. B*, 104, 2000.

[79] H. Harada O. Tsustsumi A. Kanazawa T. Shiono H.K. Lee, K. Doi and T. Ikeda. *J. Phys. Chem. B*, 104, 2000.

[80] N. Koumura B.L. Feringa, R.A. van Delden and E.M. Geertsema. *Chem. Rev.*, 100, 2000.

[81] N. Tamaoki. *Adv. Mater.*, 13, 2001.

[82] H. Matsuda M. Moriyama, S. Song and N. Tamaoki. *J. Mater. Chem.*, 11, 2001.

[83] G. Petriashvili A. Chanishvili, G. Chilaya and D. Sikharulidze.

[84] S.V. Serak N.V. Tabiryan and V.A. Grozhik. *J. Opt. Soc. Am. B*, 20, 2003.

[85] T. Ikeda. *J. Mater. Chem.*, 13, 2003.

[86] T. Sasaki S. Kurihara T. Ikeda, T. Miamito and S. Tazuke. *Mol. Cryst.*, 188, 2003.

[87] T. Ikeda and O. Tsutsumi. *Science*, 268, 1995.

[88] M.S. Soskin S.G. Odulov, Yu.A. Reznikov and A.I. Khizniak. *Sov. Phys. JEPT*, 55, 1982.

[89] M.S. Soskin S.G. Odulov, Yu.A. Reznikov and A.I. Khizniak. *Sov. Phys. JEPT*, 55, 1983.

[90] P. Chatelain M.C. R. Germain. *C.R. Acad. Sc.*, 259, 1964.

[91] G. Petriashvili R. Barberi R. Bartolino G. Cipparone A. Mazzulla R. Gimenez L. Oriol M. Pinol A. Chanishvili, G. Chilaya. Widely tunable ultraviolet-visible liquid crystal laser. *Apl. Phys. Lett.*, 86(051107):1–3, 2005.

[92] G. Petriashvili R. Barberi R. Bartolino G. Cipparone A. Mazzulla P. V. Shibaev G. Chilaya, A. Chanishvili. Reversible tuning of lasing in cholesteric liquid crystals controlled by light-emitting diodes. *Adv. Mater.*, 19, 2007.

[93] G. Petriashvili R. Barberi R. Bartolino M. P. De Santo M. A. Matranga P. Collings G. Chilaya, A. Chanishvili. Light controll of cholesteric liquid crystals using azoxy-based host materials. *Mol. Cryst. Liq. Cryst.*, 453, 2006.

[94] P. Palffy-Muhoray A. Munoz and B. Taheri. *Apl. Phys. Lett.*, 82, 2003.

[95] A. Otomo S. Furumi, S. Yokoyama and S. Mashiko. *Apl. Phys. Lett.*, 82, 2003.

[96] T. Kitasho D. Ganzke W. Haase K. Yoshino M. Ozaki, M. Kasano. *Adv. Mater.*, 15, 2003.

[97] D. Kruerke H. Sawade G. Heppke A. Jakli, L.C. Chien. Light shutters from antiferroelectric liquid crystals of bent-shaped molecules. *Liq. Cryst.*, 29, 2002.

[98] G. Petriashvili R. Barberi R. Bartolino G. Cipparrone A. Mazzulla L. Oriol A. Chanishvili, G. Chilaya. Phototunable lasing in dye-doped cholesteric liquid crystals. *Apl. Phys. Lett.*, 83, 2003.

[99] G. Petriashvili R. Barberi R. Bartolino G. Cipparrone A. Mazzulla L. Oriol A. Chanishvili, G. Chilaya. Lasing in dye-doped liquid crystals: two new strategies of tuning. *Adv. Mater*, 16, 2004.

[100] G. Chilaya. *Rev. Phys. Appl.*, 16, 1981.

[101] G.S. Chilaya and L.N. Lisetski. *Mol. Cryst. Liq. Cryst.*, 140, 1986.

[102] L.N. Lisetski T.S. Piliashvili G.S. Chilaya, Z.M. Elashvili and K.D. Vinokur. *Mol. Cryst. Liq. Cryst.*, 74, 1981.

[103] S.R. Renn and T.C. Lubensky. *Phys. Rev. A*, 38, 1988.

[104] H.-S. Kitzerow. *Chirality in Liquid Crystals*. Springer, New York, 2001.

[105] G. Petriashvili A. Chanishvili, G. Chilaya and D. Sikharulidze. *Mol. Cryst Liq. Cryst. Sci. Technol., Sect. A*, 261, 1995.

[106] G.S. Chilaya. *Crystallog. Rep.*, 45, 2000.

[107] M. Neundorf G. Pelzl A. Chanishvili, G. Chilaya and G. Petriashvili. *Cryst. Res. Technol.*, 31, 1996.

[108] Y. Bouligand. *Liquid Crystalline Order in Polymers*. Academic, New York,, 1978.

[109] K.-C. Shin T. Ohta Y. Tsunoda H. Hoshi Y. Takanishi K. Ishikawa J. Watanabe S. Nishimura T. Toyooka Z. Zhu T.M. Swager M.H. Song, B. Park and H. Takezoe. *Adv. Mater.*, 16, 2004.

[110] S. Kniesel J. Schmidtke and H. Finkelmann. Probing the photonic properties of a cholesteric elastomer under biaxial stress. *Macromolecules*, 34(4), 2005.

[111] K. Amemiya B. Park Y. Takanishi K. Ishikawa J.W. Wu S. Nishimura T. Toyooka M.H. Song, N.Y. Ha and H. Takezoe. Defect-mode lasing with lowered threshold in three-layered hetero cholesteric liquid crystal structure. *Advanced materials*, 18(2), 2006.

[112] Y. Hirota, Y.Ji, F. Serra, A.R. Tajbakhsh, and E.M. Terentjev. Effect of crosslinking on the photonic bandgap in deformable cholesteric elastomers. *Optics Express*, 16(8), 2008.

[113] S.T. Kim and H. Finkelmann. Cholesteric liquid single-crystal elastomers (lsce) obtained by the anisotropic deswelling method. *Macromol. Rapid Commun.*, 22, 2001.

[114] K. Hammerschmidt and H. Finkelmann. Stress-optical and thermomechanical measurements on liquid crystalline elastomers. *Makromol. Chem.*, 190(5), 1989.

[115] Y. Hirota. Cholesteric elastomers for a tunable laser. Mphil, University of Cambridge, 2007.

[116] B. Park S.W. Kim and Y.P. Lee. Polarized laser emission from an anistropic one dimensional photonic crystal laser. *Applied Physics letters*, 90(16), 2007.

[117] G. Chilaya, A. Chanishvili, G. Petriashvili, R. Barberi, G. Cipparrone, A. Mazzulla, M.P. De Santo, H. Sellame, and M.A. Matranga. Single mode lasing in multilayer sandwiched systems consisting of cholesteric liquid crystals and dye solution. In *Xv International Symposium on Advanced Display Technologies*, volume 6637, page 6670, 2007.

[118] A.F. Mckinley and B.L. Diffey. A reference spectrum for ultraviolet induced erythema in human skin. *CIE Journal*, 1987.

[119] G. J. Smith. 4.763.011. USA PATENT, 9 August 1988.

[120] J. H. Kinsey and R. J. Harms. 5.401.970. USA PATENT, 28 March 1995.

[121] A. F. Beaubien D. J. Beaubien. 5.331.168. USA PATENT, 19 July 1994.

[122] M. P. Wueest. 6.426.503. USA PATENT, 30 July 2002.

[123] G. Chilaya G. Petriashvili S. Tavzarashvili L. Lisetski I. Gvozdovskyy M.Aronishidze, A.Chanishvili and I. Terenetskaya. *Mol. Cryst. Liq. Cryst.*, 420:47–53, 2004.

[124] A. Chanishvili I. Terenetskaya N. Kireeva G. Chilaya, G. Petriashvili and L. Lisetski. *Mol. Cryst. Liq. Cryst.*, 433:73–85, 2005.

[125] G. Petriashvili R. Barberi R. Bartolino A. Chanishvili, G. Chilaya and M.P. De Santo. *Mol. Cryst. Liq. Cryst.*, 434:353–366, 2005.

[126] B. Lee S. Kato and C. Pac. Fluorescence behavior of cyanobiphenyl liquid crystal molecules in liquid crystal / polymer composite films. *Liquid Crystals*, 22(5):595–603, 1997.

[127] H. Levanon R. Subramanian, L.K. Patterson. Luminescence behaviour as a probe transitions and excimer formation in liquid crystals: dodecylcyanobiphenyl. *Chem. Phys. Letters*, 93(6):578–581, 1982.

[128] S. Kurihara T. Ikeda and S. Tazuke. Excimer formation kinetics in liquid-crystalline alkylcyanobiphenyls. *J. Phys.Chem.*, 94:6550–6555, 1990.

[129] S. Kurihara T. Ikeda and S. Tazuke. Persistence of ordering in 4-n-pentyl-4'-cyanobiphenyl above the nematicisotropic phase transition as detected by picosecond time-resolved fluorescence spectroscopy. *Liquid crystals*, 7(5):749–752, 1990.

[130] V.K. Doglanov and B.M. Bolotin. *Mol. Cryst. Liq. Cryst.*, 47:179–184, 1978.

List of publications

Novel UV sensor based on a liquid crystalline mixture containing a photoluminescent dye. G. Petriashvili, A. Chanishvili, G. Chilaya, M.A. Matranga, M.P. De Santo, R. Barberi. 8th national meeting of the italian liquid crystals society (SICL) *mol.cryst.liq.cryst.* (submitted)

Lasing in three layered system consisting of cholesteric liquid crystal and dye solution. G. Chilaya, A. Chanishvili, G. Petriashvili, R. Barberi, G. Cipparrone, A. Mazzulla, M. P. De Santo, H. Sellame, M. A. Matranga. *Molecular Crystals and Liquid Crystals* (submitted)

Lasing tunability and quality factor enhancement in dye doped chiral liquid crystals. G. Cipparrone, A. De Luca, M.P. De Santo, M. A. Matranga, A. Mazzulla, G. Strangi and R. Bartolino. *Journal of optoelectronics and advanced materials* (submitted).

Lasing stability enhancement in dye doped cholesteric liquid crystal. M.P. De Santo, M.A. Matranga, G. Petriashvili, G. Chilaya, and R. Barberi. *Proceedings of Japanese-Italian liquid crystal workshop 2008, to be published in Molecular Crystal and Liquid Crystal* (submitted)

Wide band gap materials as a new tuning strategy for dye doped cholesteric liquid crystals laser. G.Petriashvili, G. Chilaya, M.A. Matranga, M.P. De Santo, R.Barberi. *Optics express*(submitted)

Chiral luminescent compounds as a perspective for cholesteric liquid crystal lasers. G. Petriashvili, G. Chilaya, M.A. Matranga, M.P. De Santo, G. Cozza, R. Barberi, J. del Barrio, L.S. Chinelatto jr, L. Oriol and M. Piñol. (in preparation)

Patent: "Laser senza specchi accordabile a tre strati" G. Petriashvili, R. Barberi, M.P. De Santo, M.A. Matranga, G. Desiderio, S. Abate. (in preparation).

Lasing in Three Layer Systems Consisting of Cholesteric Liquid Crystals and Dye SolutionG. Chilaya, A. Chanishvili, G. Petriashvili, R. Barberi, G. Cipparrone, A. Mazzulla, M. P. De Santo, H. Sellame, M. A. Matranga. *mol. cryst. liq. cryst., 495,97* (2008).

Single mode lasing in multilayer sandwiched systems consisting of cholesteric liquid crystals and dye solution. G. Chilaya, A. Chanishvili, G. Petriashvili, R. Barberi, G. Cipparrone, A. Mazzulla, M. P. De Santo, H. Sellame, M. A. Matranga. *XV International Symposium on Advanced Display Technologies. SPIE Proceeding Book 6637* (2007).

Enhancing cholesteric liquid crystal laser stability by cell rotation. Guram Chilaya, Andro Chanishvili, Gia Petriashvili, Riccardo Barberi, Maria P. De Santo, Mario A. Matranga, *Optic Express,Vol. 14, No. 21* (2006).

UV sensors based on liquid crystal mixtures. A. Chanishvili, G. Chilaya, G. Petriashvili, R. Barberi, M. P. De Santo, M. A. Matranga, F. Ciuchi, *SPIE Photonic Europe Proceeding Book 6192-103* (2006).

Ligth Control of cholesteric liquid crystals using azoxy-based host materials. G.Chilaya, A.Chianishvili, G.Petriashvili, R.Barberi, R.Bartolino, M.P.De Santo, M.A. Matranga, P.Collings, *Molecular Crystals and Liquid Crystals. vol. 453* (2006).

Lasing in an intermediate phase between cholesteric and smectic A. A.Chianishvili, G.Petriashvili, G.Chilaya, R.Barberi, M.P.De Santo, M.A. Matranga, F.Ciuchi. *Applied Physics Letters. 88, 101105* (2006).

Pretransitional chiral LC phase: optical characteristics and lasing. A. Chanishvili, D. Chilaia,G. Chilaya, G Petriashvili, R. Barberi, R. Bartolino, M.P. De Santo, M.A. Matranga, F. Ciuchi. *Proceedings of the XIV-th international symposium "Advanced display technologies" Alushta, Crimea, Ukraine October 10-14*, 2005.